



The effect of activity
on the fundamental properties of
low-mass stars

Juan Carlos Morales Peralta

Barcelona, maig de 2010

UNIVERSITAT DE BARCELONA
DEPARTAMENT D'ASTRONOMIA I METEOROLOGIA
PROGRAMA DE DOCTORAT D'ASTRONOMIA I METEOROLOGIA
BIENNI 2005-2007

Memòria presentada per **Juan Carlos Morales Peralta** per
optar al grau de Doctor en Ciències Físiques

DIRECTORS:
Ignasi Ribas Canudas
Carme Jordi Nebot

TUTORA:
Carme Jordi Nebot

A la meva gent

To my family

Contents

Agraïments	iii
Acknowledgements	v
Resum	vii
Overview	1
1 Introduction	3
1.1 Eclipsing binary systems	3
1.2 Fundamental properties from DDLEBs	5
1.2.1 Mass and radius	6
1.2.2 Temperature, metallicity and age	12
1.3 Stellar models	15
1.4 Aims of this work	19
2 Absolute properties of CM Draconis and IM Virginis	25
2.1 Analysis of light and radial velocity curves	26
2.2 CM Draconis	27
2.2.1 Observations	28
2.2.2 Pre-analysis of light and radial velocity data	30
2.2.3 Analysis of light and radial velocity curves	32
2.2.4 Analysis of eclipse timings	36
2.2.5 Absolute properties	39
2.3 IM Virginis	42
2.3.1 Observations	43
2.3.2 Analysis of light and radial velocity curves	44
2.3.3 Absolute properties	49
3 The effect of activity on stars	57
3.1 Comparison between models and observations	58
3.2 The case of CM Dra	60

3.2.1	Fundamental properties	60
3.2.2	Apsidal motion	63
3.3	The case of IM Vir	65
3.4	Activity on single stars	70
3.4.1	Selection of the sample of late-K and M stars	72
3.4.2	Differences between active and inactive stars	75
3.5	Activity hypothesis	80
4	Stellar models of active stars	85
4.1	Activity parameters on the Lyon stellar models	85
4.2	Sample of low-mass DDLEBs	87
4.3	Effect of spots on DDLEB analysis	90
4.3.1	Modulation on light curves	92
4.3.2	Systematics on light curves due to spots	96
4.4	Modelling active stars	101
5	Conclusions	107
5.1	Summary and results	107
5.2	Future prospects	111
	Bibliography	113
A	CM Draconis data	123
A.1	Light curves	123
A.2	Radial velocity curves	127
A.3	Minima timings	128
B	IM Virginis data	135
B.1	Light curves	135
B.2	Radial velocity curves	139
C	Searching for low-mass eclipsing binaries	141
C.1	The ROTES project	141
C.2	Eclipsing binaries from <i>COROT</i>	145

Agraïments

Abans de començar a descriure el treball realitzat en aquests anys de tesi, vull expressar el meu més sincer agraïment a tota la gent que ha contribuït d'alguna manera o altra a la consecució d'aquest treball. Per començar, cal destacar els meus directors de tesi, l'Ignasi Ribas i la Carme Jordi. Tots dos m'han transmès els seus coneixements i la seva experiència en el camp de l'astronomia i, en particular, de les estrelles de baixa massa i dels sistemes binaris. Sense els seus consells i les seves idees aquest treball no hauria estat mai possible.

També vull agrair l'hospitalitat mostrada pels membres del grup de models estel·lars del *Centre de Recherche Astrophysique de Lyon* (França), Isabelle Baraffe, Gilles Chabrier i José Gallardo. Les diverses visites a Lyon m'han permès aprofundir els coneixements en els models d'estructura estel·lar i col·laborar activament amb ells per obtenir un dels resultats més importants d'aquest treball. Cal mencionar especialment a José Gallardo, que sempre ha atès les meves peticions per provar diferents combinacions de paràmetres als models estel·lars.

La meva estada al *Harvard Smithsonian Center for Astrophysics* a Cambridge (Massachusetts, USA) va significar també un pas important en l'elaboració d'aquesta tesi i en l'aprofundiment en les tècniques d'anàlisi de dades de sistemes binaris eclipsants. Per aquest motiu estic molt agraït a en Guillermo Torres, que em va acceptar com a estudiant seu per tres mesos i de qui he après molts dels secrets d'aquestes tècniques. També agraeixo l'atenció prestada per Dave Latham en la meva incorporació temporal al seu institut, i la dels diversos companys que em van acollir gratament al seu despatx.

No vull oblidar-me tampoc dels meus companys de l'Institut d'Estudis Espacials de Catalunya ni del Departament d'Astronomia i Meteorologia de la Universitat de Barcelona. Són innumbrables les vegades que els he consultat dubtes que m'han resolt sense cap mena de problema. Clarament, part d'aquest treball també es deu a tots ells. Però per dir algú, faré menció especial al Francesc Vilardell que m'ha ajudat a entendre el secrets del codi Wilson-Devinney.

Finalment, he de mencionar a la gent de casa. He de destacar els meus pares que sempre m'han donat suport en les diferents decisions que he prè i els meus germans que sempre han estat presents en el moment en què els he necessitat. Ja per acabar, no em puc oblidar tampoc de la Rebecca, que ha mostrat una paciència inacabable durant l'escriptura d'aquesta memòria i amb qui he trobat l'equilibri necessari entre feina i oci que, sense cap mena de dubte, ha dut aquesta tesi a bon port.

Aquest treball ha comptat amb el suport econòmic d'una beca del programa de *Colaboración con departamentos* i una beca del programa de *Formación de Profesorado Universitario* (AP2005-5310) del *Ministerio de Educación y Ciencia*. També ha estat parcialment finançada a través del *Plan Nacional de Astronomía y Astrofísica* (AYA2006-15623-C02-01/02) i del pla d'*Acciones Integradas* (HF2005-0249) ambdós del ministeri esmentat anteriorment, i del *Plan Nacional de Astronomía y Astrofísica* (AYA2009-06934) del *Ministerio de Ciencia e Innovación*.

Acknowledgements

Before embarking on the description of the work done in these years of PhD Thesis, I would like to express my sincere gratitude to all the people that have contributed somehow to achieve the results of this work. To begin, I have to remark the task of my advisors, Ignasi Ribas and Carme Jordi. Both of them have transmitted to me their knowledge and experience in Astronomy, especially in the fields of low-mass stars and eclipsing binaries. Without their advice and ideas, this work would have never been possible.

Also, I have to acknowledge the hospitality of the members of the stellar modeling group of the *Centre de Recherche Astrophysique de Lyon* (France), Isabelle Baraffe, Gilles Chabrier and José Gallardo. Several visits to Lyon allowed me to go into the stellar models in depth and participate actively with them to achieve one of the more important results of this Thesis. José Gallardo must be particularly acknowledged for his constant attention to my requests to compute stellar models with different sets of parameters.

My research stay at the Harvard-Smithsonian Center for Astrophysics in Cambridge (Massachusetts, USA) represented an important part of the development of this Thesis and a deeper insight into the analysis techniques of eclipsing binary data. For this reason, I am very grateful to Guillermo Torres for accepting me as a student for three months and for revealing to me many of the secrets of these analysis techniques. Dave Latham is also acknowledged for his attention during my stay there, and also the colleagues that pleasantly took me in their office.

I cannot forget my colleagues at the *Institut d'Estudis Espacials de Catalunya* and at the *Departament d'Astronomia i Meteorologia* of the University of Barcelona. Although the number of times I have asked them for doubts is countless, they have always helped me. Clearly, part of this work is also theirs. I would like to mention Francesc Vilardell, who has helped me to understand the secrets of the Wilson-Devinney code.

Finally, I have to mention my family. The role of my parents in this work is

crucial. They have always supported me on the different decisions I have taken in my career. I am also grateful to my siblings who have been waiting whenever I need them. To finish, I can not forget Rebecca, who has been very patient during the writing of this report. With her I have also found the perfect balance between work and leisure time that, undoubtedly, has led this Thesis to a successful ending.

This thesis has been funded by a grant of the program *Colaboración con departamentos* and a grant of the PhD training program *Formación de Profesorado Universitario* (AP2005-5310) of the *Ministerio de Educación y Ciencia*. It has also been partially supported through the *Plan Nacional de Astronomía y Astrofísica* (AYA2006-15623-C02-01/02) and through the *Acciones Integradas* (HF2005-0249) of the *Ministerio de Educación y Ciencia*, and through the *Plan Nacional de Astronomía y Astrofísica* (AYA2009-06934) of the *Ministerio de Ciencia e Innovación*.

Resum

Malgrat que les estrelles de baixa massa, estrelles de tipus K tardà i de tipus M, són el component majoritari de la Galàxia, la seva estructura no es coneix encara completament. Això és en part per la dificultat d'obtenir les propietats fonamentals d'aquestes estrelles de manera precisa i acurada per tal de poder validar les prediccions dels models teòrics d'estructura i evolució estel·lar. Aquesta dificultat es va aconseguir superar mitjançant els sistemes binaris eclipsants i espectroscòpics amb línies dobles separades als espectres. Aquests sistemes estan compostos per dues estrelles que orbiten una entorn de l'altra amb la inclinació adequada per tal d'observar des de la Terra com es van eclipsant simultàniament. L'anàlisi simultània de les variacions de lluminositat del sistema durant els eclipsis (corbes de llum) i de les variacions de velocitat radial (corbes de velocitat radial) obtingudes a través de les observacions espectroscòpiques, pot proporcionar les masses i radis dels components d'un sistema binari de manera fonamental amb precisions millors que el 2%. A més, també proporciona la relació de temperatures efectives entre les estrelles del sistema, a partir de la qual es poden estimar les temperatures individuals. Aquestes propietats estel·lars fonamentals obtingudes amb tanta precisió, permeten testejar d'una manera molt acurada els models teòrics d'estructura estel·lar per validar les seves prediccions o posar de manifest les seves deficiències.

Les comparacions entre les observacions d'estrelles de baixa massa en sistemes binaris eclipsants i els models d'estructura estel·lar dutes a terme fins ara, indiquen que els models prediuen estrelles amb radis un 10% més petits i temperatures efectives un 5% més grans que les observacions (vegeu Ribas 2006a, com a referència). En canvi, les lluminositats són correctes. Els efectes de la metal·licitat o les opacitats utilitzades als models s'han considerat com possibles causes d'aquestes diferències entre les observacions i els models, tot i així, l'activitat magnètica present en aquest tipus d'estrelles ha esdevingut una les hipòtesis més acceptades (Torres & Ribas 2002; Ribas 2006b; Torres et al. 2006; López-Morales 2007).

El principal objectiu d'aquest treball, doncs, ha estat caracteritzar les estrelles de baixa massa per tal d'explicar l'origen d'aquestes discrepàncies entre els models i les observacions i testejar els efectes de l'activitat magnètica tant sobre els models com

sobre les observacions dels sistemes binaris. Un dels problemes d'aquests sistemes binaris és que la mostra de sistemes coneguts és petita, només 6 contenen almenys una estrella amb una massa inferior a $0,8 M_{\odot}$ i tenen determinacions de masses i radis amb precisions millors que el 3%. Per tant, part de l'esforç d'aquest treball també s'ha centrat en determinar les propietats fonamentals de dos sistemes binaris, CM Draconis (CM Dra) i IM Virginis (IM Vir).

CM Dra és un sistema binari format per dues estrelles de tipus espectral M4,5 que va ser analitzat prèviament per Lacy (1977). Aquest sistema és especialment interessant perquè les masses dels components es situen per sota del límit d'estrelles totalment convectives ($M < 0,35 M_{\odot}$), un rang de masses en el qual no hi ha sistemes estudiats acuradament. A més, la seva òrbita lleugerament excèntrica el converteix en un bon candidat per determinar propietats de la seva estructura interna a partir la detecció del moviment de precessió de la seva òrbita. La gran quantitat de corbes de llum disponibles pel sistema i les corbes de velocitat radial publicades a Metcalfe et al. (1996), juntament amb les millores en els programes d'anàlisi han permès determinar les masses i radis dels components d'aquest sistema amb precisions de l'ordre del 0.5%: $M_1 = 0,2310 \pm 0,0009 M_{\odot}$, $M_2 = 0,2141 \pm 0,0010 M_{\odot}$, $R_1 = 0,2534 \pm 0,0019 R_{\odot}$ i $R_2 = 0,2396 \pm 0,0015 R_{\odot}$. En aquesta anàlisi, s'ha fet un esforç especial per tal d'eliminar l'efecte de les taques superficials que mostren les estrelles del sistema i per tal de testejar les possibles sistemàtiques en els valors de les propietats fonamentals obtingudes.

A més per a aquest sistema també s'ha obtingut una estimació de l'edat a partir de l'anàlisi de la nana blanca de moviment propi comú a CM Dra. Respecte la metal·licitat, existeixen mesures dutes a terme per Viti et al. (1997, 2002) però els seus resultats no són del tot concloents. Per tant, aquesta quantitat no està ben determinada. Aquests dos paràmetres són importants en la comparació amb els models, ja que si es coneixen es fixen tots els paràmetres lliures dels models. En cas contrari, es poden arribar a estimar a partir dels models si s'assumeix que tots dos components es van formar a la vegada i a partir del mateix material. En aquest cas els models haurien de ser capaços de reproduir simultàniament les propietats fonamentals dels dos components del sistema binari amb una única edat i metal·licitat.

Finalment, per acabar l'anàlisi de les observacions d'aquest sistema binari, s'han estudiat un total de 200 temps de mínim (101 eclipsis primaris i 99 secundaris). Aquests temps de mínim mostren la presència significativa d'un moviment de precessió. No obstant, el valor d'aquest moviment apsidal, $\dot{\omega} = (2,3 \pm 1,4) \times 10^{-4} \text{ }^{\circ} \text{ cicle}^{-1}$, no té encara la precisió adequada per poder afegir-ho en la comparació amb els models. A més, el seu valor està en clar desacord amb el valor teòric que es prediu. Això pot estar indicant l'existència d'algun altre efecte sobre aquest moviment de precessió, com per exemple un tercer cos al sistema tot i que la seva existència no es

pot encara confirmar.

En el cas de IM Vir, hem disposat de corbes de llum i de velocitat radial que estaven encara pendents d'analitzar. Les masses i radis s'han pogut determinar amb una precisió per sota del 2%: $M_1 = 0,981 \pm 0,012 M_\odot$, $M_2 = 0,6644 \pm 0,0048 M_\odot$, $R_1 = 1,061 \pm 0,0016 R_\odot$ i $R_2 = 0,681 \pm 0,013 R_\odot$. L'interès especial d'aquest sistema rau en el fet que els seus components són de masses molt diferents, per tant, permeten testejar millor els models que han d'ajustar simultàniament dues estrelles significativament diferents. Desafortunadament, però, per aquest sistema no s'ha obtingut cap estimació de l'edat o la metal·licitat a part de la indicació d'una metal·licitat lleugerament subsolar obtinguda a partir de l'anàlisi de les observacions espectroscòpiques de les quals s'han extret les corbes de velocitat radial.

Anàlisis preliminars de CM Dra es van presentar a Morales et al. (2007a,b). Els resultats dels estudis complets de CM Dra i IM Vir han estat publicats a Morales et al. (2009a) i Morales et al. (2009b), respectivament. El segon d'aquests treballs es va dur a terme durant una estada al *Harvard-Smithsonian Center for Astrophysics* (Massachusetts, USA).

En comparar aquests dos sistemes binaris amb els models d'estructura estel·lar de Baraffe et al. (1998), desenvolupats per reproduir les estrelles de baixa massa, les discrepàncies en els radis i les temperatures efectives són similars a les que s'havien observat per altres sistemes binaris de baixa massa (Ribas 2006a). En el cas de CM Dra, els radis del component primari i secundari són un 5,0% i un 5,2%, respectivament, més grans que les prediccions teòriques, mentre que les temperatures són un 6,4% i un 5,9% més fredes. Les diferències són encara més grans si es considera una metal·licitat subsolar tal com proposa Viti et al. (1997, 2002). Per tant, les discrepàncies entre models i observacions també s'observen en el rang de les estrelles totalment convectives. Per altra banda, les lluminositats estan relativament ben determinades. En el cas de IM Vir, s'ha comprovat que cap model, independentment de la metal·licitat o l'edat, és capaç de reproduir a la vegada les masses i els radis dels dos components del sistema. Suposant que la lluminositat està ben determinada pels models, com semblen indicar els resultats per altres sistemes binaris, es pot ajustar un model amb una edat de $2,4 \pm 0,5$ Gyr i una metal·licitat de $-0,28 \pm 0,10$ dex, però llavors els radis que prediuen els models són un 3,7% i un 7,5% més petits pels components primari i secundari del sistema, respectivament, i les temperatures efectives un 2% i un 3,5% més altes, en consonància amb els resultats d'altres observacions.

La presència de taques a les fotosferes dels components d'aquests dos sistemes binaris, observades com una modulació de la magnitud a les corbes de llum, i la detecció de fulguracions i emissió saturada en raigs X revelen que aquest dos siste-

mes presenten una elevada activitat magnètica. Això és una característica comuna amb altres sistemes binaris, en els quals les elevades velocitats de rotació dels seus components (degudes a la sincronització entre el moviment orbital i el de rotació) en presència de camps magnètics provoquen una elevada activitat. A més, en aquest treball també s'ha trobat que la comparació entre estrelles actives i inactives isolades de la mateixa lluminositat (i, per tant, massa) mostren diferències similars de temperatura efectiva i radi (Morales et al. 2008a,b), corroborant així la hipòtesi que l'activitat magnètica és la responsable de les discrepàncies entre els models i les observacions.

En col·laboració amb el grup de models d'evolució estel·lar del *Centre de Recherche Astrophysique de Lyon* (Isabelle Baraffe, Gilles Chabrier i José Gallardo), s'ha estudiat quin és l'efecte de la introducció de l'activitat magnètica als models i com es comparen aquest models amb les observacions. Aquest grup, mostra que la rotació i l'activitat magnètica es poden introduir als models reduint l'eficiència del transport convectiu de l'energia o suposant l'aparició de taques a la superfície de les estrelles (Chabrier et al. 2007). El primer cas es modelitza reduint el paràmetre α de longitud de barreja al model de la convecció i es pot veure que el seu efecte és molt petit per estrelles totalment convectives. El segon cas es modelitza introduint un paràmetre β que mesura la fracció de superfície de l'estrella coberta per taques purament fosques. Aquestes taques bloquegen part del flux d'energia que surt cap a l'exterior i l'estrella compensa aquesta reducció amb un augment del radi per tal de mantenir el flux.

Aquests models s'han comparat amb una mostra dels sistemes binaris amb les propietats fonamentals millor determinades (Morales et al. 2010). Les estrelles totalment convectives de CM Dra s'han fet servir per separar els efectes de α i β i s'ha avaluat també l'efecte de les cobertures de taques que es deriven dels models sobre les corbes de llum. Les conclusions principals són que cap efecte per si sol pot explicar les diferències de radi entre el 5% i el 10% entre els models i les observacions. Cal tenir en compte tres factors principals:

- La presència de taques polars poden causar una sistemàtica d'aproximadament un 3% en la determinació dels radis estel·lars a partir de les corbes de llum de binàries eclipsants.
- En introduir aquestes taques polars als models, una cobertura corresponent a $\beta \sim 0.17$ explicaria aproximadament un 2% de la sistemàtica en radi.
- En les estrelles amb més elevada rotació i, per tant, camps magnètics més potents, a més caldria una disminució de l'eficiència de la convecció (reduint α), que explicaria fins a un 4% de la diferència restant.

Aquest escenari també explicaria les diferències en les temperatures efectives i està en acord amb les modulacions observades a les corbes de llum. A més la cobertura

de taques que es prediu amb els models, un 35% de la superfície (assumint $\beta \sim 0.17$ i un contrast de temperatura entre les taques i la fotosfera de 0,85) és compatible amb els resultats obtinguts amb imatges Doppler d'estrelles actives.

Aquests resultats es basen per una banda en assumir que les taques en les estrelles estudiades apareixen preferentment als pols, i per l'altra, que totes elles presenten aproximadament la mateixa cobertura de taques. La primera hipòtesi està en consonància amb les imatges Doppler obtingudes per algunes estrelles amb rotacions elevades (vegeu Strassmeier 2009, com a referència), mentre que la segona es pot constatar pel fet que totes aquestes estrelles, presenten nivells saturats d'activitat tal com mostra l'emissió en raigs X.

Resumint breument, els resultats d'aquest treball conclouen que l'activitat magnètica és un paràmetre rellevant a tenir en compte en l'estudi de les estrelles de baixa massa, ja que altera significativament la seva estructura estel·lar, ja sigui a través del transport convectiu de l'energia, a través de l'aparició de taques a la superfície estel·lar o d'ambdós efectes a la vegada. L'obtenció de les propietats fonamentals d'estrelles de baixa massa en nous sistemes binaris, i en particular sistemes amb períodes llargs que continguin estrelles inactives, proporcionarien la confirmació final dels resultats d'aquest treball.

Overview

Although low-mass stars, those with masses lower than the mass of the Sun, comprise about 75% of the stars in the Galaxy, their structure and evolution are not yet fully understood. This is, in part, because of their intrinsic faintness that made very difficult their observation until large telescopes became available. Besides, the accurate and reliable determination of the fundamental properties of stars, such as masses and radii, is still a difficult task. The masses are usually computed from luminosity calibrations, and the radius are commonly dependent on the distance to the system or on temperature and luminosity calibrations, but the accuracies reached with these methods are not sufficient to constrain the parameters involved in the models. Knowing precisely the structure and evolution of low-mass stars is especially interesting since other objects such as brown-dwarfs or gaseous planets share common characteristics. Nowadays, with the increasing interest in exoplanets, it is also remarkable that the calculation of the masses and the sizes of exoplanets around M-type stars and their habitability are dependent on the precise knowledge of the host stars.

The difficulty in measuring the fundamental properties of these stars was overcome with the discovery of detached double-lined eclipsing binaries (DDLEBs) with low-mass components. As for more massive systems, these binary systems provide the masses and radii of their components through the analysis of the light variations caused by mutual eclipses and of their radial velocity variations. The accuracies reached on these fundamental properties are of sufficiently high accuracy to carry out stringent tests of stellar evolutionary models. Several such analyses in the past 15 years have unveiled that stellar structure models predict smaller radii and higher effective temperatures for main-sequence stars with masses below that of the Sun. However, the luminosities are well reproduced by models, thus indicating that the discrepancies in the radius and the effective temperature are in the right proportion to preserve the luminosity.

The main disadvantage of low-mass DDLEBs is their scarcity due to the low probability to be observed as eclipsing and their intrinsic faintness, which reduce the number of eclipsing binaries with high-quality observations to a few nearby systems.

Thus, increasing the sample of known systems with accurate masses and radii is very valuable in order to draw firm conclusions about the discrepancy with stellar models. With the recent development of precise spectroscopic techniques and deep photometric surveys to detect extrasolar planets, such as *COROT* or *Kepler*, this handicap is expected to be overcome.

The main goal of this work is to understand the reasons of the discrepancy found between models and observations in order to get accurate descriptions of low-mass stars. Two interesting eclipsing binary systems, CM Draconis and IM Virginis have been also analyzed, obtaining their masses and radii with uncertainties below the 1% and 2% level, respectively, thus increasing the number of well-known low-mass stars. The components of these systems and the most accurate low-mass main-sequence components from eclipsing binaries were subsequently used to test the predictions of stellar evolutionary models.

Tests of stellar models using a sample of DDLEBs with accurate properties (including CM Draconis and IM Virginis) confirmed that the radii and the effective temperatures of low-mass stars are not correctly predicted by theoretical models. Several possibilities have been considered to explain the differences between models and observations, but activity has been shown to be a reasonable explanation in the context of DDLEBs. Constraints on model parameters suggested to explain the activity effects have been also explored here.

This report is structured in two main parts, the first focused on the observational point of view and the second on the theoretical models. In Chapter 1, the introduction to the analysis of eclipsing binaries and their comparison with models is presented. Chapter 2 is devoted to the analysis of one of the systems with lowest mass stellar components known to date, CM Draconis, and also to the case of IM Virginis, a system with a small mass ratio, favorable to test the stellar models. Chapter 3 describes the comparison of both of these systems with the stellar models and also with other accurate low-mass eclipsing binaries with properties fundamentally determined. This comparison and differences observed between single main-sequence active and inactive stars lead to the hypothesis that magnetic activity plays an important role on these stars. This hypothesis is tested on stellar evolutionary models to reconcile their predictions with the observations in Chapter 4. Finally, Chapter 5 summarizes the conclusions and the future work. Appendixes show the complete data sets of CM Draconis and IM Virginis and also the activities carried out to increase the number of DDLEB systems through a photometric follow-up survey of open clusters and through the selection of DDLEB candidates from *COROT* data. Both works being still in progress.

Chapter 1

Introduction

Stellar population analyses indicate that the vast majority of stars in the Galaxy are less massive than the Sun. However, due to their intrinsic faintness, their fundamental properties have not been as accurately determined as in the case of massive stars until recently. During past years, the study of low-mass stars in Astrophysics has experienced an important progress due to the improvement of photometric and spectroscopic techniques that has made their precise observation easier. Stellar structure and evolution models of late-type stars have also been developed. Detached double-lined eclipsing binaries (hereafter DDLEBs) were found to be the best way to check the results of theoretical models, because fundamental properties of their components can be determined with very high accuracy (1-2%). Comparison of the observed properties of low-mass stars derived from these DDLEBs with the stellar models have unveiled that there is a significant discrepancy between the radii and the effective temperatures observed for low-mass stars and those predicted by models, while luminosities are well described (see, e.g., Ribas 2006a, and references therein).

This chapter is a brief introduction to low-mass star research. The general case of DDLEBs and the analysis techniques to obtain the fundamental properties of their components with an unprecedented accuracy are described. Next, a comparison of the observed properties of low-mass stars with models is presented. This leads to the main aim of this Thesis, which is, in short, to understand the disagreements between the stellar models and the observations.

1.1 Eclipsing binary systems

According to the Vogt-Russell theorem (e.g., Carroll & Ostlie 1996), mass and initial chemical composition are the fundamental properties that determine the evolution of an isolated star. Given their values, stellar structure and evolution models com-

pute the internal structure of a star as a function of time and predict observable quantities such as radius, effective temperatures and luminosities by solving the hydrostatic equilibrium, energy production and transport equations. These predictions need to be compared with the properties observed on stars in order to validate the models. Therefore, stars with known mass, radius, effective temperature, chemical composition and age are extremely valuable for this purpose. However, these fundamental properties are not easily measurable independently of any kind of calibration for single stars. For instance, masses are usually computed as a function of the spectral type and luminosity class, which on their own, depend on color calibrations or spectral indices. In the case of the radius of stars, this can be estimated from the relation between the effective temperature and the total luminosity (computed from an apparent magnitude and a bolometric correction) or from direct interferometric measurements, but then the distance to the star needs to be accurately known.

Research in this field revealed that DDLEBs are the best objects to derive fundamental properties of stars. The analysis of photometric and spectroscopic observations of these systems provide the masses and radii of the components of the system with accuracies down to the 2% level, even for low-mass stars. This exquisite accuracy makes possible a thorough test of the stellar models and their key ingredients such as the equation of state, the convection theory or the opacities (Andersen 1991; Torres et al. 2010).

DDLEBs are composed of two stars in a close orbit but detached enough to have evolved almost as single stars, unlike the case of semi-detached or contact binaries, where mutual interactions are significant. “Double-lined” means that the spectral lines of both components can be observed, therefore the projection of the orbital velocity of each star on the direction of observation (called radial velocity) is measurable by means of the Doppler effect on the spectra. From these curves, the mass ratio and a lower limit of the semi-major axis of the orbit can be determined. Their eclipsing nature enables us to derive the relative radius of each component and the orbital inclination through the light variations during the mutual eclipses. Thus, it is when combining the analyses of radial velocity curves and light curves, that both the masses and the radii of each component of the system can be measured almost independently of any model or calibration.

The main drawback of these systems is their scarcity. In order to derive accurate stellar radii, the binaries must experience eclipses. Therefore the binary orbit needs to be observed almost edge-on, i.e., the inclination of the orbital momentum vector with respect to the line of sight has to be approximately 90° . For a binary system composed of two stars with radii R_1 and R_2 orbiting each other with a circular orbit with semimajor axis a , the minimum inclination (i_{lim}) to be observable as eclipsing

is given by:

$$\cos i_{\text{lim}} = \frac{R_1 + R_2}{a} = r_1 + r_2 \quad (1.1)$$

where r_1 and r_2 are redefinitions of the radius being scaled to the semi-major axis. Assuming that the orbit orientations of binaries are randomly distributed, the probability of a system to be eclipsing is equal to the cosine of this limit angle. Thus close pairs are expected to have higher chances of being observed as eclipsing binaries since the probability scales with the inverse of the semi-major axis, i.e., with $P^{-2/3}$ and $(M_1 + M_2)^{-1/3}$. As a reference, a binary system composed of two stars orbiting each other with a period of 1 day would be eclipsing in $\sim 38\%$ of the cases if stars are like the Sun, but only in $\sim 8\%$ if their orbital period is about 10 days. The situation is even worse if we consider a system with $0.5 M_{\odot}$ stars, for which these probabilities decrease to $\sim 24\%$ and $\sim 5\%$, respectively.

This low-probability of binary systems to be observable as eclipsing binaries explains why known DDLEBs are usually short period systems. A consequence of this selection bias is that the stars in these short period systems are expected to rotate in synchrony with the orbital motion (Mazeh 2008). This causes them to be fast rotators that in the presence of magnetic fields, trigger high levels of magnetic activity. This activity is often observed as variability in the light curves due to photospheric spots and flares, and these have to be taken into account in the analysis to derive fundamental properties. In very close binary systems, tidal effects between component could also be important and cause deformations of the stellar surface. However, the deviations from a perfect sphere are expected to be small for detached systems.

The scarcity of known systems has led to several photometric surveys designed to discover new binary systems spanning a wide range of orbital periods and masses. Surveys focused on open clusters (Hebb et al. 2004; Ribas et al. 2006, 2007; Shaw & López-Morales 2007) are valuable because the age and metallicity of the binary system components can be estimated from the cluster membership. The recent increase of deep photometric surveys and space missions, such as *COROT* and *Kepler* devoted to the detection of transiting extrasolar planets, are expected to observe also a wealth of eclipsing binary systems from which will be possible to determine accurate properties of low-mass stars.

1.2 Fundamental properties from DDLEBs

Photometric and spectroscopic time-series of DDLEBs provide different information about the orbital and physical parameters of the system. From light curves, the radius relative to the semimajor axis of each component, the inclination of the system

and the temperature ratio of the stars are determined. On the other hand, radial velocity curve results provide the projected semimajor axis and the mass ratio. Thus, the inclination is needed to derive the absolute value of the semimajor axis, which in turn provides the absolute masses and radii of the components from the results of radial velocity curves and light curves, respectively. In more general cases of eccentric orbits, both types of data provide information about the eccentricity and the initial argument of the periastron, and even about the rate of apsidal motion, if present.

Additionally, in order to better constrain the stellar structure models, the effective temperature of each component and the chemical composition and age of the system should be known. The ratio of effective temperatures of the components can be accurately determined from the light curves, but some additional constraint is needed to convert this ratio into absolute values. No further information can be retrieved from light and radial velocity curves, and one needs to use other approaches to derive the rest of the properties of the stars.

1.2.1 Mass and radius

The spectral lines of both the primary and the secondary components are observable in a spectrum of a DDLEB. These spectral lines are Doppler shifted due to the orbital motion of the stars. When the lines of the primary are blue-shifted, those of the secondary are red-shifted and vice versa. Using cross-correlation codes, such as TODCOR (Zucker & Mazeh 1994), the spectra of both components can be disentangled and their respective radial velocities (the projection of the velocity on the line of sight) determined as a function of time, or orbital phase if the period is known. Uncertainties of a few km s^{-1} can be typically reached with this method for DDLEBs.

Information about the semimajor axis and the masses of the binary components can be obtained from these radial velocities. The radial velocity of each component as a function of time is given by:

$$v_{r,j} = \gamma + K_j [\cos(\theta + \omega) + e \cos(\omega)], \quad (1.2)$$

where $v_{r,j}$ is the radial velocity of component j (1 for the primary, 2 for the secondary), γ is the systemic velocity of the center of mass of the system, K_j is the velocity semi-amplitude of component j , e and ω are the eccentricity and the longitude of the periastron, respectively, and θ is the true anomaly, that contains the dependence on time. The semi-amplitude K_j , depends on the semimajor axis of the orbit of each star a_j as:

$$K_j = \frac{2\pi a_j \sin i}{P\sqrt{1 - e^2}}, \quad (1.3)$$

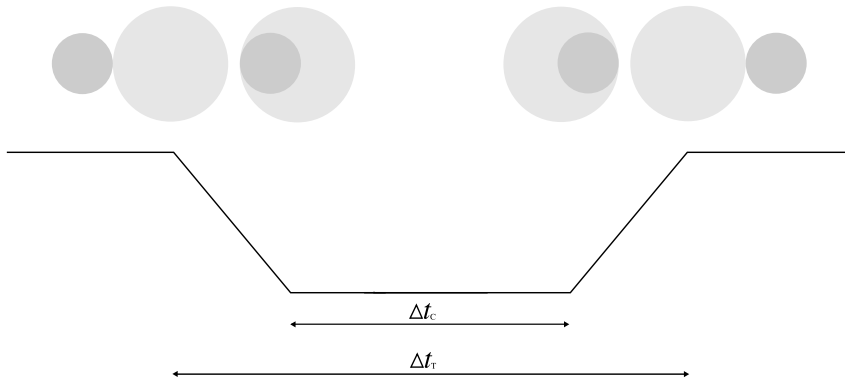


Figure 1.1: Diagram of a central eclipse in a binary system. Circles indicate the configuration of the stars in first, second, third and fourth contact from left to right, respectively.

where i is the inclination of the orbital plane with respect to the line of sight and P is the orbital period. Then, the amplitude of the radial velocity curve is a direct measurement of $a_j \sin i$, and, since the period can be determined by periodicity analysis of the curves, $M_j \sin^3 i$ can be also computed, providing a lower limit to the masses of the binary components. The mass ratio ($q = \frac{M_2}{M_1}$) can also be recovered, but not the individual masses due to the indetermination of the inclination.

On the other hand, photometric time-series of DDLEBs show the light variations of the system due to the mutual eclipses between the components. The shape and duration of the eclipses depend mostly on the sizes of the binary components relative to their separation. Figure 1.1 displays the case of a central primary eclipse, when the star with the lower surface brightness crosses in front of the brighter in a perfectly edge-on orbit ($i = 90^\circ$). If we assume a circular orbit with relative semimajor axis a , the total duration of the transit (from first to fourth contact) is given by:

$$\Delta t_T = \frac{P}{\pi} \arcsin \left(\frac{R_1 + R_2}{a} \right), \quad (1.4)$$

where P is the orbital period and R_1 and R_2 are the radius of the primary¹ and the secondary components respectively. The time from second to third contact, when secondary star is completely inside the disk of the primary is given by:

$$\Delta t_C = \frac{P}{\pi} \arcsin \left(\frac{R_1 - R_2}{a} \right). \quad (1.5)$$

¹The primary is usually considered to be the star occulted during the deepest eclipse. It usually coincides with the hotter and larger star but it depends on the properties of the system.

From these two equations, the radii relative to the semimajor axis $r_1 = \frac{R_1}{a}$ and $r_2 = \frac{R_2}{a}$ can be computed. Besides, the depth of the eclipses depends on the ratio of radii $k = \frac{R_2}{R_1}$ and effective temperatures $\frac{T_{\text{eff}2}}{T_{\text{eff}1}}$. This adds constraints on the radius of the components. Light curves are thus only sensitive to the relative scale of the system, so in order to determine the absolute radii, the semimajor axis must be obtained from radial velocity curves.

These results are only valid when the inclination is assumed to be very close to 90° and in the case of circular orbits. If this is not the situation, the eclipses are not central any more and can even be only partial, in which event Δt_C cannot be determined. In this case, the shape, the duration, the depth and the separation of the eclipses are dependent on the inclination, the eccentricity and the argument of the periastron, so their values can be determined from fits to light curves, closing the loop to obtain the absolute masses and radii of the binary components. Light curves provide the relative sizes and the inclination, and radial velocity curves yield the size and mass scale of the system, along with other orbital properties.

$$\begin{array}{l}
 \text{Light curves} \\
 \text{Radial velocities}
 \end{array}
 \left\{ \begin{array}{l}
 \text{Period, } P \\
 \text{Relative radii, } \frac{R_j}{a} \\
 \text{Inclination, } i \\
 \text{Temperature ratio, } \frac{T_{\text{eff}2}}{T_{\text{eff}1}} \\
 \text{Eccentricity and periastron, } e \text{ and } \omega \\
 \\
 \text{Period, } P \\
 \text{Minimum semimajor axis, } a \sin i \\
 \text{Minimum masses, } M_j \sin^3 i \\
 \text{Eccentricity and periastron, } e \text{ and } \omega
 \end{array} \right\}
 \begin{array}{l}
 \\
 \\
 \\
 \\
 \\
 \\
 \\
 \\
 \text{Masses, } M_1 \text{ and } M_2 \\
 \text{Radii, } R_1 \text{ and } R_2
 \end{array}$$

Inverting the radial velocity curves of a DDLEB is a straightforward problem of fitting an analytical function to a set of data. But on the other hand, fitting the light curves is much more complex and numerical computation must be used, especially in the case of eccentric orbits or when second order contributions such as the effect of limb darkening or reflections between the components need to be taken into account.

There are several codes in the literature to invert both radial velocity and light curves, but one of the more sophisticated physically-sound and widely-used code is the Wilson-Devinney (hereafter WD; Wilson & Devinney 1971; Wilson 1979). This code fits the observations by computing differential corrections of the relevant parameters of the system starting from initial guessed values. It has evolved since its first creation in 1971 in order to account for several second order effects such as reflections between stars, limb darkening, gravity darkening, deformations due to tidal forces or the presence of spots on the stellar surface. One of its advantages is that

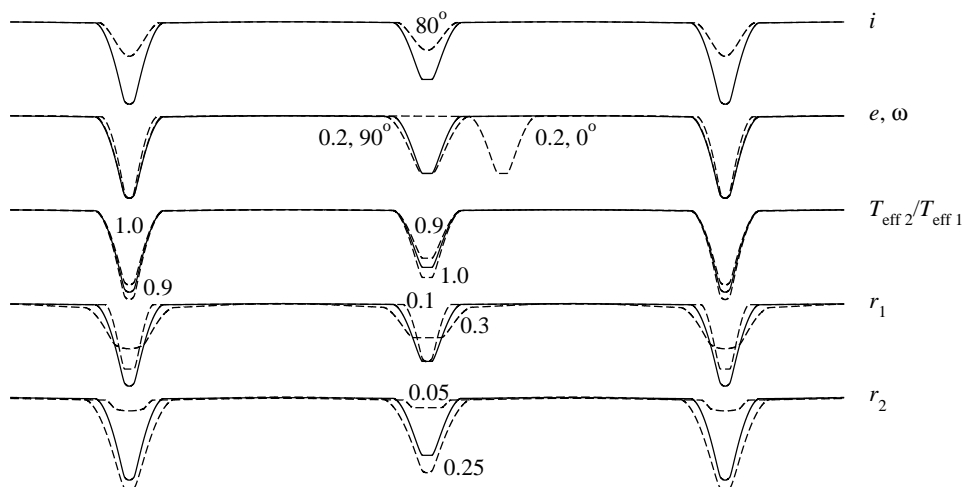


Figure 1.2: Effect of different orbital and physical parameters of a DDLEB on the light curve. Solid lines correspond to the following elements: $i = 90^\circ$, $e = 0$ and $\omega = 90^\circ$, $\frac{T_{\text{eff}2}}{T_{\text{eff}1}} = 0.95$, $r_1 = 0.2$, $r_2 = 0.15$ and linear limb darkening coefficients fixed to 0.5 for both components. Dashed lines correspond to the light curves with the parameters changed as labeled. The vertical and horizontal axes on this plot are decreasing magnitudes and orbital phase (or time), respectively, in arbitrary units.

several radial velocity and light curves in different spectral bands can be analyzed simultaneously in order to derive consistent orbital and physical parameters. Intensive use of this code has been done throughout this work, so we proceed with a brief description of its implementation to model light and radial velocity curves.

Light curve analysis

In the general case of an eccentric binary orbit, the main orbital and physical parameters that can be adjusted with the WD code are the period (P), the zero point of ephemeris (T_0), the inclination of the orbit (i), its eccentricity (e) and argument of the periastron (ω), the effective temperature ratio ($\frac{T_{\text{eff}2}}{T_{\text{eff}1}}$), the bandpass luminosity ratio ($(L_2/L_1)_\lambda$) and the surface pseudo-potentials (Ω_1 and Ω_2). WD code makes use of the Roche model (Kopal 1978) to compute the surfaces of stars, so surface pseudo-potentials Ω_j are used instead of the radii relative to the semimajor axis (r_j). The effects of some of these parameters on the light curves are displayed in Figure 1.2.

There are other parameters that have influence on the light curves. For instance, this is the case of the limb darkening coefficients that take into account the brightness distribution on the disks of the stars. For each component, the WD code permits a

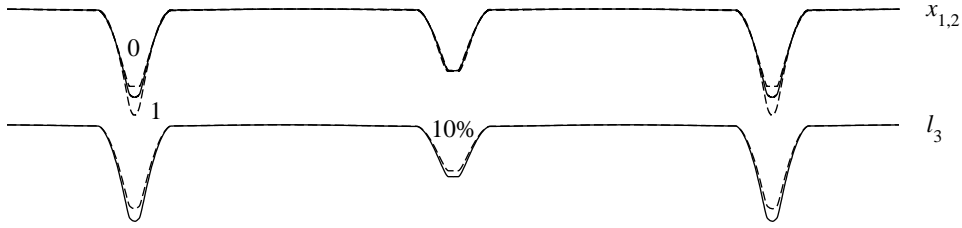


Figure 1.3: Effect of the linear limb darkening coefficient ($x_{1,2}$) and the third light (ℓ_3) on light curves. Solid lines correspond to $x_1 = x_2 = 0.5$ and $\ell_3 = 0\%$. Dashed lines correspond to the light curves with the parameters changed as labeled.

fit of the coefficient x of a linear limb darkening law given by:

$$\frac{I}{I_0} = 1 - x(1 - \mu) \quad (1.6)$$

where μ is the cosine of the incidence angle, I is the intensity of the star at this angle and I_0 is the intensity of the star at the center of the disk. Figure 1.3 shows the effect of different x coefficients on the light curves. This effect is coupled with the ratio of radii, especially when eclipses are only partial. So the value of x is difficult to determine from light curves and strongly depends on the ratio of radii. Thus, limb darkening coefficients values are often taken from theoretical tables (Claret 2000a) computed from atmosphere models, in which case, WD permits the use of much more realistic limb darkening laws such as logarithmic or square-root, with two coefficients x (linear) and y (non-linear). These coefficients depend on the temperature, surface gravity and chemical composition of the stars and also on the bandpass of the light curve. This dependency is used to break the correlation of the limb darkening coefficients with other parameters by analyzing precise light curves in different bands simultaneously. However, some independent constraint, such the luminosity ratio derived from spectral analysis, is desirable to assure that solutions are physically consistent.

Figure 1.3 also shows the effect of third light (ℓ_3) on the light curves. This parameter takes into account the possible light contamination of a background or foreground source. Its main effect is a decrease of the depth of the eclipses and its value, reported as a fraction of the total light at a quadrature phase, can be fitted using the WD code.

Proximity effects can also be taken into account with the WD code. Their influence is much smaller for well-detached systems but for high-accuracy parameters such effects need to be taken into account. These are the reflectivity of the stars, modeled with an albedo parameter for each component (A_j), and tidal deformations.

Under the presence of tides between the components, they lose the spherical symmetry and become Roche equipotential surfaces. In first approximation, in this case, gravity darkening ($g_{1,2}$) and the fractional ratio between rotation of each star and the orbital period (F_j) should also be considered when fitting the light curves. In the case of low-mass stars in short period binaries, as those analyzed in this work, gravity darkening coefficients are usually taken from theoretical tables (Claret 2000b) and synchronization (or pseudo-synchronization with the orbital velocity at periastron) is usually assumed given their short periods.

Finally, the WD code also permits fitting of the effect of spots on the stellar surface. This is important in our case since low-mass DDLEBs are usually short-period binaries that show high levels of magnetic activity. The presence of spots is observable on light curves as modulations in the out-of-eclipse phases. The WD code models spots with four parameters for every spot: two for the position, co-latitude (θ) and longitude (ϕ), and the others for the spot size (r_s measured as the subtended angle from the center of the star) and effective temperature ratio ($\frac{T_{\text{eff},s}}{T_{\text{eff}}}$). Their effect on the light curves is displayed in Figure 1.4. Different spots on both components of a binary system can be fitted, although parameters such as co-latitude, temperature ratio and size can be strongly correlated.

Radial velocity curve analysis

In the general case of eccentric orbits, the parameters that can be fitted to the radial velocity curves are the period (P), the zero point of ephemeris (T_0), the eccentricity (e), the argument of the periastron (ω), the systemic radial velocity of the binary system (γ) and the velocity semi-amplitude of both components of the system (K_1 and K_2), although the WD code uses the semimajor axis (a) and the mass ratio (q) of the system instead of the velocity semi-amplitudes. This is for simplicity when simultaneous analyses of radial velocities and light curves are performed. Figure 1.5 shows the effect of some of these parameters on the curves.

Other secondary effects on the radial velocity curves are also implemented in the code. This is the case of irradiation, which influences the conditions under which the spectral lines are formed, and the Rossiter-McLaughlin effect, that takes into account the different regions occulted during the eclipses for the integration of the spectral lines. As Figure 1.6 shows, this effect could be important during the eclipse phases.

Finally, photospheric spots also distort the shape of the spectral lines and their effect on radial velocity curves is observable as an additional modulation. Although the amplitude of this modulation is typically below the noise of the radial velocity

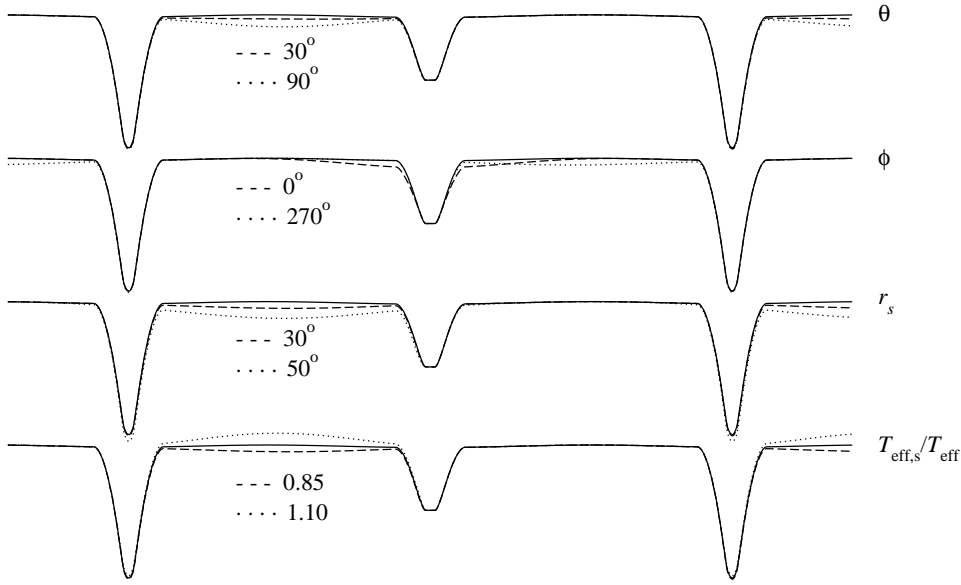


Figure 1.4: Effect of a surface spot on the secondary component of a DDLEB on the light curve. Solid lines correspond to the light curve of the system without the spot while dashed and dotted lines, to the effect of the spot. The spot parameters are $\theta = 45^\circ$, $\phi = 90^\circ$, $r_s = 30^\circ$ and $\frac{T_{\text{eff},s}}{T_{\text{eff}}} = 0.85$ except otherwise indicated.

curves of binaries, it is important to check its effect on the fits in order to provide reliable uncertainties of the semi-major axis and the mass ratio, from which absolute masses and radii are directly determined.

1.2.2 Temperature, metallicity and age

Light curves are sensitive to the ratio of the effective temperatures of the components, but not to their absolute values. Usually the effective temperature of the primary is assumed either from spectral analysis or spectral type estimations. Once the light curves are fitted, and light and radii ratios of the components are estimated, individual temperatures can be refined by different methods.

One possibility is to derive the absolute bolometric luminosity of the system from an apparent magnitude and, then, the individual luminosities and temperatures can be determined using the radii and the luminosity ratios. The distance to the system and a bolometric correction either from theoretical models (Bessell et al. 1998) or empirical calibrations (Flower 1996) are needed to compute the luminosity from the apparent magnitude. The more accurate these two properties are, the better

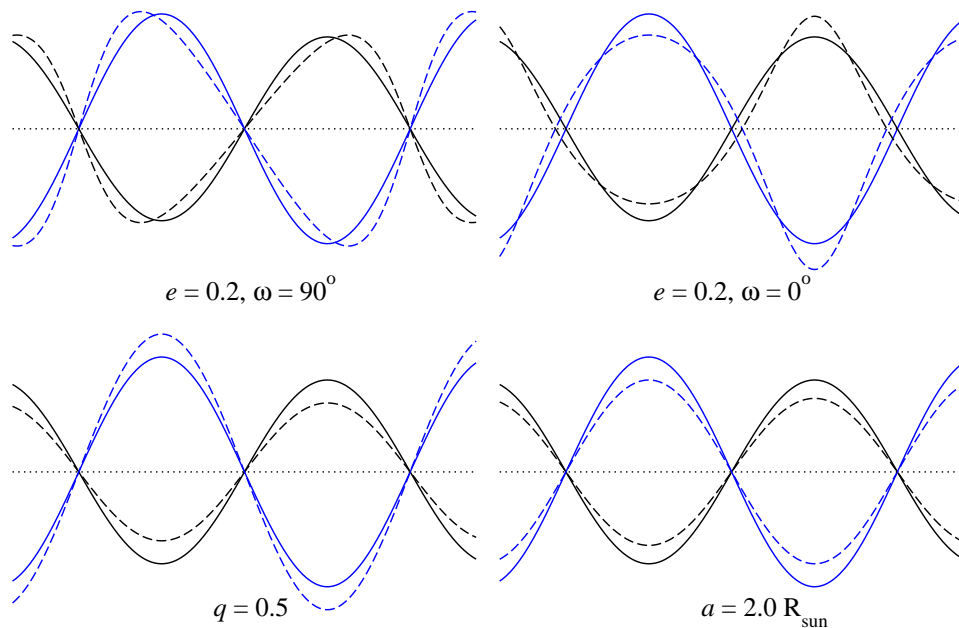


Figure 1.5: Influence of the DDLEB parameters on the radial velocity curves. Radial velocities of both stars are plotted as black and blue lines for the primary and secondary components, respectively. The solid lines correspond to: $q = 0.8$, $a = 2.5 R_{\odot}$ (with $i = 90^{\circ}$), $e = 0$ and $\omega = 90^{\circ}$. Dashed lines correspond to the changes on the different parameters as labeled. The dotted line marks the level of the systemic radial velocity. The vertical and horizontal axes on these plots are velocities and orbital phase (or time), respectively, in arbitrary units.

the temperature determination, so trigonometric parallaxes and IR magnitudes, for which bolometric corrections are less dependent on temperatures and chemical composition, are preferred.

On the other hand, if the distance is not known, color-temperature calibrations can provide individual temperatures. In this case, the absolute luminosity can be computed, and hence, the distance to the binary system is estimated when compared with the apparent magnitude. Many calibrations of this type can be found in the literature (see Ramírez & Meléndez 2005; Masana et al. 2006; Casagrande et al. 2006, 2008; González Hernández & Bonifacio 2009, as some examples). Comparison of the temperatures derived from different calibrations provides an estimation of their uncertainties.

The age and surface metallicity are more difficult to determine for M-stars. In the case of metallicity, it can be determined from analysis of high resolution spec-

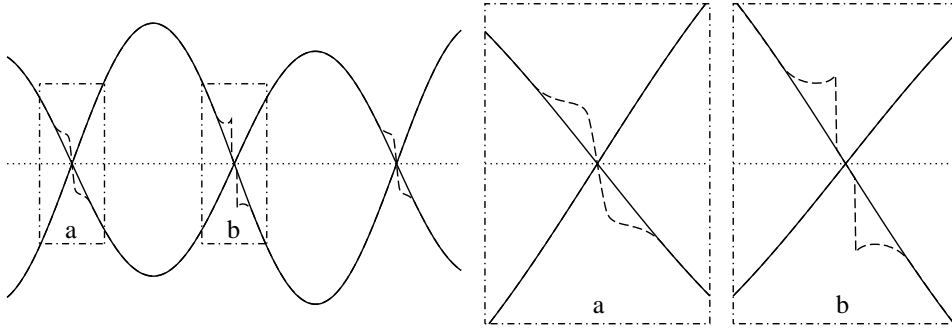


Figure 1.6: Influence of the proximity effects on the DDLEB radial velocity curves. Solid and dashed lines correspond to radial velocities without and with proximity effects considered, respectively. Right panels show an enlargement of the affected orbital phases as shown.

tra. This can be in principle done while cross-correlating the spectra of DDLEBs to derive the radial velocities if theoretical atmosphere models are used as templates. However, theoretical models still have some shortcomings in fitting the spectra of M-stars and they can only provide rough estimates of the metallicity. Color calibrations with metallicities could also be used to derive estimates of the chemical composition. Colors in the Strömgren bands are known to correlate well with metallicity (Holmberg et al. 2007). For cool stars, Bonfils et al. (2005) also found a calibration of metallicity with the $V - K$ color and K magnitude although Johnson & Apps (2009) noticed that this calibration is too low by ~ 0.3 dex for late type stars with subsolar compositions. So, the uncertainties on the chemical composition derived from this kind of calibrations are rather large.

The determination of the age is much more complicated. The only way to obtain the age of the system is through its membership to an open cluster, a kinematic group or a multiple system. In this case, if a common origin in time is assumed for the ensemble, both the age and the metallicity of the binary system are similar to those of the cluster or moving group, although their determination is model dependent.

For DDLEBs composed of two components with significantly different masses, stellar models should fit the mass-radius and the mass-effective temperature relationships of both components with the same isochrone. This can be used also to estimate the metallicity and age of the system although this can be, in general, less accurate than cluster ages and metallicities.

1.3 Stellar models

The interior structure of a star depends on its initial mass, its initial chemical composition and its age. Given these quantities, stellar structure and evolution models solve the hydrodynamic equations of a sphere of gas in order to derive all the other observable quantities and the interior profiles. Some approximations are generally assumed to simplify the problem. First, it is considered that during most of the time, the evolution of a star is much slower than its typical hydrodynamic timescale, thus stellar models assume quasistatic equilibrium and solve the structure equations in subsequently small time steps. Besides, in most cases, spherical symmetry is also assumed, and rotation and magnetic field effects are disregarded. Then, the problem is reduced to the determination of the radial dependence of the pressure, the interior mass, the interior luminosity and the temperature, through the resolution of the hydrostatic equilibrium, mass conservation, energy conservation and energy transport equations. Detailed description of these equations and the stellar modelling techniques are available on reference literature (see Kippenhahn & Weigert 1990, as an example).

A few more ingredients are still needed in order to solve the equations. On the one hand, relations between the independent variables, the production of energy and the photon-matter interactions are necessary. These are the equations of state and describe the pressure, the nuclear reaction rates, and the opacity as a function of the density, the temperature and the chemical composition. On the other hand, the description of the transport of energy in the stellar interior is also mandatory. Radiative and convective transport are the most efficient ways to transport energy in the stars, and dominate in different regions of the star depending on the temperature profiles and opacities. In the case of low-mass stars, during the main sequence, they are generally formed by a convective envelope and a radiative core that shrinks with decreasing mass, until the stars become fully convective. Convective transport is not yet fully understood and the phenomenologic Mixing Length Theory is used. It assumes that the energy is transported by bubbles of hot material that rise up adiabatically until they dissipate in the surrounding material. The path of these bubbles is known as the mixing length, l_{mix} , and is scaled to the pressure scale height H_{P} as:

$$l_{\text{mix}} = \alpha H_{\text{P}} \quad (1.7)$$

where α is used as a free parameter of the models and it is calibrated to fit the properties of the Sun.

Several stellar evolutionary models have been published by a number of research groups. Their models mainly differ on the equations of state and the boundary conditions set to solve the structure differential equations. Few of them reach the

low-mass domain, some examples being the models from the groups of Lyon (Baraffe et al. 1998, for masses between $1.4 M_{\odot}$ and the hydrogen burning limit), Grenoble (Siess et al. 2000, for masses between $7 M_{\odot}$ and $0.1 M_{\odot}$) and Padova (Girardi et al. 2000, for masses between $7 M_{\odot}$ and $0.15 M_{\odot}$). In this work, extensive use of the models of the Lyon group has been done since they were developed for the particular case of low-mass stars. The main differences with other models are the use of an equation of state developed for the degenerate conditions in low-mass stars (Saumon & Chabrier 1991, 1992), and the boundary conditions used. The Baraffe et al. (1998) models, instead of using a grey approximation, which is not adequate for low-mass stars, smoothly connect the *NextGen* atmosphere models (Allard & Hauschildt 1995; Allard et al. 1997) to the interior profiles. A comprehensive description of the models can be found in Chabrier & Baraffe (1997), Baraffe et al. (1997, 1998), and references therein.

Stellar models from the Lyon group are publicly available for different masses, chemical compositions and mixing length parameters α (Baraffe et al. 1997, 1998). This α parameter is calibrated to ~ 1.9 for the solar model, however the authors argue that $\alpha \sim 1.0$ is preferred for low-mass stars, although its effect is almost inconsequential for masses below $\sim 0.6 M_{\odot}$. Figures 1.7 and 1.8 compare the theoretical $M - R$, $M - T_{\text{eff}}$ and $M - \log L$ relationships for a 1 Gyr solar metallicity model with $\alpha = 1$ and empirical stellar values derived from observations. The sample of observations is listed in Table 1.1 (including the results obtained for CM Dra and IM Vir in this work). Results of DDLEB observations as well as from single-lined eclipsing binaries, stars with radius measured interferometrically and M-stars in post-common envelope binaries are plotted, although in these latter cases, masses and radii are not as fundamentally determined as for DDLEBs. In the case of post-common envelope components, besides, the systems may not be reliable representations of single stars due to the interactions suffered during the common envelope phase.

A significant departure of DDLEB observations from model predictions is evident in the $M - R$ and $M - T_{\text{eff}}$ plots. Stars with radius measured interferometrically do not clearly show this trend, but their uncertainties and scatter are very large to draw firm conclusions. For the case of DDLEBs, theoretical models predict smaller radius and larger effective temperatures for low-mass stars below $0.8 M_{\odot}$ while luminosities are in good agreement, thus deviations in radii and effective temperatures are in the correct sense to reproduce the correct luminosities. Roughly, observed radii are $\sim 12\%$ larger and effective temperatures are $\sim 4\%$ cooler than model predictions. There is also a clear difference between stars below and above $\sim 0.35 M_{\odot}$. On the lower mass domain, radii are better reproduced by models and less scattered while on the upper-end, both the difference with models and the scatter are larger. This behavior was already reported by Ribas (2006a) and may be consistent with the mass boundary between fully convective stars ($M \lesssim 0.35 M_{\odot}$) and partially

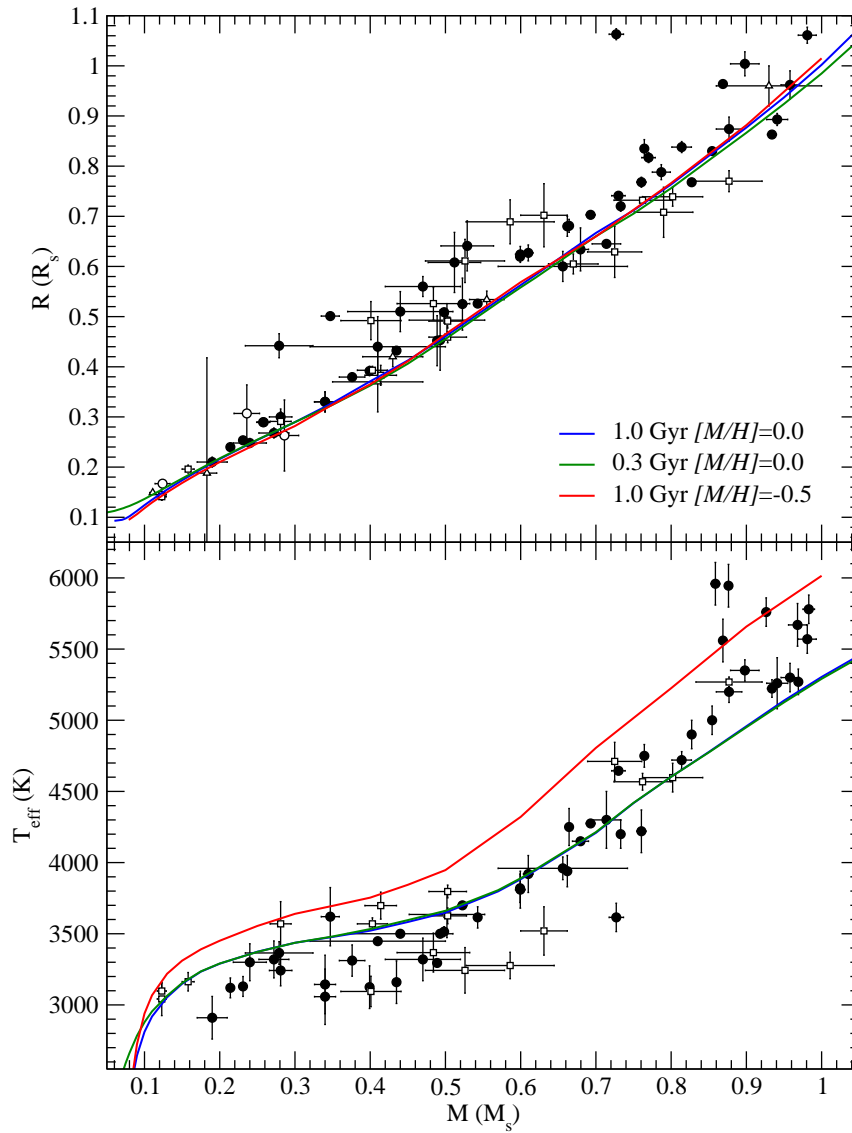


Figure 1.7: $M - R$ and $M - T_{\text{eff}}$ relationships observed for low-mass stars. Observations from DDLEBs (solid circles), single-lined eclipsing binaries (open circles), stars with interferometric measurement of radius (squares) and M-stars in post-common envelope binaries (triangles) are compared with isochrones from Baraffe et al. (1998) with different ages and metallicities as labeled. Error bars are plotted when available.

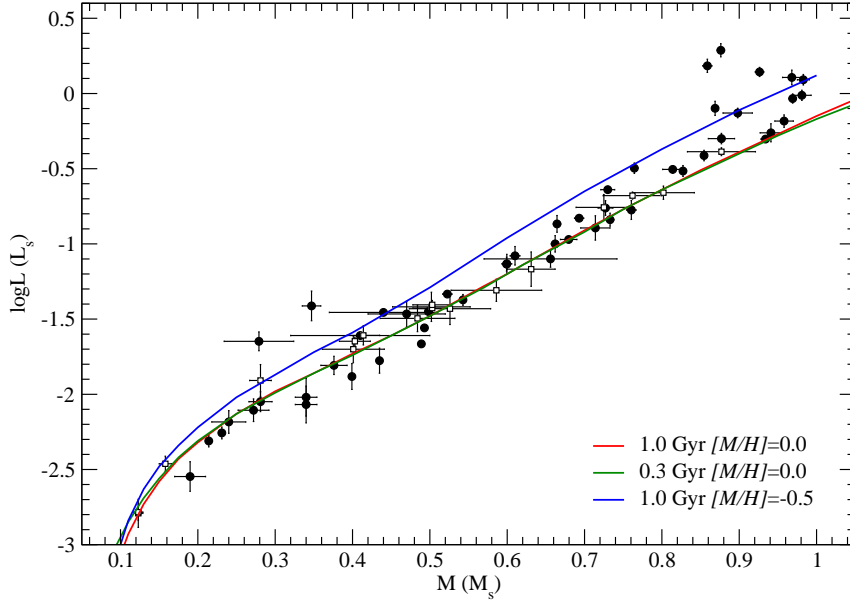


Figure 1.8: $M - L$ relationship observed for low-mass stars. Same legend as in Figure 1.7.

radiative stars. For the more massive stars (above $0.8 M_{\odot}$), radius and temperature evolution may be in part responsible for the large scatter and the differences with models.

These results may indicate that some ingredient is still missing in the stellar structure models to reproduce these stars and several hypotheses have been proposed. Metallicity or missing opacities were proposed to explain the discrepancies between models and observations (Berger et al. 2006; Casagrande et al. 2008), although, this should affect also single stars, which are known to be well described by stellar models (Demory et al. 2009). Magnetic activity was also proposed as a plausible cause of these differences (Torres & Ribas 2002; Ribas 2006b; López-Morales 2007) since most of the known DDLEBs have magnetically active components.

Critical comparisons of stellar structure models with the sample of stars with most accurate stellar properties would shed more light on this problem. DDLEB components with accurate fundamental properties and with different masses and orbital properties would also be very useful to test the correlations between these parameters and the discrepancies with models.

1.4 Aims of this work

The aim of this work is to understand the differences found between stellar model predictions and observations of low-mass stars. In order to do this, the stellar structure models are compared with fundamental properties of stars in eclipsing binaries. As mentioned in the previous sections, these systems provide masses and radii of stars with the best accuracies reached up to now, thus providing stringent constraints on model ingredients. However, only few DDLEBs with accurate fundamental properties are yet known. An important part of this work has been also devoted to increase the sample of such systems.

Therefore, the work is structured in different main topics:

1. The first is devoted to the analysis of two interesting low-mass eclipsing binaries. One is CM Draconis, a system composed of two stars with masses below the fully convective boundary, providing the first measures with masses and radii accurate to the 1% level at this mass range. This system forms a proper motion group with a white dwarf from which an indication of the age can be obtained, thus minimizing the number of free parameters for the comparison with models. The other system is IM Virginis, that is composed of two stars with a mass ratio of ~ 0.7 . This mass leverage permits a critical comparison with models since any isochrone must fit both components, thus reducing also the number of free parameters. The description of the analysis of these two systems is described in Chapter 2.
2. The second topic is centered on the understanding of the reported differences between models and observations of low-mass stars. Different causes for this discrepancy have been proposed but the critical comparison with models of the cases of CM Draconis, IM Virginis as well as other DDLEB systems leads us to propose that magnetic activity is the most plausible explanation. To support this hypothesis, the physical properties of isolated active stars was investigated (Morales et al. 2008a). This part corresponds to Chapter 3.
3. Finally, the activity hypothesis was tested on the stellar models in collaboration with the Lyon stellar modeling group given their prescriptions Chabrier et al. (2007), revealing the crucial model parameters that need to be modified to reproduce the observations. The main result of this work is achieved in Chapter 4, where a scenario to explain the differences consistent both with stellar models and with the observations of eclipsing binaries is proposed.

Further work is in progress to increase the sample of stars with accurate fundamental properties, in order to test the validity of this scenario using the data from

photometric surveys and from *COROT*. A short description of this ongoing work is given in Appendix C.

Table 1.1: Low-mass stars with masses below $1 M_{\odot}$ with reported radii and effective temperatures.

Name	P (days)	M (M_{\odot})	R R_{\odot}	T_{eff} (K)	Ref.
Double-lined eclipsing binaries					
FL Lyr B	2.18	0.958±0.012	0.962±0.028	5300±100	Torres et al. (2010)
ZZ Uma B	2.30	0.9691±0.0048	1.1562±0.0096	5270±90	Torres et al. (2010)
V658 Lyr B	14.47	0.8273±0.0042	0.7679±0.0064	4900±100	Torres et al. (2010)
V818 Tau B	5.61	0.7605±0.0062	0.768±0.010	4220±150	Torres & Ribas (2002)
V636 Cen B	4.28	0.8545±0.0030	0.8300±0.0043	5000±100	Torres et al. (2010)
CV Boo B	0.85	0.968±0.012	1.174±0.023	5670±150	Torres et al. (2010)
V1174 Ori B	2.63	0.7271±0.0096	1.063±0.011	3615±100	Torres et al. (2010)
UV Psc A	0.86	0.9829±0.0077	1.110±0.023	5780±100	Torres et al. (2010)
UV Psc B	0.86	0.7644±0.0045	0.835±0.018	4750±80	
IM Vir A	1.31	0.981±0.012	1.061±0.016	5570±100	Morales et al. (2009b)
IM Vir B	1.31	0.6644±0.0048	0.681±0.013	4250±130	
CG Cyg A	0.63	0.941±0.014	0.893±0.012	5260±180	Torres et al. (2010)
CG Cyg B	0.63	0.814±0.013	0.838±0.011	4720±60	
RW Lac A	10.37	0.9263±0.0057	1.1864±0.0038	5760±100	Torres et al. (2010)
RW Lac B	10.37	0.8688±0.0040	0.9638±0.0040	5560±150	
HS Aur A	9.82	0.898±0.019	1.004±0.024	5350±75	Torres et al. (2010)
HS Aur B	9.82	0.877±0.017	0.874±0.024	5200±75	
47 Tuc V69 A	29.55	0.8762±0.0048	1.3148±0.0051	5945±150	Thompson et al. (2010)
47 Tuc V69 B	29.55	0.8588±0.0060	1.1616±0.0062	5959±150	
2MASS J05162881+2607387 A	2.59	0.787±0.012	0.788±0.015	–	Bayless & Orosz (2006)
2MASS J05162881+2607387 B	2.59	0.770±0.009	0.817±0.010	–	
NGC2204 S892 A	0.45	0.733±0.005	0.72±0.01	4200±100	Rozyczka et al. (2009)
NGC2204 S892 B	0.45	0.662±0.005	0.68±0.02	3940±110	
RXJ0239.1-1028 A	2.07	0.730±0.009	0.741±0.004	4645±20	López-Morales & Shaw (2007)
RXJ0239.1-1028 B	2.07	0.693±0.006	0.703±0.002	4275±15	
NSVS 06507557 A	0.52	0.656±0.086	0.600±0.030	3960±80	Çakırılı & İhanoglu (2010)
NSVS 06507557 B	0.52	0.279±0.045	0.442±0.024	3365±80	
NSVS 02502726 A	0.56	0.714±0.019	0.645±0.006	4300±200	Çakırılı et al. (2009)
NSVS 02502726 B	0.56	0.347±0.012	0.501±0.005	3620±205	
T-Lyr1-17236 A	8.43	0.6795±0.0107	0.634±0.043	4150	Devor et al. (2008)
T-Lyr1-17236 B	8.43	0.5226±0.0061	0.525±0.052	3700	
GU Boo A	0.49	0.6101±0.0064	0.627±0.016	3920±130	Torres et al. (2010)
GU Boo B	0.49	0.5995±0.0064	0.624±0.016	3810±130	
YY Gem AB	0.81	0.5992±0.0047	0.6194±0.0057	3820±100	Torres et al. (2010)
NSVS01031772 A	0.37	0.5428±0.0027	0.5260±0.0028	3615±75	López-Morales et al. (2006)
NSVS01031772 B	0.37	0.4982±0.0025	0.5088±0.0030	3515±35	

Table 1.1: Continued.

Name	P (days)	M (M_{\odot})	R R_{\odot}	T_{eff} (K)	Ref.
UNSW-TR-2 A	2.12	0.529 ± 0.035	0.64 ± 0.05	–	Young et al. (2006)
UNSW-TR-2 B	2.12	0.512 ± 0.035	0.61 ± 0.06	–	
TPES-Her0-07621 A	1.12	0.493 ± 0.003	0.453 ± 0.060	3500	Creavey et al. (2005)
TPES-Her0-07621 B	1.12	0.489 ± 0.003	0.452 ± 0.050	3295	
2MASS J04463285+1901432 A	0.62	0.47 ± 0.05	0.56 ± 0.02	3320 ± 150	Hebb et al. (2006)
2MASS J04463285+1901432 B	0.62	0.19 ± 0.02	0.21 ± 0.01	2910 ± 150	
BW3 V38 A	0.20	0.44 ± 0.07	0.51 ± 0.04	3500	Maceroni & Montalbán (2004)
BW3 V38 B	0.20	0.41 ± 0.09	0.44 ± 0.06	3448	
CU Cnc A	2.77	0.4349 ± 0.0012	0.4323 ± 0.0055	3160 ± 150	Torres et al. (2010)
CU Cnc B	2.77	0.3992 ± 0.0009	0.3916 ± 0.0094	3125 ± 150	
GJ 3236 A	0.77	0.376 ± 0.017	0.3795 ± 0.0082	3312 ± 110	Irwin et al. (2009)
GJ 3236 B	0.77	0.281 ± 0.015	0.300 ± 0.011	3242 ± 108	
LP133-373 A	1.63	0.340 ± 0.014	0.33 ± 0.02	3058 ± 195	Vaccaro et al. (2007)
LP133-373 A	1.63	0.340 ± 0.014	0.33 ± 0.02	3144 ± 206	
SDSS 031824-010018 A	0.41	0.2720 ± 0.0200	0.2680 ± 0.0100	3320 ± 130	Blake et al. (2008)
SDSS 031824-010018 B	0.41	0.2400 ± 0.0220	0.2480 ± 0.0090	3300 ± 130	
IRXS J154727.5+450803 A	3.55	0.2576 ± 0.0085	0.2895 ± 0.0068	–	Hartman et al. (2009)
IRXS J154727.5+450803 A	3.55	0.2585 ± 0.0080	0.2895 ± 0.0068	–	
CM Dra A	1.27	0.2310 ± 0.0009	0.2534 ± 0.0019	3130 ± 70	Torres et al. (2010)
CM Dra B	1.27	0.2141 ± 0.0008	0.2398 ± 0.0018	3120 ± 70	
Single-lined eclipsing binaries					
HAT-TR-205-013 B	2.23	0.124 ± 0.010	0.167 ± 0.006	–	Beatty et al. (2007)
HDI86753 B	1.91	0.236 ± 0.017	0.307 ± 0.057	–	Bentley et al. (2009)
TYC7096-222-1 B	8.96	0.286 ± 0.019	$0.263_{-0.071}^{+0.020}$	–	Bentley et al. (2009)

Table 1.1: Continued.

Name	P (days)	M (M_{\odot})	R R_{\odot}	T_{eff} (K)	Ref.
Stars with radii measured interferometrically					
G-J166 A	-	0.877 ± 0.044	0.770 ± 0.021	5269 ± 35	Demory et al. (2009)
G-J570 A	-	0.802 ± 0.040	0.739 ± 0.019	4597 ± 101	Demory et al. (2009)
G-J105 A	-	0.790 ± 0.039	0.708 ± 0.050	-	Ségransan et al. (2003)
G-J845	-	0.762 ± 0.038	0.732 ± 0.006	4568 ± 59	Demory et al. (2009)
G-J879	-	0.725 ± 0.036	0.629 ± 0.051	4711 ± 134	Demory et al. (2009)
G-J380	-	0.670 ± 0.033	0.605 ± 0.020	-	Ségransan et al. (2003)
G-J205	-	0.631 ± 0.031	0.702 ± 0.063	3520 ± 170	Ségransan et al. (2003)
G-J880	-	0.586 ± 0.059	0.689 ± 0.044	3277 ± 93	Berger et al. (2006)
G-J514	-	0.526 ± 0.053	0.611 ± 0.043	3243 ± 160	Berger et al. (2006)
G-J887	-	0.503 ± 0.025	0.459 ± 0.011	3797 ± 45	Demory et al. (2009)
G-J526	-	0.502 ± 0.050	0.493 ± 0.033	3636 ± 163	Berger et al. (2006)
G-J752 A	-	0.484 ± 0.048	0.526 ± 0.032	3368 ± 137	Berger et al. (2006)
G-J15 A	-	0.414 ± 0.021	0.383 ± 0.020	3698 ± 95	Ségransan et al. (2003)
G-J411	-	0.403 ± 0.020	0.393 ± 0.008	3570 ± 42	Ségransan et al. (2003)
G-J687	-	0.401 ± 0.040	0.492 ± 0.038	3095 ± 107	Berger et al. (2006)
G-J191	-	0.281 ± 0.014	0.291 ± 0.025	3570 ± 156	Ségransan et al. (2003)
G-J699	-	0.158 ± 0.008	0.196 ± 0.008	3163 ± 65	Ségransan et al. (2003)
G-J551	-	0.123 ± 0.006	0.141 ± 0.007	3098 ± 56	Demory et al. (2009)
M-stars in post-common envelope binaries					
V471 Tau B	0.52	0.93 ± 0.07	0.96 ± 0.04	-	O'Brien et al. (2001)
RXJ2130.6+4710 B	0.52	0.555 ± 0.023	0.534 ± 0.017	-	Maxted et al. (2004)
DE CVn	0.36	0.41 ± 0.06	$0.37^{+0.06}_{-0.007}$	-	van den Besselaar et al. (2007)
RR Cae	0.30	0.183 ± 0.013	0.19 ± 0.23	-	Maxted et al. (2007)
EC 13471-1258	0.15	0.43 ± 0.04	0.42 ± 0.02	-	O'Donoghue et al. (2003)
NN Ser	0.13	0.111 ± 0.004	0.149 ± 0.002	-	Parsons et al. (2010)

Chapter 2

Absolute properties of CM Draconis and IM Virginis

As explained in Section 1.1 and will be developed later in Section 4.2, the number of well-known DDLEBs with at least one component with a mass below $1 M_{\odot}$ is still scarce. Consequently, new accurate measurements of fundamental properties from binaries of this type are very valuable. The cases of CM Draconis and IM Virginis (hereafter CM Dra and IM Vir, respectively) were found to be very interesting both for their properties and the availability of data. CM Dra is a very low-mass system composed by two similar dM4.5 stars and IM Vir, by two different G7 and K7 stars. The first system is exceptionally important because its components are expected to be fully convective, and thus pivotal to test models in the mass range of this type of stars. The second is a textbook example of systems for testing stellar model predictions since it provides fundamental properties of two different stars with the same age and metallicity that must be fitted simultaneously by theoretical isochrones. New data and the improvement of analysis techniques in the case of CM Dra, and the available data of IM Vir, which were pending of analysis, made the study of these systems worthwhile. The results of the analysis were published in Morales et al. (2009a) and Morales et al. (2009b).

In this chapter, the analysis of the light and radial velocity curves and the determination of the absolute fundamental properties of both systems are described. In the first section, the automatic implementation of the Wilson-Devinney code used to get converged solutions when analyzing several curves simultaneously is presented. The analyses of CM Dra and IM Vir using this code are following.

2.1 Analysis of light and radial velocity curves

In this work, the 2003 version of the WD code¹ was used to fit the observations of CM Dra and IM Vir. The basic concepts of the fits to light and radial velocity curves have been described in Section 1.2. Just as a reminder, the WD code can model these curves by applying differential corrections to a set of initial orbital and physical parameters. Several sets of these initial values are tested to check the consistency of the parameters. The original version of the program was constructed to be iterated manually in order to check the convergence, but here an automatic iterative procedure has been used defining the convergence when differential corrections are smaller than the formal errors of the parameters in three consecutive iterations. Besides, the iterations are carried on further until convergence is repeated for five times. From the five converged solutions, that with the smallest residuals is adopted as the best solution. This automatic convergence code also enables to compute the limb darkening coefficients from theoretical tables at each iteration according to the corrected individual temperatures and gravities, thus making the coefficients of the final solution consistent with the physical properties of the components. The individual effective temperatures rather than their ratio, which is directly determined from the light curves, are then necessary. This is solved in the WD code by fixing a temperature for the primary and fitting that of the secondary. The tables of limb darkening coefficients in the *uvbyUBVR* bands from Claret (2000a) were implemented in this algorithm and used to adjust the data of CM Dra and IM Vir.

As mentioned in Section 1.2, the main advantage of the WD code is the possibility of analyzing different light and radial velocity curves simultaneously in order to obtain accurate fundamental properties coherent with all data sets. This is very important since light curves in different bands constrain better the radius and effective temperature ratios, or in the case of eccentric orbits, eccentricity and argument of the periastron values could be determined consistently by fitting both light and radial velocity curves, which are basically sensitive to $e \cos \omega$ and $e \sin \omega$, respectively.

However, care has to be taken when combining different curves, in particular when light curves are affected by spots. The timescale of the evolution of activity features on active stars could be of a few months, consequently, the spot configuration, and its effect on light curves may be different for different epochs of observation. In this case, spot parameters cannot be fitted simultaneously for different epochs and a separate pre-analysis has to be carried out. The spot effect on radial velocity curves should also be taken into account. Usually radial velocity curves of DDLEBs are obtained over long campaigns of observation. Therefore, additional jitter on these curves may be present due to the temporal evolution of spots. In this

¹Subsequent updates in this code do not affect the fitting mode used for detached binaries.

case, an estimation of the corrections produced by different spot configurations in the radial velocity parameters should be performed to obtain reliable uncertainties of the absolute properties of the components.

The possibility of analysing several curves simultaneously with the WD code has been used in this work whenever possible. In such cases, the residuals of each curve is used in order to give different weights to the curves according to their quality.

2.2 CM Draconis

CM Dra (also GJ 630.1 A, $\alpha = 16^{\text{h}}34^{\text{m}}20^{\text{s}}.41$, $\delta = +57^{\circ}9'43''.94$, J2000.0) is a $V = 12.0$ mag eclipsing binary discovered by Eggen & Sandage (1967). It was found to form a common proper motion pair moving at a speed of $\sim 2''\text{yr}^{-1}$ with a $V = 15$ mag white dwarf (GJ 630.1 B, $\alpha = 16^{\text{h}}34^{\text{m}}21^{\text{s}}.64$, $\delta = +57^{\circ}10'8''.3$, J2000.0) at a distance of $26''$. Figure 2.1 shows the proper motion of this pair on the sky. This DDLEB was first spectroscopically and photometrically analyzed by Lacy (1977) and new radial velocity curves were obtained by Metcalfe et al. (1996). Their results indicated that CM Dra is composed by two similar dM4.5 main sequence stars with masses of about $0.23 M_{\odot}$ and $0.21 M_{\odot}$, orbiting each other with a period of approximately 1.27 days. This confirmed the components of CM Dra as the first fully convective stars with accurate determinations of masses and radii.

Unlike other well-known DDLEBs, the orbit of CM Dra is somewhat eccentric. This peculiar feature makes this system even more interesting because properties about its internal structure can be inferred. The internal structure constant (k_2 see Kopal 1978, for reference) of the components, related to the density profile of the stars, can be estimated through the analysis of the apsidal motion of the system (Kopal 1978; Claret & Giménez 1993), enhancing the importance of this binary system.

New photometric observations of this system and improvements on the fitting methods of light and radial velocity curves, as well as the importance of this system due to the reasons mentioned (fully convective components and eccentric orbit) justified the reanalysis of CM Dra. The fitting of the photometric and spectroscopic data and the study of the times of minima that yielded the apsidal motion are described in this section.

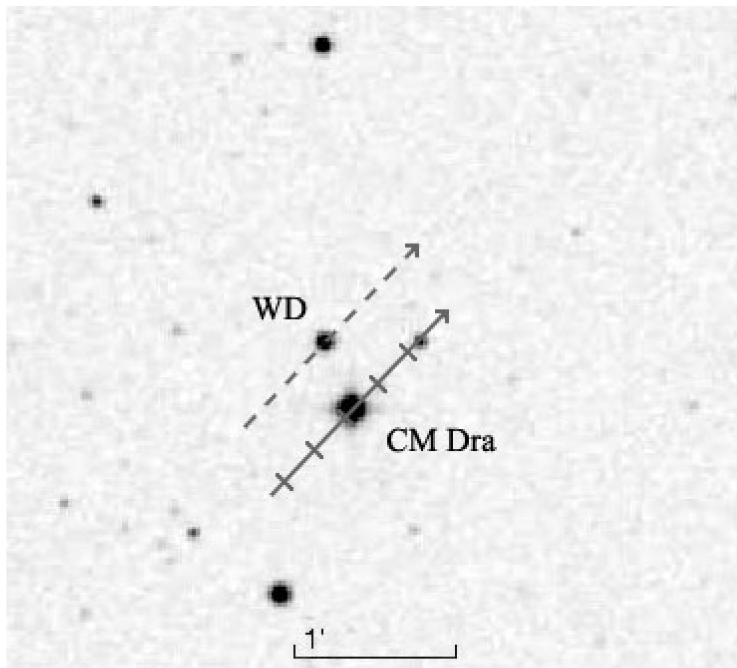


Figure 2.1: POSS-II DSS2 image in the R band showing the position of CM Dra at epoch 1991.5 and its proper motion on the sky. The common proper motion white dwarf companion is labeled "WD". Tick marks on the path of CM Dra are given in steps of 10 years from 1970 to 2010. North is up and East is left.

2.2.1 Observations

The photometric follow-up observations of the CM Dra system come from the different sources that are summarized in Table 2.1. The photometric light curve in the I band published by Lacy (1977) has been used as well as more recent observations from different observatories. Six light curves in the Cousins R and I bands taken at different epochs with the 0.8 m Four College Automatic Photoelectric Telescope (hereafter FCAPT) located at Fairborn Observatory (Arizona, USA) were kindly provided by E. F. Guinan. Finally, a light curve in the Sloan r' filter observed during the Trans-Atlantic Exoplanet Survey (TrES) with the Sleuth telescope at Palomar Observatory (California, USA) were handed by D. Charbonneau. Details on the reduction of observations to derive the differential magnitudes of these curves can be found in the Appendix A. In our automatic convergence algorithm of the WD code, the limb darkening coefficients for the Sloan r' band are not implemented. However, tests during the analysis of the Sleuth light curve did not show any difference between fits with the Cousins R -band limb darkening coefficients and those

Table 2.1: Summary of photometric observations of CM Dra

Epoch	Observatory and telescope	Band	Observations	Ref.
1976 (Apr 25th–Aug 6th)	McDonald Obs., 91 cm refl.	<i>I</i>	830	1
1996 (Mar 30th–Jul 5th)	Fairborn Obs., FCAPT	<i>R</i> and <i>I</i>	1235 and 1220	2
1997 (Feb 20th–Jul 2nd)	Fairborn Obs., FCAPT	<i>R</i> and <i>I</i>	1025 and 1017	2
1998 (Apr 10th–Jul 3rd)	Fairborn Obs., FCAPT	<i>R</i> and <i>I</i>	1141 and 1154	2
1999 (Feb 7th–May 24th)	Fairborn Obs., FCAPT	<i>R</i> and <i>I</i>	505 and 509	2
2000 (Feb 27th–Jul 5th)	Fairborn Obs., FCAPT	<i>R</i> and <i>I</i>	1214 and 1163	2
2001 (Apr 28th–Jun 29th)	Fairborn Obs., FCAPT	<i>R</i> and <i>I</i>	585 and 596	2
2004 (Mar 29th–Jun 6th)	Palomar Obs., Sleuth	<i>r'</i>	8302	3

Ref.: 1. Lacy (1977). 2. E. F. Guinan (private communication). 3. D. Charbonneau (private communication)

corresponding to the Sloan *r* band (compatible with Sloan *r'*) computed from Claret (2004). Thus, the Cousins *R* band was subsequently used to fit this curve in order to update the limb darkening coefficients at each iteration.

Radial velocities of CM Dra were obtained from the same spectroscopic observations used by Metcalfe et al. (1996) taken with an echelle spectrograph on the Tillinghast reflector at the F. L. Whipple Observatory (Arizona, USA). Each spectrum covers approximately 45 Å centered on the Mg I b triplet at ~ 5187 Å and were reanalyzed with improved techniques using TODCOR (Zucker & Mazeh 1994) to derive the individual radial velocities (kindly provided by G. Torres). A spectrum of Barnard’s star (GJ 699, M4Ve), taken with similar instrumentation, was used as template for both the primary and the secondary components of CM Dra. The rotations of each component were matched by convolving the template with standard rotational profiles. The projected rotational velocities that best match the observations were $10.0 \pm 1.0 \text{ km s}^{-1}$ and $9.5 \pm 1.0 \text{ km s}^{-1}$ for the primary and the secondary components, respectively. These values were used to derive the radial velocities from the observations. An average light ratio $L_2/L_1 = 0.91 \pm 0.05$ at the mean wavelength of the spectra was found from the analysis. This value can be used to check the consistency of the light ratios derived from light curves. Other templates for stars such as GJ 275 A (M3.5V) and GJ 51 (M5.0V) were tested to check for systematic errors due to template mismatch, but without any improvement. See Appendix A for further details.

The effect of photospheric spots is clearly visible in the light curves as modulations in the out-of-eclipse phases and may also be present on the radial velocity curves. This is not surprising since the short period may be indicative of tidal locking. Thus, the components of CM Dra may be rapid rotators that in the presence of magnetic fields trigger high levels of magnetic activity. This has been also confirmed by the detection of flares (Eggen & Sandage 1967; Lacy et al. 1976; Kozhevnikova et al. 2004; Nelson & Caton 2007) and X-ray emission. For this reason, the distortions caused by the different spot configurations in each season need to be corrected

prior to the combination of the curves. This is done in a separate pre-analysis of each light curve. For the radial velocity curves, this correction would have also been possible if spectroscopic observations were contemporaneous with light curves, but this is not the case. Besides, radial velocities span approximately 5 years of observations. Thus, the jitter due to the changing configuration of spots can not be properly corrected by a single fit. In any case, spot effects on the radial velocity parameters can be estimated and added to the uncertainties.

2.2.2 Pre-analysis of light and radial velocity data

In order to fit all the light curves simultaneously with the WD code, the effect of photospheric spots from different epochs must be corrected first. The pre-analysis was also used to correct for third light differences between epochs. This was done because, due to the high proper motion of CM Dra, it is approaching an $R = 16.5$ mag star (see Figure 2.1) that may contaminate the photometry in a different amount depending on its relative distance and the photometric aperture used to obtain the measurements. Thus, a correction for third light was also implemented at the same time as the correction for spots.

The pre-analysis was performed by fitting the light curves from different epochs separately with the spots and third light parameters set as free. FCAPT R - and I -band light curves from the same season were used simultaneously to derive consistent parameters. The fits were started with the parameters of the binary reported in Metcalfe et al. (1996) and solved the different light curve seasons for the eccentricity (e), the initial argument of periastron (ω), the inclination (i), the temperature ratio ($T_{\text{eff}2}/T_{\text{eff}1}$), the pseudo-potentials (Ω_i) and the passband specific luminosity ratio (L_2/L_1). We also fitted the parameters of spots, the size (r_s), the longitude (ϕ_s), the latitude (θ_s) and the temperature contrast relative to the photosphere (T_s/T_{eff}), and the third light (ℓ_3) on each passband. The size, the temperature contrast and the latitude of the spots are strongly correlated, so we started computing solutions with variable ϕ_s and r_s for several fixed values of θ_s and dark and bright spots with moderate temperature contrast. Several scenarios with spots on different components or more than one spot were tested and once convergence was reached, ϕ_s and r_s were fixed and we solved for θ_s and T_s/T_{eff} . If convergence was not reached in this final stage, those fits with the fixed values of θ_s and T_s/T_{eff} that yielded the smallest residuals were selected as best solutions. The spot and third light parameters that best matched the light curves are given in Table 2.2. Figures of all these light curves with their best fits and the residuals are compiled in Appendix A.

The corrections for spots and third light in each season were computed from the differences between the theoretical curves from these fits and the theoretical curves

Table 2.2: Spot and third light parameters fitted to light curves of each season. Third light is given as the percentage of the total light at phase 0.25. Parameters labeled as fixed were obtained from the trial fits giving the best residuals.

	Star	Spots			T_s/T_{eff}	ℓ_3 (%)	
		θ ($^\circ$)	ϕ ($^\circ$)	r_s ($^\circ$)		R band	I band
Lacy (1977) 1976	1	21 \pm 8	76 \pm 5	42 \pm 3	0.94 \pm 0.02	–	1.3 \pm 0.8
FCAPT 1996	2	45 (fixed)	338 \pm 6	13 \pm 1	1.09 (fixed)	4.1 \pm 1.2	2.3 \pm 1.2
FCAPT 1997	1	30 (fixed)	316 \pm 7	32 \pm 6	0.96 (fixed)	3.4 \pm 1.2	3.0 \pm 1.2
	2	30 (fixed)	304 \pm 12	12 \pm 5	1.09 (fixed)		
FCAPT 1998	1	30 (fixed)	315 \pm 7	40 \pm 2	0.96 (fixed)	4.4 \pm 0.8	3.3 \pm 0.8
FCAPT 1999	1	45 (fixed)	119 \pm 11	15 \pm 3	1.09 (fixed)	4.8 (fixed)	2.9 (fixed)
	1	45 (fixed)	255 \pm 11	19 \pm 7	0.96 (fixed)		
FCAPT 2000		Spot modulation not significant				5.5 \pm 1.7	3.6 \pm 1.7
FCAPT 2001	1	30 (fixed)	297 \pm 8	23 \pm 3	1.09 (fixed)	1.4 \pm 1.7	1.6 \pm 1.7
Sleuth 2004	2	45 (fixed)	273 \pm 2	32 \pm 1	0.96 (fixed)	12.3 \pm 0.9	–

with the same geometric properties but without spots and third light. These differences were subtracted from the original data. Figure 2.2 shows the differential effect of spots on the *I*-band light curve of Lacy (1977) as an example. Without spots and third light, the light curves can be combined in the WD code. However, fits with the WD code to the large number of data points that comprise these light curves would have taken a long time, in particular for CM Dra due to its eccentric orbit. Therefore, for practical reasons, all the FCAPT seasons were combined in two single light curves, one for each band, and subsequently binned by averaging the observations in the out-of-eclipse phases with bins of 0.04 in phase. The same binning was also applied to the Sleuth light curve. The resulting light curves contain 5356 data points. Unit weight was assigned to observations that had no reported errors, as is the case of FCAPT and Lacy (1977), and individual weights were used for Sleuth data. For the out-of-eclipse averages computed for FCAPT and Sleuth, the number of combined points and the reciprocal of the standard deviation squared were used as weights, respectively.

The spot scenarios fitted in the light curves were also used to estimate their effect on the radial velocity curves of CM Dra. The differentials between spotted and non-spotted velocity curves were computed with the WD code and applied to the radial velocities. Figure 2.3 shows that these differentials are always below 0.2 km s⁻¹, except during the eclipse phases when Rossiter-McLaughlin effect is important, but few data points are affected. These corrections are much smaller than the reported uncertainties of the individual measurements, thus, they are not expected to modify the parameters of the fits significantly. Keplerian fits to the different sets of radial velocities were carried out and the differences in the key parameters were below 0.25% and 0.12% for the primary and the secondary minimum masses, respectively, and below 0.1% for the projected semimajor axis, always within the errors of the canonical solution as expected. However, to be conservative, half of the maximum

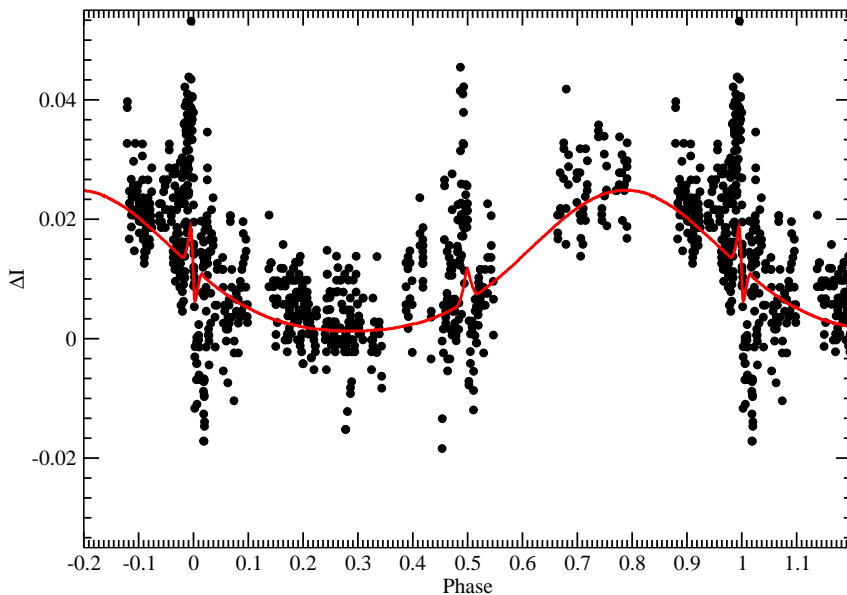


Figure 2.2: Differential effect of star spots on the I -band light curve of Lacy (1977). The solid line represents the model described in the text.

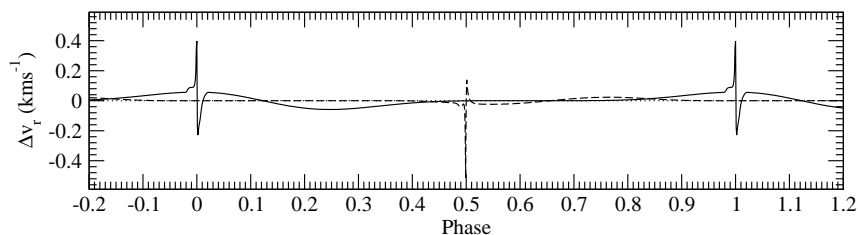


Figure 2.3: Differential effect of spots on the radial velocity curves of CM Dra. The primary and the secondary component differential velocities are plotted as solid and dashed lines, respectively. This example corresponds to the spot scenario fitted to the 1997 FCAPT data. The differentials are computed as the curve with spots minus the curve without spots.

difference in each parameter was added in quadrature to the final uncertainty of each parameter.

2.2.3 Analysis of light and radial velocity curves

The final set of light and radial velocity curves consisted in two light curves in the I band, Lacy (1977) and FCAPT I data with 830 and 1691 data points, respectively, and two more in the R band, FCAPT R and Sleuth data with 1656 and 1179 data

points, respectively. Besides, the radial velocity curve of each component contains a total of 233 data points. In order to combine appropriately these data, the times of observation were transformed to the uniform Terrestrial Time (TT) scale to avoid discontinuities resulting from the more than 30 leap seconds that have been introduced between the first and the last seasons of observation.

The WD code was used to analyze these curves. The reflection albedos were fixed to 0.5, appropriate for convective envelopes, and a value of 0.2 was adopted for the gravity brightening of each component according to Claret (2000b). The square root limb darkening law was used with coefficients computed from theoretical tables as mentioned in Section 2.1.

In a first attempt, the light and radial velocity curves were fitted simultaneously by solving for the epoch of primary eclipse (T_0), the eccentricity (e), the initial argument of periastron (ω_0), the inclination (i), the semimajor axis (a), the systemic radial velocity (γ), the mass ratio (M_2/M_1), the secondary effective temperature ($T_{\text{eff}2}$), the luminosity ratio at each bandpass (L_2/L_1), and the surface pseudo-potentials (Ω_j). The effective temperature of the primary was fixed to $T_{\text{eff}1} = 3100$ K according to Viti et al. (1997, 2002) in order to properly compute the limb darkening coefficients, and $T_{\text{eff}2}$ was fitted instead of the temperature ratio. Since the data span over 30 years and apsidal motion is expected to be present for CM Dra, the period (P) and the apsidal motion rate ($\dot{\omega}$) were also set as free. This procedure did not yield satisfactory fits, giving values for $\dot{\omega}$ not significant in comparison with its large error. Thus, the best option to solve the system was found to be by fixing $\dot{\omega}$ to zero and fitting the light curves separately in order to avoid systematic effects of changes of ω from epoch to epoch. To be consistent, the period was fixed to $P = 1.268389985 \pm 0.000000005$ days as obtained analyzing times of minima and accounting for the effect of $\dot{\omega}$ as described later in Section 2.2.4.

An iterative procedure was performed to fit all the light curves and the radial velocity curves consistently. Light curve parameters adjusted to the different light curves were weight averaged, and subsequently fixed to fit the radial velocity curves. These iterations between fits of light curves and fits of radial velocity curves were repeated until convergence, considered when changes from one iteration to the next were smaller than the errors reported by the WD code. Fits to the light curves are shown in Figures 2.4 and 2.5. The results for the different seasons, as well as the average values taken as the best solution, are listed in Table 2.3. These averages were computed by weighing each solution according to the inverse of the square of the rms of the fits. To be conservative, the uncertainties of each parameter were computed as the quadratic addition of the standard deviation from the different fits and the internal maximum error given by the WD code. The final solution shows that both components in CM Dra are perfectly spherical, showing identical radius

Table 2.3: Light curve parameters adjusted to the different epochs of observation of CM Dra and their weighted average.

Parameter	Lacy	FCAPT	Sleuth	Average
Physical properties				
T_0 (HJD-2400000)	42958.620510(24)	51134.661970(13)	53127.302690(21)	48042.32743(24) ^a
e	0.00521(56)	0.00686(50)	0.00424(56)	0.0054(13)
ω_0 ($^\circ$)	108.1(2.2)	101.9(0.9)	113.9(3.8)	107.6(6.3)
i ($^\circ$)	89.784(64)	89.770(28)	89.712(62)	89.769(73)
Ω_1	15.736(50)	15.877(39)	15.862(61)	15.79(11)
Ω_2	15.631(59)	15.506(40)	15.582(75)	15.59(10)
r_1^b	0.06757(12)	0.06700(12)	0.06690(17)	0.0673(5)
r_2^b	0.06350(17)	0.06403(12)	0.06377(17)	0.0637(4)
Radiative properties ($T_{\text{eff}1} = 3100$ K)				
$T_{\text{eff},2}/T_{\text{eff},1}$	0.9984(7)	0.9926(4)	0.9923(5)	0.9960(40)
$(L_2/L_1)_R^c$	–	0.8721(32)	0.8632(63)	0.8654(89)
$(L_2/L_1)_I^c$	0.8764(43)	0.8782(33)	–	0.8768(44)
Other quantities pertaining to the fits				
σ_R (mag)	–	0.0236	0.0137	
σ_I (mag)	0.0071	0.0130	–	
N_{obs}	830	1656 (R) , 1691 (I)	1179	

^aReference epoch of each light curve corrected to a central epoch.^bVolume radii.^cLight ratio computed at orbital phase 0.25.

(within the uncertainties) in the pole direction (r_{pole}) and in the direction between the components (r_{point}) computed by the WD code.

The radial velocity curve fits are displayed in Figure 2.6 and the parameters retrieved are listed in Table 2.4. Eccentricity and initial argument of periastron are consistent with those derived from the light curves within the errors. The uncertainties of the relevant parameters due to spots derived in Section 2.2.2 were added quadratically to this solution.

The parameters derived from light and radial velocity curves are very similar to those reported by Lacy (1977) and Metcalfe et al. (1996) with the exception of the relative radius of the secondary component (r_2). The solution given here is a significant 2.1% higher than that determined by Lacy (1977). This discrepancy was found to be due to the treatment of the light curve by Lacy (1977). In that work, the fits were performed with a much simpler model (Russell & Merrill 1952) than that used by the WD code, and the effect of spots was removed with a sinusoidal fit to the out-of-eclipse phases. This correction does not take into account the occultation or appearance of spots during eclipses that deviate the effect of spots from a pure sinusoidal shape (see Figure 2.2). Besides, in Lacy (1977) the system was assumed to be circular due to its very low eccentricity. In order to check this hypothesis, a test to Lacy's light curve was performed. The modeling code Eclipsing Binary Orbit

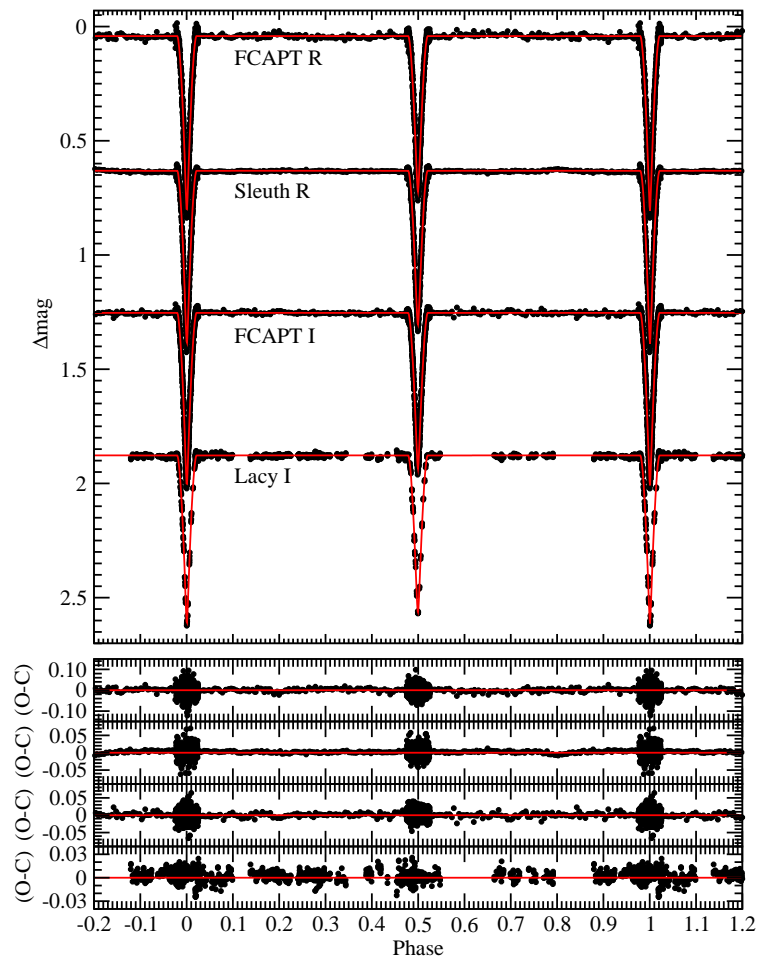


Figure 2.4: Light curves of CM Dra after subtracting the effect of spots and third light and with out-of-eclipse phases binned. Solid lines are the best fits to each curve and the lower panels show the residuals in the same order as arranged in the top panel. Note the different scales of the residuals of each dataset.

Program (EBOP Etzel 1981; Popper & Etzel 1981), that does not consider spots, was used to fit Lacy’s data assuming a circular orbit and removing the spot effect with a sinusoidal fit. Similar results as those of Lacy (1977) were found, indicating that the modelling code is relatively unimportant. If the effect of spots on the light curve is removed as described in Section 2.2.2 and $e = 0$ is still fixed, the relative radius r_2 (and the sum of radii) fitted with EBOP is somewhat increased. If the eccentricity is also set as free parameter, then r_2 is close to the value obtained with the WD code. These results indicate that the adjusted parameters obtained here are

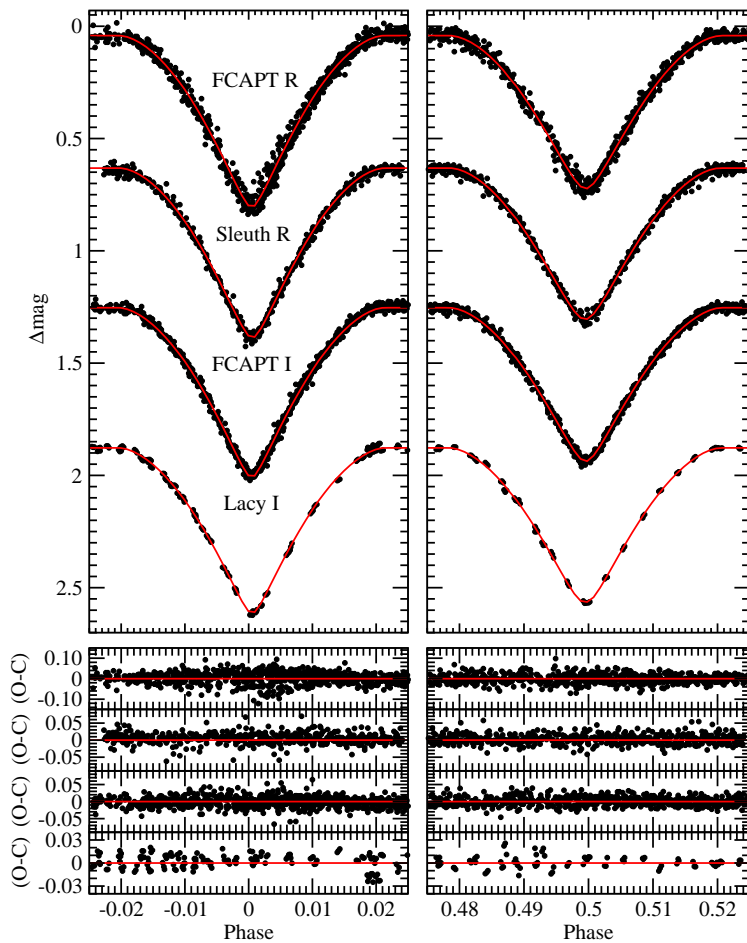


Figure 2.5: Enlargement of Figure 2.4 during the eclipse phases.

likely free from systematics due to spot or eccentricity effects.

2.2.4 Analysis of eclipse timings

Both General Relativity and the classical theory of tides predict a certain degree of advance of periastron for eccentric close binary systems. This apsidal motion depends on the mass distribution in the interior of the components, and thus properties of this profile can be determined. As already mentioned, the eccentricity of CM Dra makes the determination of the apsidal motion possible. Although light curves do not provide good estimates of its value, it can be determined through the analysis of eclipse timings.

Table 2.4: Radial velocity solution for CM Dra.

Parameter	Value
Adjusted quantities	
T_0 (HJD)	$2446058.56471 \pm 0.00026$
e	0.0051 ± 0.0013
ω_0 ($^\circ$)	129 ± 16
a (R_\odot)	3.7634 ± 0.0046
γ (km s^{-1}) ^b	-118.24 ± 0.07
Derived quantities	
M_2/M_1	0.9267 ± 0.0023
K_1 (km s^{-1})	72.23 ± 0.13
K_2 (km s^{-1})	77.95 ± 0.13
RMS residuals from the fits	
Primary (km s^{-1})	1.30
Secondary (km s^{-1})	1.40

^aThe true uncertainty of γ may be larger due to external errors.

Due to the intrinsic peculiarity of CM Dra and its brightness and eclipse depths, this system is an easy target for observations. Many observers have been interested on this system for different purposes, as a consequence, like in the case of light curves, many eclipse timings have been measured from different observatories. Photoelectric and CCD minima timings were collected from the light curves analyzed in the previous section, from the literature (Lacy 1977; Deeg et al. 2000, 2008; Dvorak 2005; Smith & Caton 2007), and also from different observatories: 63 minima from Bradstreet Observatory (Pennsylvania, D. H. Bradstreet, private communication), 20 from Ondřejov Observatory (Czech Republic, M. Wolf, private communication), 8 from La Palma Observatory (Canary Islands, G. Anglada, private communication) and 1 more from F. L. Whipple Observatory (Arizona, D. W. Latham, private communication). Further references for the minima timings are given in Appendix A and the complete list of 200 times of eclipse (101 for the primary and 99 for the secondary) is available in Morales et al. (2009a). All these timings were converted to the uniform TT scale. They cover more than 30 years of observations but with an unfortunate gap of nearly 18 years.

According to Giménez & Bastero (1995), the eclipse timings of a binary system with apsidal motion can be written as:

$$T_j = T_0 + P \left(E + \frac{j-1}{2} \right) + (2j-3) A_1 \frac{eP}{2\pi} \cos \omega + \mathcal{O}(e^2), \quad (2.1)$$

where E is the cycle number, A_1 is a coefficient dependent on the inclination and the eccentricity, and j indicates primary or secondary eclipse (1 and 2, respectively). The third term is the correction to the linear ephemeris due to the apsidal motion. The term on e^2 introduces corrections of about 0.2 s to this equation for the case

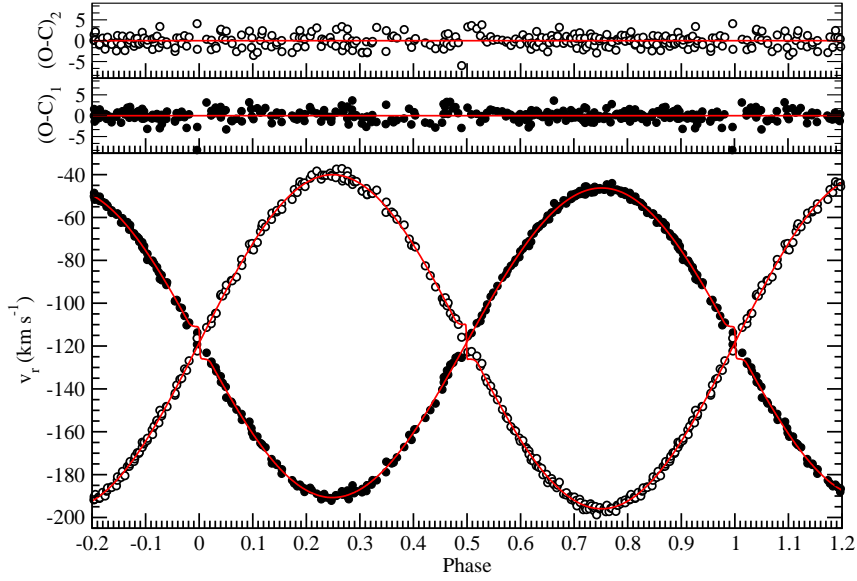


Figure 2.6: Best fits to the radial velocity curves of CM Dra. Primary and secondary components are shown as filled and open symbols, respectively. Residuals of the fits are plotted on the upper panels.

of CM Dra, so it can be neglected given the accuracy of the measurements of the minima timings.

According to the prescriptions of Giménez & Bastero (1995), since the inclination of CM Dra is close to 90° , $A_1 \approx 2$. Thus, given the CM Dra eccentricity from the light curve analysis and the period, Equation 2.1 predicts a sinusoidal shape of the apsidal motion term on the eclipse timings with a 180° phase difference between the primary and the secondary and a semi amplitude of about 188 s. Assuming a constant apsidal motion rate ($\dot{\omega}$), the argument of the periastron can be written as:

$$\omega = \omega_0 + \dot{\omega} \cdot E. \quad (2.2)$$

In the approximation of small values of $\dot{\omega}E$, Equation 2.1 is transformed into:

$$T_j \simeq T_0 + P \left(E + \frac{j-1}{2} \right) + (2j-3) A_1 \frac{eP}{2\pi} (\cos \omega_0 - \sin \omega_0 \cdot \dot{\omega}E). \quad (2.3)$$

This equation can be re-defined as a linear equation on E as:

$$(O - C)_j = \mathcal{T}_{0,j} + \mathcal{P}_j E, \quad (2.4)$$

where $\mathcal{T}_{0,j}$ represents an effective epoch of reference for each type of eclipse and \mathcal{P}_j , their corresponding period. From these values, the ephemeris of the binary can be

determined as:

$$P = \frac{\mathcal{P}_1 + \mathcal{P}_2}{2}, \quad (2.5)$$

$$T_0 = \frac{\mathcal{T}_{0,1} + \mathcal{T}_{0,2}}{2} - \frac{P}{4}. \quad (2.6)$$

And the initial argument of the periastron and the total apsidal motion rate as:

$$\omega_0 = \cos^{-1} \left(\frac{2\pi}{A_1 e P} \frac{\mathcal{T}_{0,2} - \mathcal{T}_{0,1} - \frac{P}{2}}{2} \right), \quad (2.7)$$

$$\dot{\omega} = \left(\frac{2\pi}{A_1 e P \sin \omega_0} \frac{\mathcal{P}_1 - \mathcal{P}_2}{2} \right). \quad (2.8)$$

This last equation indicates that apsidal motion is present when the observed periods for the primary and the secondary eclipses are different.

Following these equations, linear fits were performed to the times of minima. Figure 2.7 shows the observed minus computed values ($O - C$) of the times of minima and the linear fits obtained. The scatter of these measurements is large, in fact, larger than the typical error bars assigned. This larger scatter may be, in part, due to the presence of photospheric spots on the components of CM Dra. A simple test simulating the light curves with the spot properties given in Table 2.2 confirmed this scenario. A bias of up to 15 s was found between the minima timings of these curves and those of the corresponding unspotted light curves. Similar results were found by Hargis et al. (2000). In order to account for this fact, linear fits to the times of minima were performed but doubling the internal errors of the measurements in order to preserve the relative weights but obtaining a χ^2 closer to unity that yield much more reliable uncertainties for the parameters. Tests adding 15 s in quadrature to the internal error bars gave similar results. Table 2.5 lists the parameters found from these linear fits and the ephemeris, the apsidal motion rate derived and the initial argument of the periastron, which is consistent with the value found from the light curve analysis.

2.2.5 Absolute properties

The orbital and physical parameters determined from fits of the light and radial velocity curves of CM Dra provide direct determinations of the masses and radii of the components independently of any distance or flux calibration. These values are reported in Table 2.6. The rotational velocities of the primary and secondary components can be derived from the absolute radii and the period assuming pseudo-synchronization, giving, $10.22 \pm 0.08 \text{ km s}^{-1}$ and $9.67 \pm 0.07 \text{ km s}^{-1}$, respectively.

Table 2.5: Results of the linear fits to the times of minima of CM Dra.

Properties	Weighted fit
Quantities from linear fits	
$\mathcal{T}_{0,1}$ (HJD)	$2448042.32778 \pm 0.00002$
\mathcal{P}_1 (s cycle ⁻¹)	$1.2683899936 \pm 0.0000000064$
χ_1^2	1.303
$\mathcal{T}_{0,2}$ (HJD)	$2448042.96084 \pm 0.00002$
\mathcal{P}_2 (s cycle ⁻¹)	$1.2683899765 \pm 0.0000000069$
χ_2^2	0.920
P (days)	$1.268389985 \pm 0.000000005$
T_0 (HJED)	$2448042.327214 \pm 0.000014$
Derived quantities	
ω_0 (°)	104.9 ± 3.7
$\dot{\omega}$ (° cycle ⁻¹)	$(2.3 \pm 1.4)10^{-4}$
U (years)	5400 ± 3200

These values are in accordance with those derived from the spectra ($9.5 \pm 1.0 \text{ km s}^{-1}$ and $10.0 \pm 1.0 \text{ km s}^{-1}$, see Section 2.2.1).

In order to determine the individual effective temperatures of the stars, an absolute value for one of them must be assumed. During the light curve fitting, a value of 3100 K was adopted for the primary, but it could be refined using the apparent magnitudes and the parallax of the system. IR magnitudes are preferred because the bolometric magnitudes are less dependent on the effective temperature and the chemical composition. The 2MASS magnitude $K_s = 7.796 \pm 0.021$ (Cutri et al. 2003), transformed to the Johnson system following Carpenter (2001), and the parallax $\pi = 69.2 \pm 2.5 \text{ mas}$ (van Altena et al. 1995) were used to derive the individual temperatures by an iterative procedure. Starting from the initial value $T_{\text{eff}1} = 3100 \text{ K}$, and the temperature ratio determined from light curves, the effective temperature of the secondary component can be determined and then a bolometric correction for each star can be computed using the theoretical tables in Bessell et al. (1998). The total luminosity $L_1 + L_2$ is subsequently computed from the K_s magnitude, the bolometric corrections and the parallax. A ratio of the bolometric luminosities can be derived from the light curve parameters as:

$$\frac{L_2}{L_1} = \left(\frac{r_2}{r_1}\right)^2 \left(\frac{T_{\text{eff},2}}{T_{\text{eff},1}}\right)^4 = 0.880 \pm 0.022. \quad (2.9)$$

Thus, individual bolometric luminosities are easily derived from $L_1 + L_2$ and L_2/L_1 , and from them and the individual radii, the individual temperatures. The process was iterated until corrections of temperatures were below 1 K and checked from different starting points of $T_{\text{eff}1}$. The final mean bolometric correction and the total luminosity were 2.66 ± 0.05 and $0.0104 \pm 0.0009 L_\odot$, respectively. These values

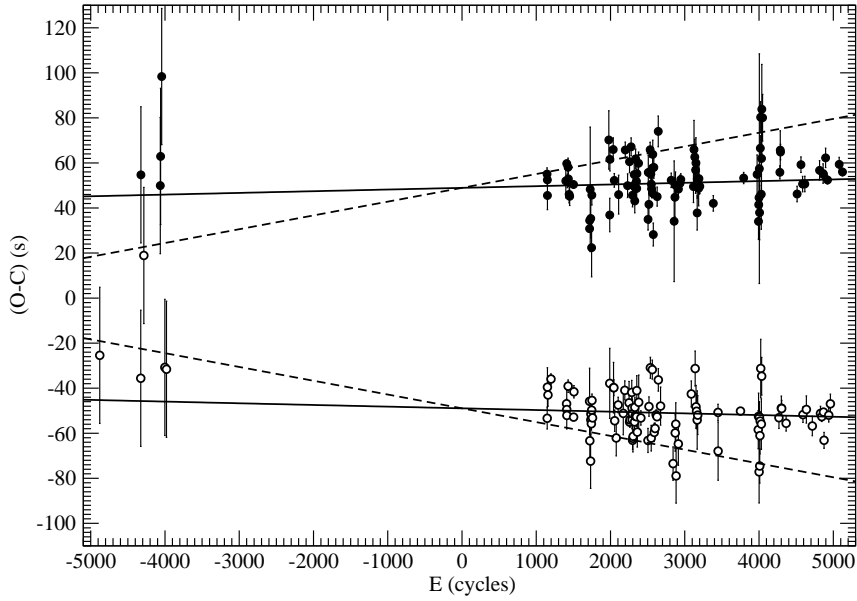


Figure 2.7: Observed minus computed residuals ($O-C$) from the times of minima of CM Dra. Primary and secondary eclipses are represented as filled and open symbols, respectively. Solid lines are the best linear fits obtained and dashed lines are the theoretical predictions (see Section 3.2.2).

Table 2.6: Absolute physical properties of the components CM Dra.

Properties	Component 1	Component 2
$M (M_{\odot})$	0.2310 ± 0.0009	0.2141 ± 0.0010
$R (R_{\odot})$	0.2534 ± 0.0019	0.2396 ± 0.0015
$\log g$ (cgs)	4.994 ± 0.007	5.009 ± 0.006
T_{eff} (K)	3130 ± 70	3120 ± 70
$\log(L/L_{\odot})$	-2.258 ± 0.038	-2.313 ± 0.056
Age (Gyr)	4.1 ± 0.8 (Main Sequence)	
$[M/H]$	$-1 < [M/H] < -0.6$	

$M_{\text{Bol}\odot}=4.74$ is used to compute luminosities (Bessell et al. 1998).

yielded the individual temperatures and luminosities reported also in Table 2.6.

The final temperatures were used to determine the light ratio in the V band scaling *NextGen* atmosphere models (Hauschildt et al. 1999) to the R and I light ratios derived from light curves. The result found was $(L_2/L_1)_V = 0.86 \pm 0.15$ and is in accordance with the value of 0.91 ± 0.05 derived from the spectra in Section 2.2.1, thus confirming the self-consistency of the fits. As a check, temperature-color cali-

brations for dwarf stars from Casagrande et al. (2008) were also used to derive the individual temperatures from different colors indices and independently of light curve parameters or parallax. This yielded a mean temperature of 3050 ± 50 K similar to that found from K_s and the parallax.

Age and chemical composition, along with mass, are the fundamental properties that determine the evolutionary status of a star. Little was known about both of them for CM Dra. This system was regarded to belong to Population II due to its high proper motion, however no clear correlation between kinematics and metallicity or age is found for stars in the solar neighborhood (Nordström et al. 2004).

Regarding the age, some insight can be obtained from the white dwarf common proper motion companion of CM Dra. According to Bergeron et al. (2001) the cooling age and estimated mass of this white dwarf are 2.84 ± 0.37 Gyr and $0.63 M_{\odot}$, respectively. According to the initial-to-final mass relationship of white dwarfs in Catalán et al. (2008), a mass of $2.1 \pm 0.4 M_{\odot}$ can be estimated for the progenitor star. A star with such mass would have a life span of approximately 1.3 Gyr (Girardi et al. 2000), thus deriving a total age of 4.1 ± 0.8 Gyr for the system (the uncertainty coming from the uncertainties in the mass and the chemical composition of the progenitor star). Considering the same age for CM Dra, it follows that the components are in the main-sequence phase of evolution.

Attempts to determine the metallicity of CM Dra were carried out by Viti et al. (1997, 2002) by performing fits to the spectral energy distribution and to several spectral features using stellar atmosphere models. A range $-1.0 < [M/H] < -0.6$ was suggested, but systematic differences in the results from optical and near-IR spectra cast some doubts on this result. Fits using the most recent version of the *NextGen* models did neither clarify the scenario, thus the metallicity of CM Dra is still, unfortunately, poorly determined.

2.3 IM Virginis

IM Virginis (also HD 111487, 1E 1247.0–0548, $\alpha = 12^{\text{h}}49^{\text{m}}38^{\text{s}}70$, $\delta = -6^{\circ}04'44''9$, J2000.0) is a $V = 9.57$ mag eclipsing binary discovered as an X-ray source with the Einstein Observatory by Helfand & Caillault (1982). Radial velocity variability was found by Silva et al. (1987), and spectroscopic and photometric follow-up carried out by Marschall et al. (1988, 1989) confirmed this system to be a DDLEB composed by a G7 and a late-K or M star with an orbital period of 1.3085 days.

Very little is known from this binary since these first publications apart from

sparse photometry and some detections of chromospheric activity and X-ray flaring (Strassmeier et al. 1993; Pandey & Singh 2008). These publications indicate that, as expected from the period, the components of this system are magnetically active, as in the case of CM Dra. The large spectral type difference of the components is indicative of two stars with a large mass difference. Systems with this property are especially interesting for stellar model testing since they provide two separate points in the mass-radius and mass-effective temperature diagrams that must be fitted simultaneously with the same age and chemical composition.

This section describes the analysis of the light and radial velocity curves carried out on the available data for this system in order to derive its physical properties with sufficient accuracy to test stellar structure and evolution models. This work was done during a research stay at the Harvard-Smithsonian Center for Astrophysics in collaboration with G. Torres.

2.3.1 Observations

The photometric time-series observations of IM Vir were taken at the Gettysburg College Observatory (Pasadena, USA) with a CCD camera mounted on a 0.4-m Ealing Cassegrain reflector. Differential photometry in the Bessell *BVRI* bands was obtained between April and May in 2006 and kindly provided by L. A. Marschall. Details on these observations can be found in Appendix B.

The raw photometry was affected by subtle trends as revealed by the differential photometry of the comparison and check stars (BD-05 3573 and HD 111427, respectively). Thus, the differential photometry of IM Vir was de-trended by removing the median value of the comparison minus check star photometric differences computed over intervals of few hours. The second part of the photometry still showed a systematic difference of about 0.01 magnitudes with respect to the first half of the photometry. This was assumed to be due to the temporal evolution of photospheric spots over a timescale of a few weeks. Since only some phases of the primary eclipse but not the secondary were covered, this second half of the data was rejected. Thus, four light curves in *BVRI* bands spanning 22 days of observations and with 438, 495, 443 and 455 points, respectively, were finally used.

Additional photometry in the Strömgren *uvby* system was published by Morale et al. (1996) and *Tycho-2* (Høg et al. 2000) light curves are also available. Interestingly, the photometry of these data sets is calibrated to the standard systems, so despite the poor phase coverage renders them useless to determine the orbital and physical parameters of the system, they were used to compute the magnitudes in the Strömgren and *Tycho-2* photometric systems. These magnitudes were later useful

to derive accurate individual temperatures.

Regarding radial velocity curves, spectroscopic time-series of IM Vir was conducted at the Harvard-Smithsonian Center for Astrophysics (CfA) from January 1984 to May 2009. Observations were obtained at the F.L. Whipple observatory (Arizona, USA) and at the Oak Ridge Observatory (Massachusetts, USA) with a similar echelle spectrograph and different telescopes. See Appendix B for more details on these observations. Spectra centered at the Mg I triplet at 5188.5 Å with a width of 45 Å were obtained.

The radial velocities of both stars were derived using TODCOR (Zucker & Mazeh 1994) with synthetic templates based on the ATLAS stellar atmosphere models (Castelli & Kurucz 2004). To check the self-consistency of the light and radial velocity curve fits, properties of the atmosphere models that best match the primary component were also provided: $T_{\text{eff}} = 5570 \pm 100$ K and $v \sin i = 43 \pm 2$ km s⁻¹. A rough value for the metallicity $[M/H] = -0.1$ was also estimated although its uncertainty may be as large as 0.25 dex. The secondary template is less constrained by observations and was chosen to match the results of the light curve analysis. TODCOR also provided a luminosity ratio of 0.06 ± 0.01 at the mean wavelength of the observations.

Due to the narrow spectral window and the use of synthetic spectra, some systematics on the radial velocities could be present due to the shift of the spectral lines in and out of the spectrum limits. This effect was corrected by simulating the spectrum of IM Vir with theoretical templates at the different phases observed, and then applying TODCOR to derive the radial velocities in the same way as done for the real observations. The differences between the input velocities and those recovered from the simulations were applied to the radial velocities. These differences were typically below 0.5 km s⁻¹ for the primary, but reach up to 13 km s⁻¹ for the secondary. The impact on the masses derived was very small: 0.26% and 0.14% for primary and secondary components, respectively. These corrections were applied to obtain the final radial velocity curves.

2.3.2 Analysis of light and radial velocity curves

As in the case of CM Dra, the light curves of IM Vir show a modulation on the out-of-eclipse phases: a signature of the presence of spots on the surface of one or both of the components. As a consequence, radial velocity and light curves cannot be simultaneously analyzed since these data span different time intervals in which the configuration of spots may have changed. In this case, however, the orbit is circular ($e = 0$), and therefore, there are no parameters dependent both on light and radial

velocity curves, except for some minor effects such as reflection or tidal deformations.

The radial velocity curves span 25 years of observations, so they provided a period much better than the light curves that only span 22 days. The ephemeris derived from radial velocity data for the primary eclipse were:

$$T_1 = 2,452,402.87420(52) + 1.30861497(34)E, \quad (2.10)$$

A preliminary individual Keplerian fit to the radial velocity curves of the primary and the secondary orbit revealed that the systemic radial velocity (γ) derived for the primary component was about 4 km s^{-1} lower than that derived for the secondary component. This same systematic effect has been already observed in other systems when there is a slight mismatch between the spectra of the system and the templates used to derive the radial velocities (Popper 2000; Griffin et al. 2000). In the case of IM Vir, the mismatch is likely coming from the cooler secondary component since theoretical templates start to become unrealistic for very cool stars. Experiments using other templates for both the primary and the secondary components did not resolve this bias and thus the radial velocity curves were fitted allowing for different systemic velocities. This procedure did not significantly affect the semi-amplitudes of the radial velocities, and therefore the semi-major axis or the mass ratio.

The parameters of the best Keplerian fits found for IM Vir are reported in Table 2.7 and the curves are shown in Figure 2.8. No indication of a significant eccentricity was found. The systemic radial velocity derived from the primary component is given since the template mismatch is expected to be smaller than for the secondary component. The systematic difference $\Delta\gamma$ with the value derived from the secondary is also given.

The photometric light curves were phase folded according to the ephemeris derived from the spectroscopic analysis and the WD code was used to solve for the inclination (i), the secondary effective temperature ($T_{\text{eff}2}$), the pseudo-potentials of each component (Ω_j) and the luminosity ratio at each bandpass (L_2/L_1). A phase shift was also set as a free parameter to account for possible distortions of the times of eclipse due to spots. The primary effective temperature was held fixed at 5570 K, as found from the spectral analysis, in order to update the limb darkening coefficients according to the temperature corrections during the iterations, exactly as in the case of the CM Dra analysis. The reflection albedos were fixed to 0.5, as appropriate for stars with a convective envelope, and the gravity darkening coefficients were set to 0.34 for the primary and 0.40 for the secondary following Claret (2000b).

Spot parameters were also fitted to reproduce the modulations on the out-of-eclipse phases. As for the case of CM Dra, the temperature factor of spots (T_s/T_{eff})

Table 2.7: Orbital parameters of the fits to the radial velocity curves of IM Vir.

Parameter	Value
Adjusted quantities	
P (days)	$1.30861497 \pm 0.00000034$
T_1 (HJD-2,400,000) ^a	52402.87420 ± 0.00052
K_1 (km s ⁻¹)	92.684 ± 0.088
K_2 (km s ⁻¹)	136.84 ± 0.74
γ (km s ⁻¹)	$+12.221 \pm 0.082$
$\Delta\gamma$ (km s ⁻¹) ^b	-3.96 ± 0.69
Derived quantities	
$M_1 \sin^3 i$ (M_\odot)	0.978 ± 0.012
$M_2 \sin^3 i$ (M_\odot)	0.6621 ± 0.0044
$q \equiv M_2/M_1$	0.6773 ± 0.0037
$a_1 \sin i$ (10^6 km s ⁻¹)	1.6678 ± 0.0016
$a_2 \sin i$ (10^6 km s ⁻¹)	2.462 ± 0.013
$a \sin i$ (R_\odot)	5.934 ± 0.019
Other quantities pertaining to the fit	
σ_1 (km s ⁻¹)	0.99
σ_2 (km s ⁻¹)	8.39
N_{obs}	138

^aTime of primary eclipse.^bZero-point difference between the primary and secondary velocities, in the sense primary *minus* secondary.

and the co-latitude (θ_s) were found to be highly correlated with the size of spots. Thus, only the longitude (ϕ_s) and the size (r_s) of the spots were fitted while the longitude and the temperature factor were fixed to different values. The orbit of IM Vir is assumed to be circular and the time of computation of the WD code is much shorter than in the case of CM Dra. Consequently, a wide range of co-latitudes (from 10° to 170° , in steps of 10°) and spot temperature values (from 0.85 to 0.95 for the primary and from 0.75 to 0.85 for the secondary with a step size of 0.05) were explored. We considered spots on the primary, the secondary, and on both components. The overall best fit has one spot on each component but with a χ^2 value that is only marginally better than for the other two scenarios (1.5% lower than in the case with two spots on the primary, and 3.4% lower than in the case of two spots on the secondary). The parameters of the best fit are given in Table 2.8 and the light curves are shown in Figures 2.9 and 2.10. Figure 2.11 depicts the location of the spots in the model with the lowest residuals at different orbital phases and Figure 2.12 illustrates the effect of such spots on the light curves, that range from ~ 0.025 mag in B to ~ 0.015 mag in I (peak to peak).

The uncertainties reported in this table are conservative estimates computed as the quadratic addition of the following sources of error:

- The internal statistical errors of the best fit reported by WD (σ_{WD}). As a check, the adopted solution was iterated again 200 times to examine the scatter of the parameters of those 200 fits. For all parameters the scatter of those solutions

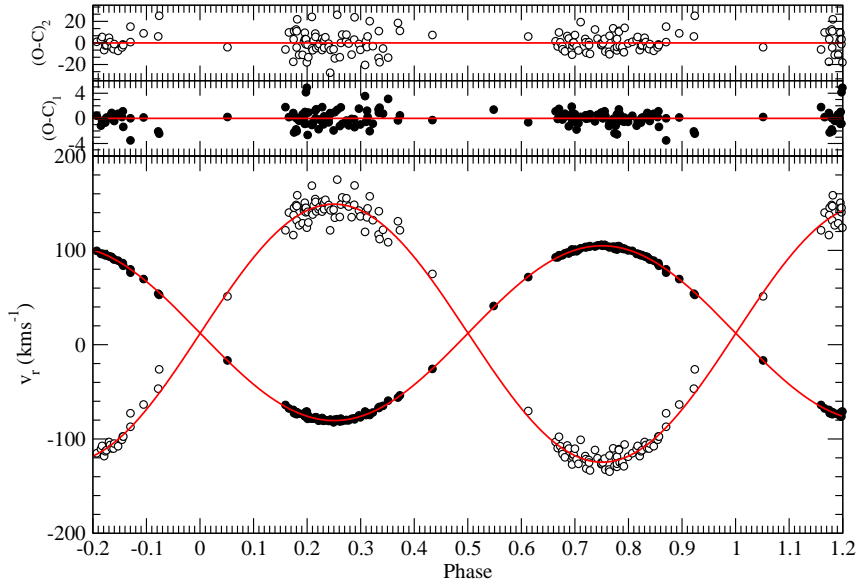


Figure 2.8: Best fits to the radial velocity curves of the primary component (filled symbols) and the secondary component (open symbols) of IM Vir. The upper panels show the residuals of these fits. Notice the different scales of these panels.

was found to be smaller than the errors given by the WD code, except for the light ratios that are a factor of 2 larger. The larger of the two estimates were adopted as the uncertainties.

- The contribution of the analysis in different bands (σ_{Bands}). Fits to the individual *BVRI* light curves were performed by fixing the spot properties. The dispersion of each parameter above the average of the four fits was taken as an additional contribution to the overall uncertainty.
- The error coming from the indetermination of the correct spot scenario (σ_{Spots}). This contribution was estimated comparing the parameters of the best fits with the spots on the primary, on the secondary or on both. Half of the range of each parameter on these three solutions was adopted as uncertainty.

Table 2.9 summarizes the values of these uncertainties and gives their combination for the relevant parameters of light curves.

Solutions with the eccentricity set as a free parameter were performed but with no significant results. Third light was also tested, but unphysical negative values or values consistent with zero were found. Different limb darkening laws were also

Table 2.8: Light curve parameters of IM Vir from the simultaneous best fit.

Parameter	Primary	Secondary
Geometric properties		
Phase shift	0.0006 ± 0.0001	
i (deg)	87.24 ± 0.16	
Ω	6.298 ± 0.023	7.081 ± 0.038
r^a	0.1785 ± 0.0008	0.1146 ± 0.0010
Radiative properties		
T_{eff} (K)	5570 ^b	4246 ± 16
L_2/L_1 B band	0.04805 ± 0.00008	
L_2/L_1 V band	0.07499 ± 0.00016	
L_2/L_1 R band	0.10960 ± 0.00027	
L_2/L_1 I band	0.14267 ± 0.00036	
Albedo ^c	0.5	
Gravity darkening ^c	0.34	0.40
Limb darkening coefficients (square root law)		
x B band	0.625	0.904
y B band	0.240	-0.057
x V band	0.364	0.644
y V band	0.450	0.190
x R band	0.237	0.462
y R band	0.517	0.354
x I band	0.137	0.269
y I band	0.539	0.475
Spots properties		
Latitude ^c (deg)	-60	-60
Longitude (deg)	307.3 ± 4.9	331.8 ± 4.7
Radius (deg)	26.4 ± 1.2	36.0 ± 2.5
T_{eff} factor ^c	0.95	0.80
Residuals and number of observations		
σ_B / N_B	0.01347 / 438	
σ_V / N_V	0.01295 / 495	
σ_R / N_R	0.01300 / 443	
σ_I / N_I	0.01399 / 455	

^aVolume radius derived from the fitted parameters.^bFixed according to the spectroscopic analysis.^cFixed; see text.

tested but results were within the errors.

The B and V light ratios were interpolated to the wavelength of the spectroscopic observations yielding $L_2/L_1 = 0.066 \pm 0.005$, which agrees well with the spectroscopic determination ($L_2/L_1 = 0.06 \pm 0.01$).

Finally, the effect of the photospheric spots was tested like in the case of CM Dra. The differentials between radial velocity curves computed with the three best fitted spot scenarios and the canonical solution were applied to the radial velocity curves. Figure 2.13 shows these differentials, which are always below or similar to 1 km s^{-1} .

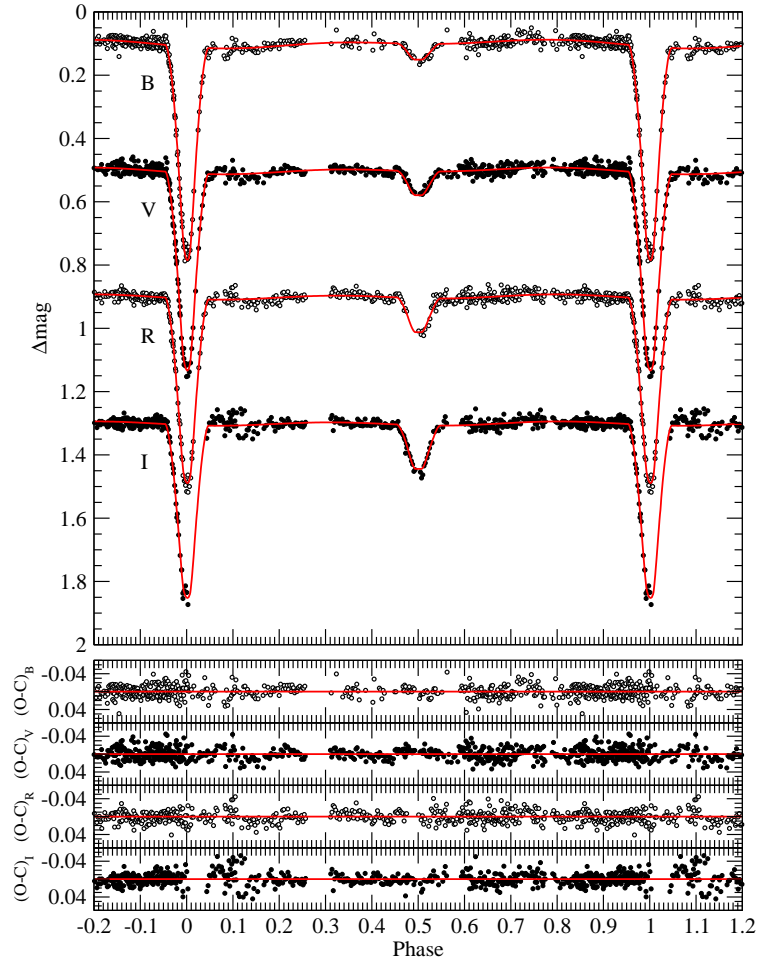


Figure 2.9: Light curves of IM Vir with their best simultaneous fit. The lower panels show the residuals in the same order as arranged in the top panel.

Then, Keplerian fits were performed to these new data sets. Differences below 0.6% and 0.2% were found for the minimum masses of the components and the projected semimajor axis, respectively. To be conservative, half of these ranges were added to the uncertainties of the radial velocity parameters.

2.3.3 Absolute properties

The individual masses and radii of the components of IM Vir derived from the fits to the light and radial velocity curves are given in Table 2.10. As explained, the uncer-

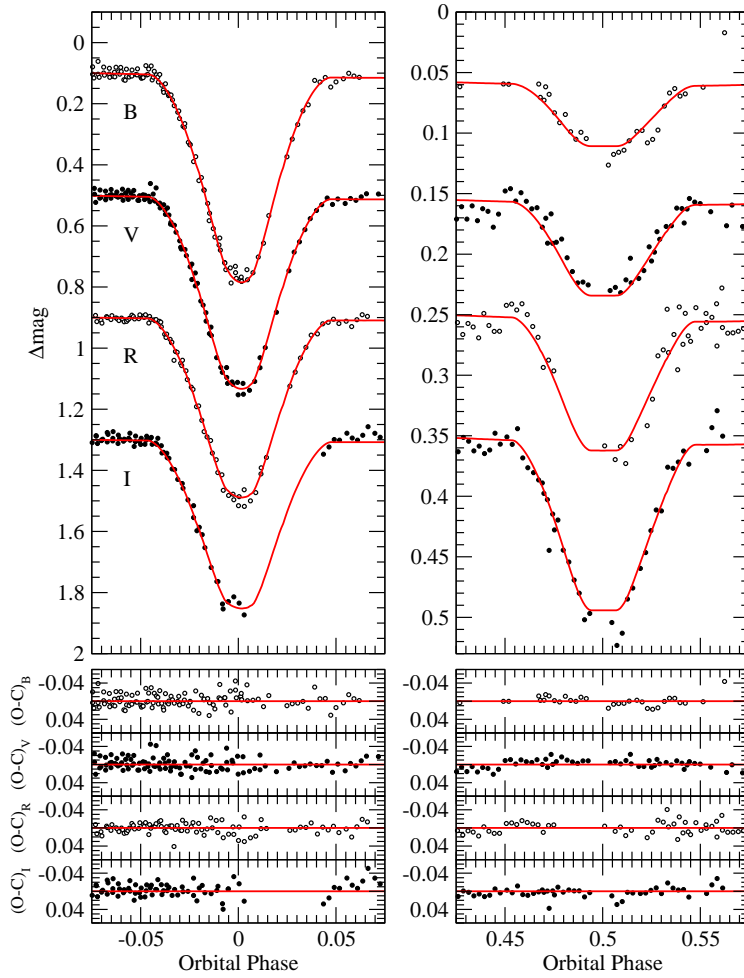


Figure 2.10: Enlargement of the eclipse phases of Figure 2.9. Note the different scale of the secondary eclipse differential magnitudes.

tainties reported are conservative estimates considering the different data sets, the effect of photospheric spots and the fits statistical errors. With the accurate radii and the period, synchronous rotation velocities of $41.0 \pm 0.6 \text{ km s}^{-1}$ and $26.3 \pm 0.5 \text{ km s}^{-1}$ were derived for the primary and the secondary components of IM Vir, respectively. The value for the primary is in good accordance with the spectroscopic determination of $43 \pm 2 \text{ km s}^{-1}$, suggesting that synchronization with the orbital motion has been achieved. Independent determinations of $42 \pm 2 \text{ km s}^{-1}$ and $31 \pm 4 \text{ km s}^{-1}$ were obtained by Fekel (2009, private communication) from the spectroscopic data used in Strassmeier et al. (1993). These values also agree very well with the primary

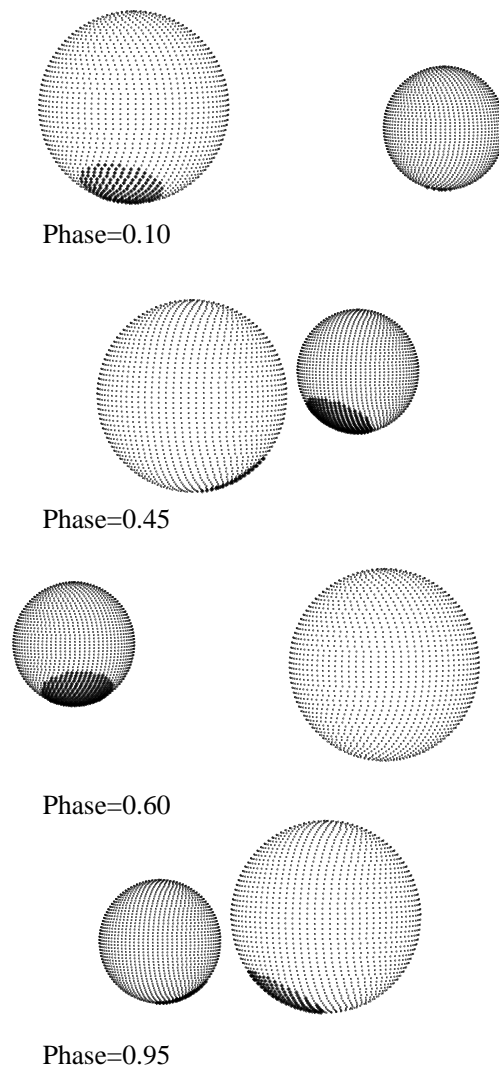


Figure 2.11: Spot location on each star as viewed from the Earth at different orbital phases, in the adopted scenario in which each component has one cool spot. The stars and their separation are rendered to scale.

component and probably also with the secondary, confirming the synchronization of the system.

As a self consistency check, the luminosity ratio derived from spectroscopy was compared with those obtained from the light curve fits. The B and V light ratios were interpolated to the mean wavelength of the spectroscopic observations yielding

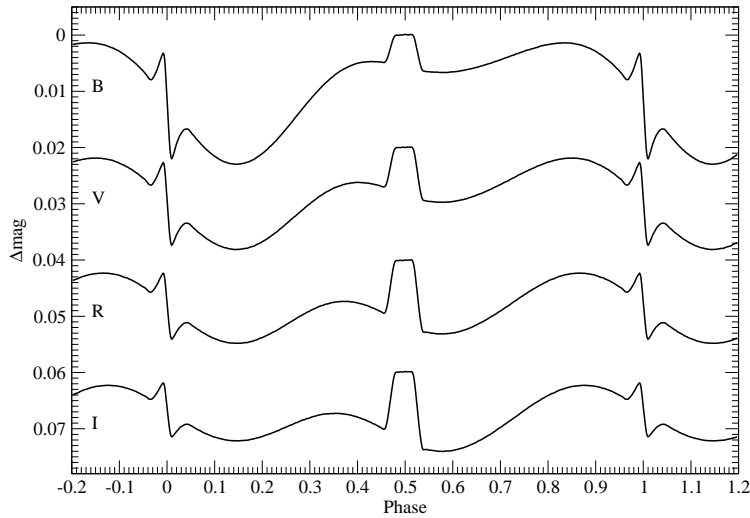


Figure 2.12: Effect of the spots on the light curves of IM Vir. The variations shown correspond to the adopted scenario with one cool spot on each star.

$L_2/L_1 = 0.066 \pm 0.005$, which agrees well with the value of 0.06 ± 0.01 that is determined from the spectra.

In order to estimate the individual temperatures of the components of IM Vir, a T_{eff} for the primary must be assumed. For the light curve analysis, a rough estimate from spectroscopy of 5570 K was used, but this value can be refined using the magnitudes and light ratios of IM Vir once known from the light curves. Unlike in the case of CM Dra, there is no trigonometric determination of the parallax of IM Vir, so the temperature has to be derived from temperature-color calibrations. In order to proceed, the *Tycho-2* visual magnitudes $B_T = 10.483 \pm 0.039$ mag and $V_T = 9.768 \pm 0.030$ mag (Høg et al. 2000) and the IR magnitudes from 2MASS catalog (Cutri et al. 2003) were compiled. The data of 2MASS indicated that observations were taken at orbital phase ~ 0.54 , during the egress of the secondary eclipse, so JHK_s magnitudes were corrected according to the results of the IM Vir light curves extrapolated to the 2MASS bands. The corrections to be applied on these magnitudes were about 0.03 mag for the three bands yielding $J = 8.176 \pm 0.020$ mag, $H = 7.712 \pm 0.025$ mag and $K_s = 7.634 \pm 0.024$ mag. Strömgren magnitudes were also derived from Manfroid et al. (1991) and Morale et al. (1996) giving $b = 10.209 \pm 0.021$ mag and $y = 9.748 \pm 0.017$ mag. The out-of-eclipse BV measurements of the light curves analyzed here, after transformation of these curves to a standard system using the comparison and check stars, were also used to obtain $B = 10.234 \pm 0.030$ and $V = 9.574 \pm 0.030$ Johnson magnitudes.

Table 2.9: Summary of the estimation of uncertainties for the light curve parameters of IM Vir.

Parameter	Individual light-curve fits				Standard error estimates		
	<i>B</i>	<i>V</i>	<i>R</i>	<i>I</i>	σ_{Bands}	σ_{Spots}	σ_{WD}
Phase shift	0.0007	0.0007	0.0006	0.0004	0.00014	0.00010	0.00010
<i>i</i> (°)	87.38	87.22	86.91	87.83	0.38	0.08	0.16
$T_{\text{eff},2}$	4272	4191	4231	4304	49	56	16
Ω_1	6.257	6.289	6.304	6.431	0.077	0.018	0.023
Ω_2	7.091	7.080	7.003	7.220	0.090	0.044	0.038
$r_{\text{vol},1}$	0.1798	0.1788	0.1783	0.1743	0.0024	0.0006	0.0008
$r_{\text{vol},2}$	0.1144	0.1146	0.1161	0.1119	0.0017	0.0009	0.0010
L_2/L_1 (<i>B</i>)	0.04999	–	–	–	–	0.0041	0.00021
L_2/L_1 (<i>V</i>)	–	0.05366	–	–	–	0.0054	0.00030
L_2/L_1 (<i>R</i>)	–	–	0.10928	–	–	0.0065	0.00042
L_2/L_1 (<i>I</i>)	–	–	–	0.15179	–	0.0068	0.00050

Parameter	Adopted fit	
	Value	σ
Phase shift	0.0006	0.0002
<i>i</i> (°)	87.24	0.42
$T_{\text{eff},2}$	4246	83
Ω_1	6.298	0.082
Ω_2	7.08	0.11
$r_{\text{vol},1}$	0.1785	0.0026
$r_{\text{vol},2}$	0.1146	0.0022
L_2/L_1 (<i>B</i>)	0.0480	0.0041
L_2/L_1 (<i>V</i>)	0.0750	0.0054
L_2/L_1 (<i>R</i>)	0.1096	0.0065
L_2/L_1 (<i>I</i>)	0.1427	0.0068

Prior to deriving the individual temperatures from these magnitudes and colors, the individual primary and secondary magnitudes must be determined. This deconvolution is done according to the equations:

$$m_1 - m = 2.5 \log \left(1 + \frac{L_2}{L_1} \right), \quad (2.11)$$

$$m_2 - m = 2.5 \log \left(1 + \frac{L_1}{L_2} \right), \quad (2.12)$$

where m is the total magnitude of the binary system and m_j the magnitude of each component. Light ratios in the *B* and *V* bands were computed from the light curve solutions. For Strömgren *uvby*, these were derived from fits to the light curves of Manfroid et al. (1991) with all the parameters fixed except for the light ratio. Finally, *Tycho-2* and 2MASS light ratios were derived from 1 Gyr theoretical isochrones of Girardi et al. (2000) and Baraffe et al. (1998), respectively. 5 Gyr isochrones were also tested but differences were within the errors. The colors derived for the components of IM Vir are listed in Table 2.11.

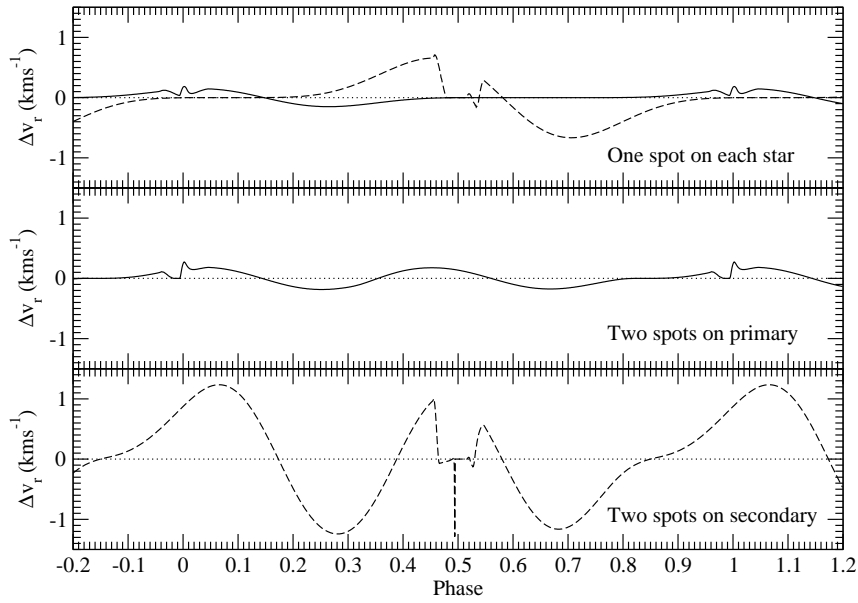


Figure 2.13: Effect of the spots on the radial velocity curves of IM Vir. The three spot scenarios that give the best residuals are tested as labeled. Solid and dashed lines are the differentials in the radial velocities due to spots for the primary and the secondary components, respectively.

Table 2.10: Absolute physical properties of the components of IM Vir.

Parameter	Primary	Secondary
M (M_{\odot})	0.981 ± 0.012	0.6644 ± 0.0048
R (R_{\odot})	1.060 ± 0.016	0.681 ± 0.013
T_{eff} (K)	5570 ± 100	4250 ± 130
$\log g$ (cgs)	4.379 ± 0.014	4.595 ± 0.017
$\log L/L_{\odot}$	-0.012 ± 0.034	-0.867 ± 0.056
$[M/H]$	~ -0.3	
distance (pc)	89.8 ± 5.8	

Color-temperature calibrations from Ramírez & Meléndez (2005), Casagrande et al. (2006) and González Hernández & Bonifacio (2009) were applied to derive the individual temperature of the primary component from its colors assuming solar metallicity. All the colors given in Table 2.11 were used to check the consistency between calibrations although not all of them are independent. These calibrations yielded an average value of $T_{\text{eff}1} = 5560 \pm 100$ K that is in very good agreement with the value found from spectroscopy $T_{\text{eff}1} = 5570 \pm 100$ K. According to the

Table 2.11: Combined out-of-eclipse magnitudes and colors of IM Vir

Color	Combined	Primary	Secondary
$B - V$	0.661 ± 0.028	0.632 ± 0.030	1.12 ± 0.12
$b - y$	0.465 ± 0.032	0.440 ± 0.024	0.71 ± 0.15
$V - J$	1.372 ± 0.028	1.261 ± 0.030	2.41 ± 0.12
$V - H$	1.832 ± 0.030	1.656 ± 0.030	3.15 ± 0.12
$V - K_s$	1.905 ± 0.031	1.712 ± 0.030	3.29 ± 0.12
$B_T - V_T$	0.715 ± 0.057	0.685 ± 0.039	1.16 ± 0.16
$V_T - K_s$	2.099 ± 0.038	1.914 ± 0.031	3.38 ± 0.15
$J - K_s$	0.533 ± 0.031	0.451 ± 0.035	0.88 ± 0.13

temperature ratio from the light curves, $T_{\text{eff}2} = 4250 \pm 130$ K. Casagrande et al. (2008) color-temperature calibrations for cool stars were used to check this result. These relations give $T_{\text{eff}2} = 4380 \pm 220$ K, a value still consistent with the much more accurate determination from the temperature ratio coming from the light curves.

Once temperatures are known, the total bolometric luminosities can be derived and, thus, the distance to the system when comparing with the apparent magnitudes. The empirical bolometric corrections from Flower (1996) were used to derive an absolute M_V magnitude of 4.98 ± 0.10 mag for the system. Comparing with the apparent magnitude $V = 9.574 \pm 0.030$ mag, the distance derived is 89.8 ± 5.8 pc, ignoring extinction. This value is 50% larger than the rough estimate computed from the spectral type by Strassmeier et al. (1993).

Like in the case of CM Dra, the chemical composition of IM Vir is also unconstrained. Beyond the spectroscopic estimate of $[M/H] = -0.1 \pm 0.25$ given here, another spectroscopic value of -0.53 ± 0.16 was reported by Dall et al. (2007) although based on a composite spectrum and a model with an effective temperature ~ 200 K cooler and a higher surface gravity. A rather poorly determined value of -0.37 ± 0.47 dex was derived from the Strömgren photometric colors of the primary and the empirical calibrations of Holmberg et al. (2007). The secondary is too cool for this calibration but within the range of the near-IR calibrations of Bonfils et al. (2005) that yielded $[Fe/H] = -0.26 \pm 0.26$. However, it has been noticed that this calibration underestimates the metallicity of late-type stars by about 0.3 dex (Johnson & Apps 2009). These results may suggest a subsolar metallicity of about -0.3 for IM Vir, but confirmation is required.

Remarkably, the orbital and physical properties of IM Vir predict a total secondary eclipse with a duration of about 28 minutes during which the secondary star is completely occulted. This offers a unique opportunity to obtain a reliable estimation of the chemical composition of the system by analyzing a spectral distribution

of the primary component undisturbed by the secondary spectral features. This may be exploited in the future.

Regarding the age of IM Vir, little is known. UVW space velocities of $U = +24.4 \text{ km s}^{-1}$ (positive toward the Galactic center), $V = -17.7 \text{ km s}^{-1}$ and $W = -3.0 \text{ km s}^{-1}$ were determined from the *Tycho-2* proper motions and the systemic velocity derived from light curves, but these velocities do not appear to associate IM Vir with any known moving group in the solar neighborhood. Therefore the age of this system is undetermined.

Chapter 3

The effect of activity on stars

As explained in the first chapter of this work, stellar structure and evolution models must be confronted with observations in order to check the validity of their predictions. Apart from the Sun, which is commonly used to calibrate the mixing length parameter of the convective transport, DDLEBs offer a unique opportunity to test models predictions since masses, radii and effective temperatures of their components can be determined with very good accuracy (well below the 3% level in the case of masses and radii), as has been shown for CM Dra and IM Vir. Besides, the masses and radii are fundamentally determined independently of any calibration or distance estimation. As explained in Chapter 1, DDLEBs have unveiled significant discrepancies between the observed radii and the effective temperatures of the stars in these systems and model predictions, being observed radii $\sim 12\%$ larger and effective temperatures $\sim 4\%$ cooler. On the other hand, luminosities are roughly well reproduced. Magnetic activity was one of the phenomena considered to be responsible of these discrepancies (Torres & Ribas 2002; Ribas 2006b; Torres et al. 2006; López-Morales 2007), however, the sample of very well-known eclipsing binaries was still scarce at that time and further confirmation was required.

The accuracies reached in the masses and radii of the components of CM Dra and IM Vir make these two systems very valuable to test stellar models. This chapter shows the comparison between the stellar models of the Lyon group (Baraffe et al. 1998), developed for the case of low-mass stars, and the components of CM Dra and IM Vir. They are put in context with the DDLEBs with best mass and radius determinations and with similar discrepancies found between active and inactive single isolated stars (Morales et al. 2008a). The results reinforce the hypothesis that magnetic activity could be responsible for the discrepancies between models and observations that will be tested on models in the following chapter.

3.1 Comparison between models and observations

In order to thoroughly test stellar structure and evolutionary models, accurate fundamental properties of the stars must be known. Masses and radii with uncertainties below the 3% limit allow to test the effect of different chemical composition, convection theories or opacity tables on the structure of the stars (Andersen 1991; Torres et al. 2010). The light and radial velocity curve analyses of DDLEBs provide the individual masses, radii and effective temperatures (given the temperature of one of the components) of their components with high accuracy.

When the metallicity and the age of the system are also reliably known from other sources of data, then all the relevant model parameters are constrained and the mass-radius ($M-R$), mass-effective temperature ($M-T_{\text{eff}}$) and mass-luminosity ($M-L$) relationships can be compared with any free parameter in the models. Any persistent discrepancy between models and observations would be indicative of a missing ingredient in the models.

In the worst case, age and metallicity are poorly determined and they enter as free parameters in the comparison. However, some estimation of these quantities can be obtained if one assumes that the components of the binary are coeval, so they formed from the same molecular cloud and have the same age and chemical composition. In this case, the metallicity and the age can be used as free parameters that must fit the $M-R$, $M-T_{\text{eff}}$ and $M-L$ relationships of both components at the same time. If one of these relationships is not properly fitted simultaneously for both components of the binary, again, this would indicate a shortcoming of the models. This model adjusting procedure is particularly useful for binaries with components with very different masses, such as the case of IM Vir, because the slopes of the $M-R$, $M-T_{\text{eff}}$ and $M-L$ relationships, that depend both on the age and the chemical composition, are better constrained by the observations.

As already mentioned in the Section 1.3 of the introductory chapter of this work, the comparison between models and observations do indeed show significant radius and temperature discrepancies, while luminosities are correctly described by models (Torres & Ribas 2002; Ribas 2006b). Different explanations have been proposed to reconcile models with the observations of low-mass stars.

- **Activity:** Using the available data from DDLEBs and analysing the possible scenarios, Ribas (2006b) and Torres et al. (2006) concluded that a plausible explanation for the observed discrepancies could be related to stellar activity. The active components of eclipsing binaries appear to be larger and cooler than inactive single stars (which are correctly described by models) while keeping similar luminosities. To first approximation, this means that, regardless of

changes in the stellar outer layers, the rate of nuclear burning in the core is not modified by activity and therefore the overall flux is conserved. This could be explained by the effect of the photospheric spots in the components of these systems. These spots may block part of the outgoing flux from the stellar interior, which is conserved by increasing the radius of the star.

- **Metallicity:** According to stellar models, the radius and the effective temperature of a star depend on its metallicity. Berger et al. (2006) found a correlation between the radius discrepancy and the metallicity for a sample of single stars with radius measured interferometrically, thus proposing this property as the responsible of this discrepancy. However, in a recent work, Demory et al. (2009) did not confirm these results and found that single stars are well described by models by comparing interferometric radius measurements of inactive low-mass stars with model predictions. The Lyon stellar models predict radii and effective temperatures differences of about 4% and 20%, respectively, when comparing $[M/H] = 0.0$ and $[M/H] = -1.0$. However, many of the binary systems in which discrepancies with models are reported do not have such low metallicities nor such high temperature differentials. Furthermore, radius corrections due to metallicity are lower than needed to reproduce the observations. All this suggests that the metallicity may not be the main responsible of the discrepancies between models and observations.
- **Opacity:** Missing opacities in the stellar models could produce also significant differences on the stellar properties, but rather on the predicted magnitudes in the different passbands than on the fundamental properties such as the radii or the effective temperatures (Chabrier & Baraffe 1997; Baraffe et al. 1998). Recently, the possibility of underestimated opacities has been raised in the context of the Standard Solar Model. An increase of opacities near the bottom of the convective zone has been shown to reconcile helioseismic data of the Sun with models using the new chemical composition (Bahcall et al. 2004, 2005). These results and others found in the literature invoking problems with the atmospheric opacities as a source of the discrepancies present in observed radii of DDLEBs compared with theoretical models led us to perform different tests to analyze the effect of atmospheric opacity on the resulting stellar radius. Using the standard Lyon group stellar evolutionary models (Baraffe et al. 1998), an overall massive increase by a factor of ~ 10 in the opacity affects the radius by just 4% (and even this difference is smaller below the fully convective boundary), as already shown by Chabrier & Baraffe (1997). To obtain a $\sim 10\%$ larger radius the opacities of eclipsing binaries would have to be increased to unrealistically high values. Thus, missing elemental opacities do not seem to be enough to explain the $\sim 5 - 10\%$ radius disagreement between models and

observations. Moreover, opacity effects should also be present on single stars, which are known to be well described by models, as recently confirmed by Demory et al. (2009).

The effect of activity on the stellar structure seems to be a reasonable explanation, but further insight both on models and observations should be done in order to understand the whole scenario.

3.2 The case of CM Dra

In the previous chapter, the fundamental properties of the CM Dra system were derived from the analysis of light and radial velocity curves, yielding masses and radii accurate down to the 0.5% and 0.75% level, respectively, and temperatures with uncertainties of about 2%. The age was found to be 4.1 ± 0.8 Gyr from the analysis of the common proper motion companion WD, and the metallicity is the only property that remains poorly constrained. For this binary system, an apsidal motion rate was also found. This quantity can provide an additional constraint to the models since it depends on the internal mass distribution of the star. However, its accuracy is very low to draw firm conclusions.

3.2.1 Fundamental properties

Figure 3.1 shows the $M - R$ and $M - T_{\text{eff}}$ relationships of CM Dra compared with the predictions of Baraffe et al. (1998) stellar models with different ages and metallicities. A mixing length parameter $\alpha = 1$ has been used in this figure as suggested by these authors in the case of low-mass stars. Similar discrepancies as those found for other low-mass systems are apparent. The radii of the primary and secondary components are larger than expected for 4.1 Gyr solar metallicity stars by 5.0% and 5.2%, respectively. Comparing with the reported radius uncertainties, these discrepancies are significant to the 6.3σ and 7.8σ levels. Regarding temperatures, the situation is not much better, the components being 6.4% (for the primary) and 5.9% (for the secondary) cooler than expected from models. These differences in temperature are significant to the 3.0σ and 2.8σ level. Interestingly, the deviations in the radii and the effective temperatures are significant offsets, while the slope of the models appear to be substantially correct.

The plots in Figure 3.1, also show that age effects on radii and effective temperatures are almost negligible for the age of CM Dra, while metallicity effects are more important. However, differences between models and observations are even larger if

a subsolar metallicity is considered for the system as suggested by Viti et al. (1997, 2002). Very high metallicities (in contrast with the observations) should have to be assumed in order to explain the radii and the effective temperatures of the components of CM Dra.

In the case of luminosities, Figure 3.2 shows that, for the case of CM Dra, the stellar models predict stars brighter than observed, by 3.0% and 2.5% for the primary component and the secondary, respectively. In order to match the luminosity of the components of CM Dra for its given age, the metallicity has to be increased up to $[M/H] \sim 0.4$. This seems to be an unreal value, so a metallicity near solar is the only compromise we can adopt for CM Dra. On the other hand, the $\log L$ of the components is about 0.05 dex below the zero age main sequence prediction, thus older or younger ages for the system do not correct the discrepancy. It should also be noticed that the comparison in this $M - L$, as well as in the $M - T_{\text{eff}}$ plane, depends on the effective temperature assumed for the primary component. This temperature should have to be increased by about 150 K and 200 K to explain the $M - L$ and $M - T_{\text{eff}}$ relationships, respectively. However, these values would be inconsistent with the independent determinations from the flux calibration in the K band and the color-temperature calibrations used in Section 2.2.5. The luminosity discrepancies of the 4.1 Gyr solar metallicity models are marginally in accordance with the observations within the uncertainties, about 1.7σ and 1.0σ for primary and secondary components, respectively, thus confirming that luminosities are relatively better described by models than the radii or the effective temperatures.

These results of CM Dra increase the number of stars in well-known eclipsing binaries with radii and effective temperatures larger and cooler, respectively, than the stellar model predictions and extend these differences to the very low-mass domain of fully convective stars. Like classical DDLEBs such as YY Gem (Torres & Ribas 2002), CU Cnc (Ribas 2003) or GU Boo (López-Morales & Ribas 2005), CM Dra is known to be a magnetically active system. Evidence of this activity are the photometric variability of the system due to photospheric spots, the observation of flares (Eggen & Sandage 1967; Lacy et al. 1976; Kozhevnikova et al. 2004; Nelson & Caton 2007) and the X-ray luminosity. From the X-ray count rate and hardness ratio of CM Dra from *ROSAT* an X-ray luminosity of $L_X = (2.98 \pm 0.37) 10^{28} \text{ erg s}^{-1}$ is derived for the system using the parallax of CM Dra (van Altena et al. 1995) and the energy conversion factor prescribed by Schmitt et al. (1995). Assuming an equal contribution from both components of the system, bolometric to X-ray luminosity ratios of $\log L_X/L_{\text{Bol}} = -3.15 \pm 0.07$ and -3.10 ± 0.07 are derived for the primary and secondary components, respectively. These are common values found on stars saturated by activity (Pizzolato et al. 2003), thus increasing the mounting evidence that the discrepancies between models and observations are due to the magnetic activity.

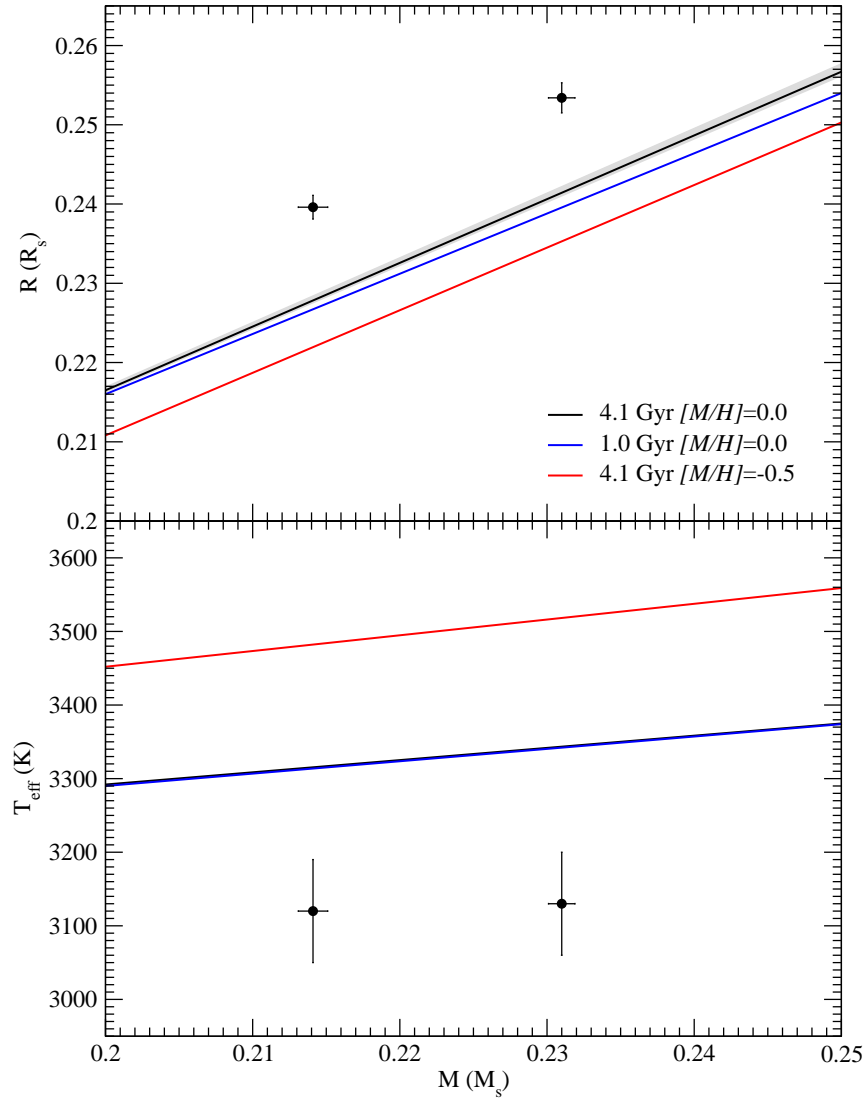


Figure 3.1: Theoretical $M - R$ (top) and $M - T_{\text{eff}}$ (bottom) relationships of Baraffe et al. (1998) models compared with the observed properties of the components of CM Dra. Models with different ages and metallicities are plotted as labeled. The age error is indicated by the shaded area in the $M - R$ plot.

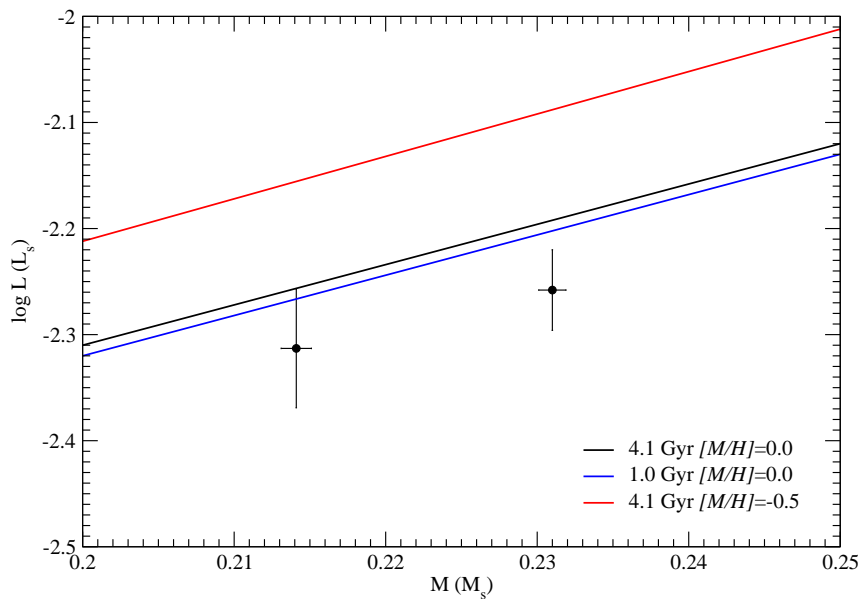


Figure 3.2: Theoretical $M - L$ relationship of Baraffe et al. (1998) models compared with the observed properties of the components of CM Dra. Models with different ages and metallicities are plotted as labeled.

CM Dra has often been regarded in the past to be a favorable system for inferring the primordial helium abundance of the Universe, assuming that it is a Population II star. Metcalfe et al. (1996) derived a rather large value of about 0.3 dex for the bulk helium abundance using polytropic stellar models following the description of Paczyński & Sienkiewicz (1984). Chabrier & Baraffe (1995) derived a much lower value of 0.25 dex by comparing with their models. The present work shows that models are not able yet to properly describe the fundamental properties of the components of CM Dra, so a comparison with models to derive the helium abundance is not meaningful.

3.2.2 Apsidal motion

The analysis of minima timings of CM Dra also provided the apsidal motion rate of the system, $\dot{\omega} = (2.3 \pm 1.4) \times 10^{-4} \text{ }^\circ\text{cycle}^{-1}$. Under the absence of external interactions, the advance of the line of apsides of the system is due to the relativistic effects and to the classical contribution of tidal forces and deformations by rotation. The classical precession induced by tidal effects is dependent on the density profile

of the stars in the binary. Following the prescriptions in Kopal (1978), the tidal apsidal motion is given by:

$$\dot{\omega}_{\text{tidal}} = 360^\circ (c_{2,1}k_{2,1} + c_{2,2}k_{2,2}), \quad (3.1)$$

where $c_{2,j}$ are coefficients that depend on the properties of each component and $k_{2,j}$ are the internal structure constants that depend on the mass profile of each star in the binary. These constants can be computed from theoretical models and thus the experimental value of the apsidal motion can add a further constraint on stellar models. Using the Baraffe et al. (1998) stellar models, values of $\log k_{2,1} = -0.95$ and $\log k_{2,2} = -0.96$ are found for the primary and secondary components of CM Dra. According to Kopal (1978), when the rotation axes of the components are perpendicular to the orbital plane of the system, the $c_{2,j}$ coefficients are given by:

$$c_{2,j} = \left[\left(\frac{\omega_{\text{rot},j}}{\omega_{\text{rot,K}}} \right)^2 \left(1 + \frac{M_{3-j}}{M_j} \right) \frac{1}{(1-e^2)^2} + 15 \frac{M_{3-j}}{M_j} \frac{8 + 12e^2 + e^4}{8(1-e^2)^5} \right] r_j^5, \quad (3.2)$$

where $\omega_{\text{rot},j}$ is the rotational angular velocity of each component, $\omega_{\text{rot,K}}$ is the Keplerian angular velocity (given by $2\pi/P$), M_j is the stellar mass of component j ($j = 1$ for the primary and $j = 2$ for the secondary), e is the eccentricity and r_j the radii of star j relative to the semimajor axis. As expected, the tidal contribution is inversely proportional to a high power of the separation between the components. In eccentric systems, when synchronization at the periastron passage between orbital and rotational velocity of the components is assumed (as expected for close eclipsing binary systems; Mazeh 2008), the ratio between the angular velocities is provided by:

$$\frac{\omega_{\text{rot},j}}{\omega_{\text{rot,K}}} = \sqrt{\frac{1+e}{(1-e)^3}}. \quad (3.3)$$

Given the orbital and physical properties found for CM Dra, and assuming synchronization, Equation 3.2 yields $c_{2,1} = (2.19 \pm 0.08) \times 10^{-5}$ and $c_{2,2} = (1.91 \pm 0.06) \times 10^{-5}$ and thus, the theoretical tidal contribution to the apsidal motion is $\dot{\omega}_{\text{tidal}} = (1.64 \pm 0.04) \times 10^{-3} \text{ }^\circ\text{cycle}^{-1}$.

The General Relativity theory predicts an apsidal motion rate that is given by Giménez (1985) as:

$$\dot{\omega}_{\text{rel}} = 5.45 \cdot 10^{-4} \frac{1}{1-e^2} \left(\frac{M_1 + M_2}{P} \right)^{\frac{2}{3}}, \quad (3.4)$$

where e is the eccentricity of the orbit, M_j the stellar masses given in units of the Sun, P the period in days, and $\dot{\omega}_{\text{rel}}$ is given in degrees per cycle. As the tidal case, this contribution increases for closer stars (shorter period). For the case of CM Dra,

given the properties derived in the previous chapter, the relativistic advance of the periastron is $\dot{\omega}_{\text{rel}} = (2.711 \pm 0.005) \times 10^{-4} \text{ }^\circ\text{cycle}^{-1}$. The tidal contribution is more than 6 times larger than the relativistic prediction.

Combining these two contributions, the theoretical value of the apsidal motion rate results in $\dot{\omega}_t = (1.91 \pm 0.04) \times 10^{-3} \text{ }^\circ\text{cycle}^{-1}$. This value is much larger than the observed $\dot{\omega} = (2.3 \pm 1.4) \times 10^{-4} \text{ }^\circ\text{cycle}^{-1}$ being the discrepancy significant at the 12σ level. Figure 2.7 clearly shows the different slopes of the $(O-C)$ vs. epoch relationships derived from observations and from theory. Internal structure constants should have to be decreased to unrealistically negative values to explain the observed apsidal motion. Thus, little can be said regarding the internal structure constants derived from models.

There are other factors that may contribute to the total apsidal motion rate of the system, such as the spin-orbit misalignment or the presence of third bodies in the system. The former may be discarded because CM Dra is sufficiently old to have been aligned and synchronized given the typical time scales of these processes (Mazeh 2008). This may be confirmed by the good agreement that was found between the rotational velocities and those derived from the physical properties of the stars assuming synchronization. Furthermore, the radial velocities of the components during the eclipse phases, in spite of the small number of points, do not show any significant Rossiter-McLaughlin effect due to spin-orbit misalignment.

The presence of a third body in the system could also explain the apsidal motion discrepancy. It may also be responsible for the small but significant eccentricity of this system, that should be circularized. There have been some claims of detections of low-mass companions orbiting CM Dra (Deeg et al. 2000, 2008) through the observation of the light time effect. However, the evidence so far does not seem compelling. The results of the analysis of the minima timings performed in Section 2.2.4 does not show any light time effect due to third bodies, unless it is indistinguishable from the ~ 15 s scatter of the minima timings or its period is over 60 yr. In Appendix A we discuss the third body scenario accounting for all observational data and constraints. Follow-up of the eclipse timings of CM Dra over the coming years, would provide a better determination of the apsidal motion rate and also unveil the presence of any third body in the system.

3.3 The case of IM Vir

The fundamental properties of the components of IM Vir derived from the analysis in Section 2.3, comprise the masses, the radii and the effective temperatures. There

is no constrain regarding age and metallicity. However, the leverage provided by the very different masses yields an estimate of these quantities by fitting the fundamental properties of both components of the system with a single isochrone simultaneously. Besides, the primary component of this system is a solar-type star that should be properly fitted by stellar models.

The widely-used Yonsei-Yale stellar models (Yi et al. 2001; Demarque et al. 2004) were first considered for the comparison with observations. These theoretical models range from $0.4 M_{\odot}$ up to $5 M_{\odot}$ with a mixing-length parameter $\alpha = 1.7432$ to reproduce the Sun. Stellar tracks for different compositions are provided to fit the observations by interpolation, but no combination of composition and age was able to match at the same time the primary and the secondary components of IM Vir in a Hertzsprung-Russell diagram (HR diagram). This could be, in part, due to the fact that, for the less massive secondary component (IM Vir B), these models may be less reliable than those of Baraffe et al. (1998). Figure 3.3 shows the fit of the Yonsei-Yale stellar models using only the primary component (IM Vir A). This fit yielded an age of about 8 Gyr and a metallicity of about +0.15 for the system. However, the secondary component is found to be too large and too cool according to this isochrone. This figure also shows different Baraffe et al. (1998) isochrones, which are better models for the less massive component of IM Vir. The effective temperature suggests a lower abundance, but the measured radius is too large regardless of the metallicity or the age.

The metallicity value of +0.15 dex is largely inconsistent with that derived from the spectral analysis and from the photometric calibrations in Section 2.3.3 that pointed at value near -0.30 dex. On the other hand, an old age model with super-solar abundance seems to be rather implausible. Besides, the inconsistency in age and metallicity between the models for the primary and for the secondary, may be an indication that the good fit achieved for the primary component is not real and that it too may have anomalies similar to those of the secondary. Both components are rapid rotators ($v \sin i = 41.0 \pm 0.6 \text{ km s}^{-1}$ and $26.3 \pm 0.5 \text{ km s}^{-1}$, for the primary and the secondary components, respectively) and therefore they could be both affected by magnetic activity. There is ample evidence of the activity of IM Vir, which was actually discovered through its X-ray emission. The light curves of this system also show the typical effect of photospheric spots, and the best fit was obtained by considering spots on both components. Additional manifestations of activity are detections of filled-in $H\alpha$ line (Strassmeier et al. 1993; Liu et al. 1996; Popper 1996), Ca II H and K emission (Dall et al. 2007) and flaring in X rays (Pandey & Singh 2008). With the X-ray count rate and the hardness ratio from *ROSAT* a total X-ray luminosity of $L_X = (1.48 \pm 0.29) 10^{30} \text{ erg s}^{-1}$ is derived for the system according to the prescriptions given in Schmitt et al. (1995) and the distance derived in Section 2.3.3. Assuming equal X-ray emission for each star, since

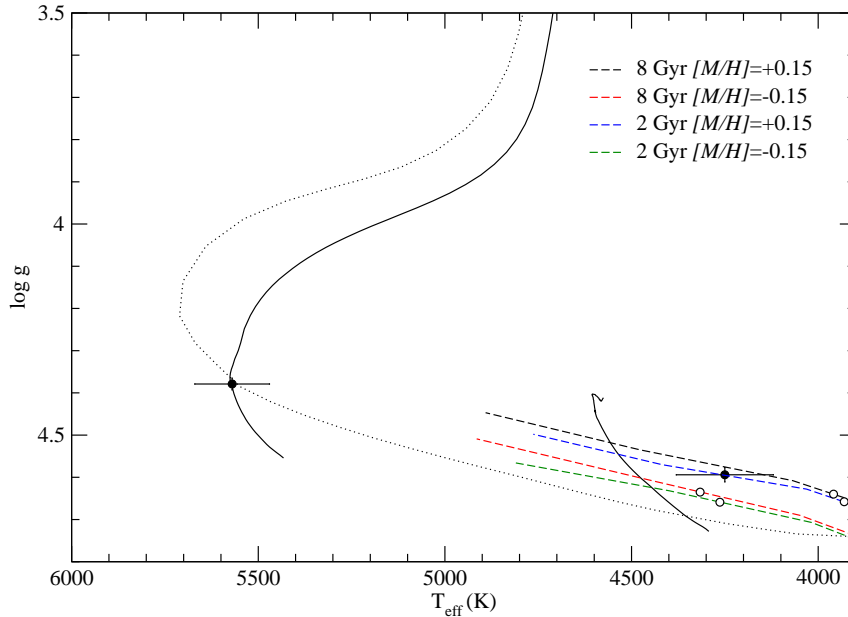


Figure 3.3: Fit of the Yonsei-Yale models for the primary component of IM Vir. Solid lines are the stellar tracks for the masses of IM Vir A and IM Vir B with $[Fe/H] = +0.15$. The dotted line is the 8 Gyr isochrone that best match the primary component. Different sets of Baraffe et al. (1998) isochrones are also plotted for the secondary component as labeled. Open symbols indicate the corresponding position of the mass of IM Vir B on these isochrones.

the *ROSAT* observation does not resolve the binary, the X-ray to bolometric luminosities ratios derived are $\log L_X/L_{\text{Bol}} = -3.70 \pm 0.13$ and -2.84 ± 0.13 for the primary and secondary components, respectively. These values are consistent with IM Vir B being completely saturated and IM Vir A being near saturation. They are similar to the X-ray luminosities seen in other active binary systems, and therefore, it could be assumed that both stars in this system may be affected by stellar activity.

Since radii and effective temperatures are not correctly reproduced by models, the $M - R$ and $M - T_{\text{eff}}$ relationships cannot be used to estimate the age and the metallicity of the system by fitting standard models. However, there is still a possibility to estimate these properties from models if only the $M - L$ relation is used, because it has been reported that the luminosities of these systems are indeed well described by models. As a way of parameterizing the missing physical effect from activity and their impact on the structure of low-mass stars, Torres (2007) explored the use of a correction factor β to the theoretical radii, and showed that good fits to empirical data could be achieved by simultaneously correcting the

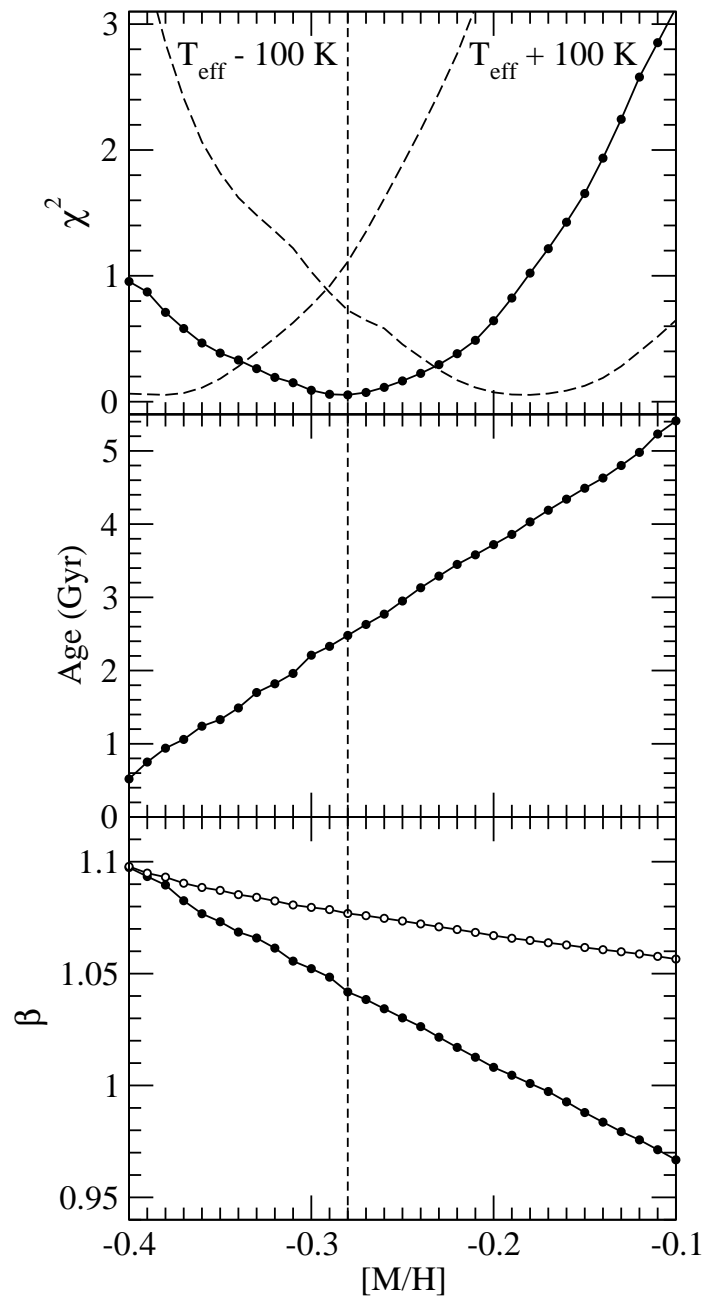


Figure 3.4: Illustration of the grid search to obtain the best simultaneous fit to the observed properties of the components of IM Vir using the Baraffe et al. (1998) models. For each metallicity of the grid search, the χ^2 of the fit, the age that best match the observations and the radius corrections factors β_1 (solid symbols) and β_2 (open symbols) are shown in top, middle and bottom panels, respectively. The vertical dotted line marks the best fit to the observations. Dashed lines in the top panel shows the χ^2 of the same fit when temperatures are increased or decreased by 100 K as labeled.

theoretical temperatures by $\beta^{-1/2}$, so as to preserve the bolometric luminosity. These same procedure was applied to the components of IM Vir considering different β parameters for the primary and secondary components, and defining the χ^2 of the fit as

$$\chi^2 = \sum_{j=1}^2 \left(\frac{R_j - \beta_j R_{\text{mod},j}}{\delta R_j} \right)^2 + \left(\frac{T_{\text{eff},j} - \beta_j^{-1/2} T_{\text{eff,mod},j}}{\delta T_{\text{eff},j}} \right)^2 + \left(\frac{L_j - L_{\text{mod},j}}{\delta L_j} \right)^2. \quad (3.5)$$

where, the subindex *mod* indicates the value derived from the models according to the mass of each component, and δR , δT_{eff} and δL are the uncertainties of the radii, the effective temperature and the luminosity, respectively. A wide range in metallicity and age using the Lyon stellar models (Baraffe et al. 1998) were explored to match simultaneously the luminosity of both components of IM Vir and to compute their correction factors β_1 and β_2 . Figure 3.4 illustrates the results of the grid search. For each metallicity, it displays the age and β_j factors that fit the observations with the lowest χ^2 as computed from Equation 3.5. The best fit was found for an age of 2.4 Gyr and $[M/H] = -0.28$. Interestingly, this value of metallicity is much more consistent with the rough estimates from photometry and spectroscopy than the metal-rich composition derived from Yonsei-Yale models for the primary. The radius correction factors are $\beta_1 = 1.037$ and $\beta_2 = 1.075$, meaning that stellar radii are 3.7% and 7.5% larger and the effective temperatures about 2% and 3.5% cooler than models predictions for the primary and the secondary components, respectively. Figures 3.5 and 3.6 show the $M - L$, $M - R$ and $M - T_{\text{eff}}$ relationships of the model that best fit the observations, as well as for models with different sets of age and metallicity for comparison.

Fits with temperatures increased and decreased by 100 K were also tested because the fitting procedure relies on the absolute temperatures, which are determined from the assumed temperature of the primary and the temperature ratio better determined from light curve analysis. Figure 3.4 also shows the χ^2 values of these fits. The best fit metallicity changes by about ± 0.10 dex and the age by about ± 0.50 Gyr, while correction factors vary about ± 0.010 for β_1 and ± 0.003 for β_2 , thus still showing similar discrepancies with the stellar models.

Therefore, the differences in radii and effective temperatures between the models and the components of IM Vir are of similar magnitude as those found for other active stars with convective envelopes. This is not an unexpected result for IM Vir B given the evidence from other low-mass DDLEBs. The result for IM Vir A supports the evidence that the discrepancies between models and observations are not confined to the low-mass stars, but reach solar-type stars as have been documented for other systems such as VZ Cep (Torres & Lacy 2009), CV Boo (Torres et al. 2008), FL Lyr (Popper et al. 1986) and V1061 Cyg (Torres et al. 2006).

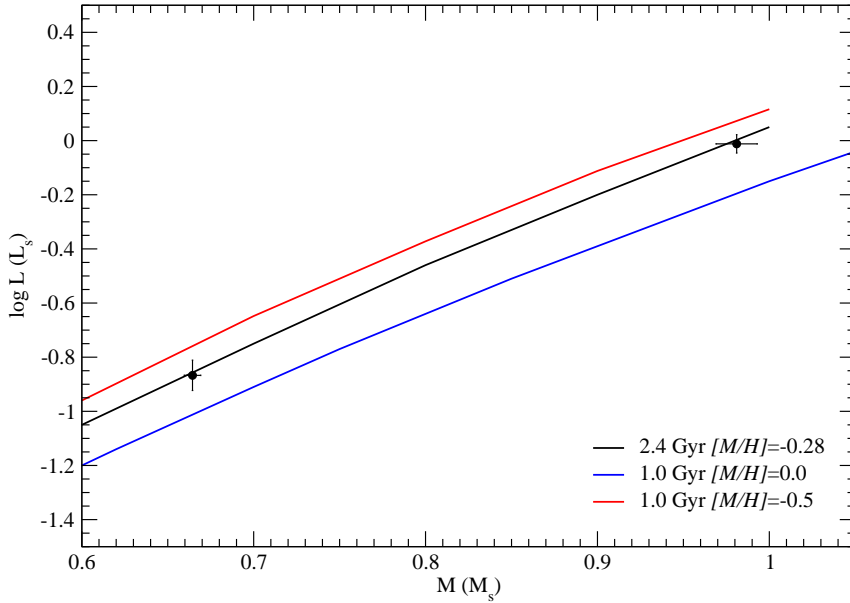


Figure 3.5: Theoretical $M - L$ relationship of the Baraffe et al. (1998) models compared with the observed properties of the components of IM Vir. The 2.4 Gyr isochrone with $[M/H] = -0.28$ that best fits the observations is shown along with other isochrones with a different set of age and metallicity.

3.4 Activity on single stars

The results of the comparison between models and observations of low-mass stars in DDLEBs lead to attribute the discrepancies in radii and effective temperatures to the magnetic activity (Torres & Ribas 2002; Ribas 2006b; this work). In these systems, where orbital synchronization forces the components to rotate fast, high levels of magnetic activity are triggered. With a much longer history, the question of the possible differences between active and inactive stars has been a recurrent one (Kuiper 1942; Joy & Abt 1974). Recent studies have been generally focused on the comparison of radiative properties such as spectral types or photometric colors. The conclusions have been quite diverse, both in favor (Hawley et al. 1996; Amado & Byrne 1997) and against (West et al. 2004; Bochanski et al. 2005) the existence of systematic color differences. One of the most conclusive analyses is that of Stauffer & Hartmann (1986), where the authors identified a separation of the sequences of active and inactive stars in a luminosity-color plot. The reasons for the observed separation in the sequences could not be unambiguously identified since it could come

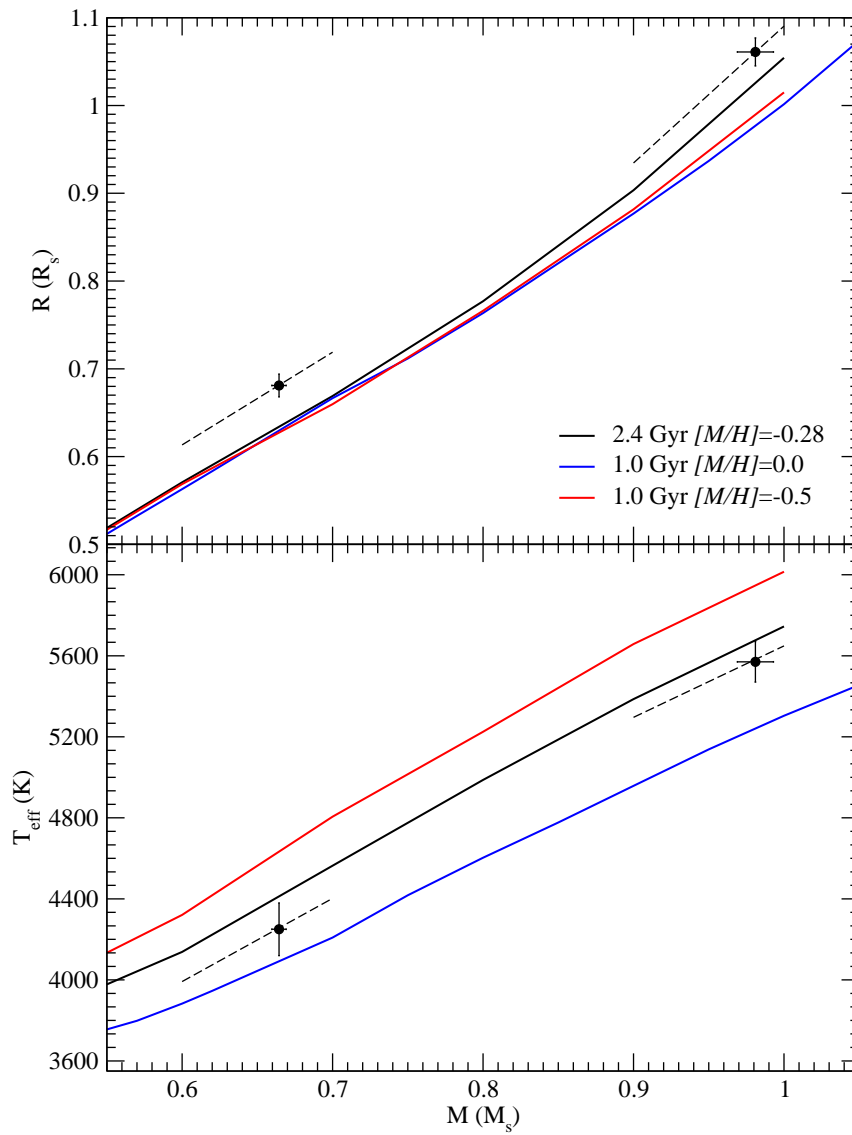


Figure 3.6: Theoretical $M - R$ (top) and $M - T_{\text{eff}}$ (bottom) relationships of the Baraffe et al. (1998) models compared with the observed properties of the components of IM Vir. The 2.4 Gyr isochrone with $[M/H] = -0.28$ best fitting the luminosities is plotted, as well as other isochrones with a different set of age and metallicity. Dashed lines correspond to the best fitted model but with radii and temperatures corrected according to the β_j correction factor of each star.

from luminosity differences at constant effective temperature, effective temperature differences at constant luminosity, or a combination of both.

With improved statistics with respect to Stauffer & Hartmann (1986) and the context provided by the new evidence discussed above, the existence of differences between active and inactive single stars of spectral types late-K and M was analyzed in the present work and published in Morales et al. (2008a) using luminosities directly determined from accurate trigonometric parallaxes and carrying out a thorough analysis of possible biases, such as the effect of pre-main sequence (PMS) and binary stars. The differences were computed as effective temperature and radius variations, thus if active stars were indeed cooler and larger than their inactive counterparts, while keeping similar luminosities, this should be observable in single field stars (in addition to close binaries) thus generalizing the proposed stellar activity scenario to all low-mass stars.

3.4.1 Selection of the sample of late-K and M stars

The sample used to test this hypothesis was composed of selected late-K and M dwarfs from the Palomar/Michigan State University survey of nearby stars (hereafter PMSU Reid et al. 1995; Hawley et al. 1996). This catalog lists the position, absolute magnitude (M_V), distance, TiO, CaH and CaOH spectral indices, H α equivalent width and proper motions for each of the 1966 stars that it contains. The distances listed are averaged combinations of Hipparcos trigonometric parallaxes and spectrophotometric determinations. Because of the working hypothesis of the T_{eff} dependence on activity, only objects with direct trigonometric parallaxes were useful because spectroscopic and photometric parallaxes could be biased by activity. The restriction of trigonometric parallaxes reduced the number of stars in the working sample to 746, with $1.3 < d < 58.0$ pc and $6.65 < M_V < 16.0$ mag.

The photometry in the IR bands was used to calculate the bolometric magnitude (i.e., luminosity) of the stars in the sample because of the weaker dependence on the bolometric correction (BC), which could be a potential source of large uncertainty (for M-type stars variations of 200 K in T_{eff} produce only changes below 0.1 mag in BC_K). Thus, the comparison between active and inactive stars with the same luminosity is more reliable if M_{bol} is computed from the K band rather than from the V band. The former is also less affected by variability caused by surface inhomogeneities. The sample was cross-matched with the 2MASS and *ROSAT* survey catalogs to obtain J , H and K_s magnitudes and L_X for each star. K_s was transformed to the K Johnson band (Alonso et al. 1994) to compute BC_K using the models in Bessell et al. (1998) as a function of T_{eff} . The available trigonometric distances were used to compute M_K and, subsequently, M_{bol} . The TiO5 index was

Table 3.1: Distance and radiative properties of the inactive sample of stars from the PMSU survey.

PMSU number	Identification	d (pc)	TiO5	T_{eff} (K)	K_s	M_{bol}
6	G1 1	4.4	0.610	3560	4.523	8.95
7	G1 2	11.5	0.660	3640	5.853	8.18
11	G1 4 A	11.8	0.830	3950	5.262	7.42
12	G1 4 B	11.8	0.810	3900	5.284	7.46
15	LHS1019	17.6	0.530	3430	7.631	9.07
17	G1 4.2B	25.6	0.870	4060	5.266	7.82
23	V351	21.9	0.770	3820	6.980	7.85
27	G1 7	23.4	0.780	3840	7.856	8.57
30	G031-030	25.5	0.790	3860	7.119	7.64
38	G242-048A	19.6	0.630	3590	6.904	8.08

A few lines of this table are given here for reference. The complete sample of stars is available electronically in Morales et al. (2008a).

used as spectral type indicator with the prescription on Reid et al. (1995), which suggests a linear relationship with small scatter between this spectral index and the spectral subtype of M stars given by:

$$\text{Sp.Type.} = -10.775 \cdot \text{TiO5} + 8.2. \quad (3.6)$$

Effective temperatures were derived using the spectral type-temperature correspondence in Bessell (1991) (which is similar to that of Leggett et al. 1996) and the equivalent width of the $\text{H}\alpha$ emission line was used as an indicator of magnetic activity. An iterative procedure was used to ensure consistency between the adopted T_{eff} and BC_K .

Active and inactive stars were considered separately in the analysis of the sample. Those stars with the $\text{H}\alpha$ line in absorption were classified as inactive while those with $\text{H}\alpha$ in emission were considered to be active. Note that this criterion only identifies as active stars those with high levels of activity, since mildly active stars can still have $\text{H}\alpha$ in absorption (e.g. Cram & Mullan 1979). Following this approach, 72 stars out of the total 746 turn out to be active. Tables 3.1 and 3.2 list part of the sample of inactive and active stars as guidance.

It is important to emphasize that the comparison of these stars is only meaningful if both sets of active and inactive single stars are equivalent in terms of evolution and metallicity so particular attention has to be taken both on the age and the metallicity of these stars:

- **Age:** The comparison between active and inactive late-K and M-type stars needs to be restricted to main sequence stars. The relatively short Pre Main Sequence (PMS) evolutionary phase, in which stars are also magnetically active, would break the one-to-one correspondence between luminosity and mass

Table 3.2: Distance and radiative properties of the active sample of stars from the PMSU survey.

PMSU number	Identification	d (pc)	TiO5	EW H α (\AA)	T_{eff} (K)	K_s	M_{bol}
70	GJ 3029	20.0	0.480	3.700	3340	7.447	8.62
140	Gl 31.2B	33.8	0.350	1.120	3080	7.124	9.71
165	LTT10301A	12.0	0.450	4.880	3280	7.119	9.41
353	GJ 1041 B	29.8	0.540	2.020	3440	7.119	7.41
411	LHS1377 A	14.2	0.470	2.100	3320	7.131	9.05
412	LHS1376 B	14.2	0.410	3.500	3190	7.887	9.83
478	GJ 1049	16.5	0.820	2.000	3930	5.757	7.20
497	G078-003B	23.5	0.300	3.070	3000	10.217	11.12
707	Gl 157 B	15.8	0.560	2.400	3470	6.927	8.59
742	Gl 166 C	5.0	0.340	3.940	3070	5.962	10.20

A few lines of this table are given here for reference. The complete sample of stars is available electronically in Morales et al. (2008a).

and therefore invalidate the comparisons. Thus, the active star sample was cleaned from possible PMS objects. There are only a few known young star associations and moving groups in the solar neighborhood and these have well-defined space motions. Using the catalogs of young moving groups (López-Santiago et al. 2006, D. Fernández, private communication), a total of 22 stars (9 of them classified as active) that belong to ensembles with ages younger than ~ 200 Myr were removed from the sample. Since this is a crude approach, an independent theoretical estimation of the expected number of PMS stars as a function of mass were carried out for comparison. Using the models of Baraffe et al. (1998) and assuming a constant star formation rate in the solar neighborhood, the fraction of PMS stars was estimated just by calculating the ratio of the time spent in the PMS phase and the total time during which a star would be classified as active. This calculation yielded a fraction of PMS stars of 20% to 10% (decreasing with mass) for the parameters of the sample. Such values turn out to be close to the actual fractions found when considering kinematic restrictions.

- **Metallicity:** Due to the effect of the chemical composition on the radiative properties of the stars, low-metallicity halo stars could also alter the results of the inactive star bins. Thus, high-velocity stars were removed from the sample. Subdwarfs were also disregarded using the CaH2-TiO5 prescription given in Bochanski et al. (2005). A total of 7 stars were eliminated at this step. In this way, both the inactive and active star samples contain disk stars and should have largely similar metallicities.

Finally, close binary stars were also removed from the list since the aim of this analysis is to test if single active stars show the same discrepancies with the models as close binaries. A total of 22 binaries (14 with H α in emission) were identified and rejected using SIMBAD and the lists given in Gizis et al. (2002) for the PMSU sur-

vey. The sample ended up with a total of 695 single main sequence disk stars, 48 active and 647 inactive.

3.4.2 Differences between active and inactive stars

In order to explore the existence of differences between the active and the inactive stars, the sample was grouped in M_{bol} (i.e., luminosity) bins. The bin size was selected to be 1 magnitude to keep a statistically significant number of stars in each bin. Note that, since the mass-luminosity relationship is so tight for low-mass stars (because post-ZAMS evolution is so slow), mass and luminosity bins are equivalent. Because of the need to use fairly large M_{bol} bins, the results could be potentially affected by some biases and selection effects:

1. A selection effect could be caused by the use of $\text{H}\alpha$ emission as activity criterion, which is more sensitive for stars of lower photospheric luminosities.
2. It is well known that the number of active stars increases towards later spectral types, i.e., decreasing effective temperature (e.g. West et al. 2004), which could tend to give more weight to the cooler active stars in each luminosity bin.

Fortunately, both effects can be corrected using the statistics available in the PMSU sample itself by computing the ratio of active to inactive stars as a function of the TiO5 index, as shown in Figure 3.7, in which active stars are selected using the $\text{H}\alpha$ emission criterion. To correct for the biases, the parameters related to active stars were weighted with the quantity $N_{\text{inactive}}/N_{\text{active}}$ estimated at their respective TiO5 index values in all subsequent calculations. The correction had a small (albeit non negligible) effect on the mean TiO5 indices of the bins. As a check, the same corrections were computed using the active star ratios in West et al. (2004) and Bochanski et al. (2005) and the results are identical.

Figure 3.8 illustrates the distribution of stars in the TiO5 versus $\text{H}\alpha$ equivalent width (EW) diagram ($\text{H}\alpha$ EW = 0 means line in absorption) for the 695 single main sequence, disk stars of the sample. The average TiO5 index for each M_{bol} bin is shown in Figure 3.8 for active and inactive stars separately. In Table 3.3 the differences between active and inactive stars are listed for statistically significant bins; M_{bol} bins with few stars (typically 2 or less) were not considered in the figure and subsequent comparisons. Also provided are the average values of $\log(L_X/L_{\text{bol}})$ computed for active stars using the *ROSAT* observations and the prescriptions given in Schmitt et al. (1995). These ratios are at the saturation level (Pizzolato et al. 2003) for all luminosity bins. This indicates that the active sample is representative of stars with very high activity levels. It is obvious both from the plot and from the table that active stars have systematically lower TiO5 indices (i.e., lower effective

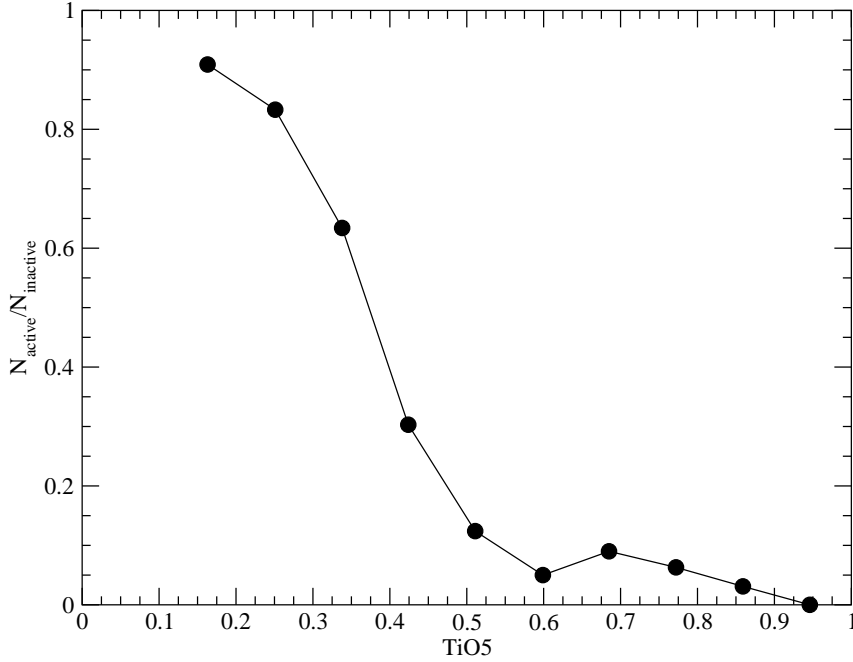


Figure 3.7: Ratio of active to inactive stars as function of the TiO5 index for the full PMSU sample. Active stars are defined as those with H α emission.

Table 3.3: Differences between mean values for active and inactive stars for each bin of M_{bol} with statistical significance.

M_{bol} bin	N_{inactive}	N_{active}	$\langle \Delta \text{TiO5} \rangle$	$\langle \Delta T_{\text{eff}} \rangle$ (K)	$\langle \Delta R/R \rangle$ (%)
7.0 – 8.0	286	13	-0.066 ± 0.038	-128 ± 62	6.9 ± 3.5
8.0 – 9.0	208	12	-0.066 ± 0.018	-107 ± 29	6.3 ± 1.8
9.0 – 10.0	72	13	-0.059 ± 0.012	-118 ± 22	7.3 ± 1.4
10.0 – 11.0	13	5	-0.030 ± 0.026	-59 ± 50	3.8 ± 3.3

M_{bol} bin	N_{inactive}	N_{active}	$\langle \Delta(V - K) \rangle$	$\langle \log(L_X/L_{\text{bol}}) \rangle_{\text{active}}$
7.0 – 8.0	286	13	0.34 ± 0.26	-3.11 ± 0.03
8.0 – 9.0	208	12	0.31 ± 0.07	-3.19 ± 0.11
9.0 – 10.0	72	13	0.31 ± 0.08	-2.87 ± 0.14
10.0 – 11.0	13	5	0.30 ± 0.24	-3.30 ± 0.11

temperatures) than their inactive counterparts of similar luminosity.

The mean TiO5 differences in Table 3.3 are all positive and quite similar in all magnitude bins. These index differences can be transformed into temperature differences using the calibrations of Bessell (1991) and eventually into radius differences just by assuming that the luminosity of the stars is not affected by activity as found from the comparison between models and observations of low-mass stars in eclipsing

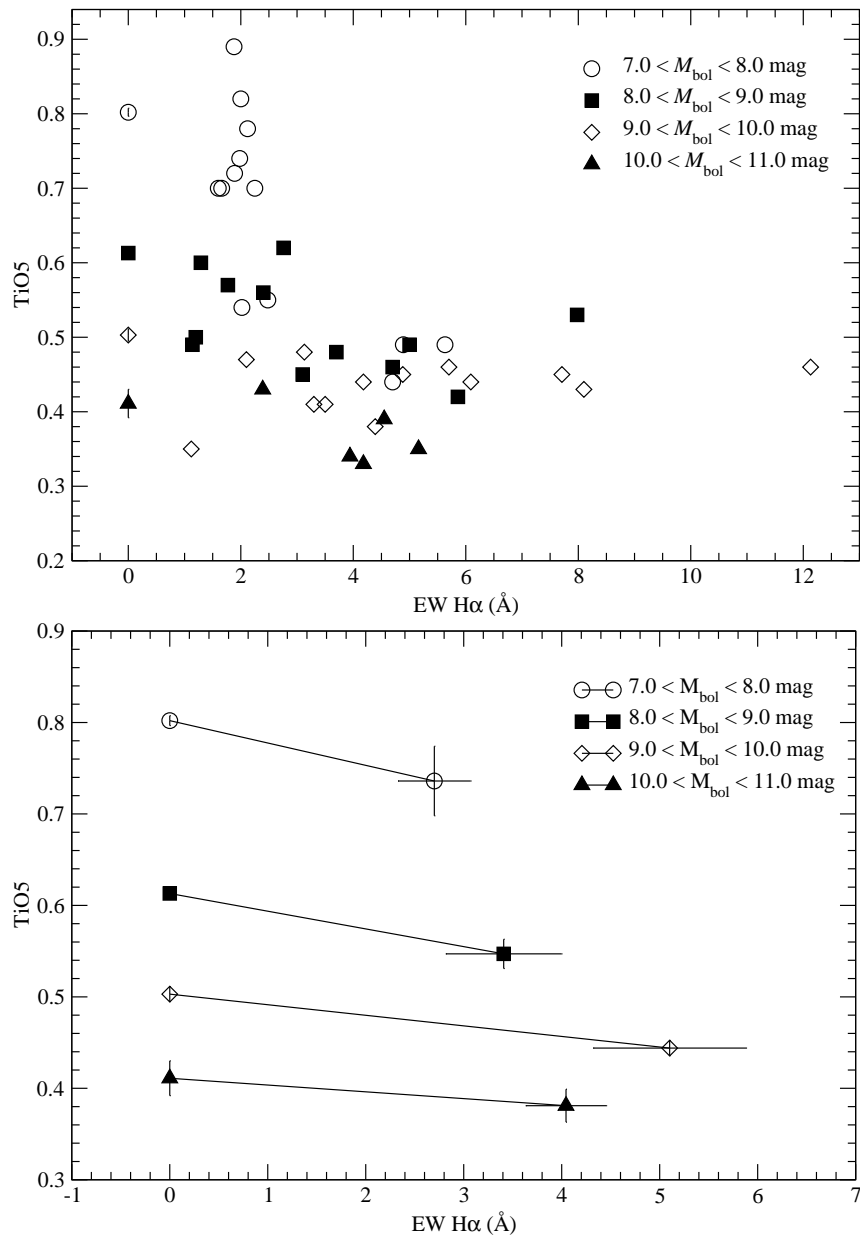


Figure 3.8: Distribution of active and inactive stars in TiO5 vs. EW H α for bins with statistical significance. Top: Single values for each active star and mean values for inactive stars. Bottom: Mean values for each M_{bol} bin.

Table 3.4: Effective temperature and radius differences of active stars calculated from a polynomial fit to inactive stars.

M_{bol} bin	N_{active}	$\langle \Delta T_{\text{eff}} \rangle$ (K)	$\langle \Delta R/R \rangle$ (%)
7.0 – 8.0	13	-106 ± 60	6.9 ± 3.5
8.0 – 9.0	12	-128 ± 19	7.8 ± 1.2
9.0 – 10.0	13	-120 ± 7	7.5 ± 0.5
10.0 – 11.0	5	-65 ± 16	4.5 ± 1.0

binaries. Then if $L_{\text{active}} \simeq L_{\text{inactive}}$, the radius difference can be calculated as:

$$\frac{R_{\text{ac}} - R_{\text{inac}}}{R_{\text{inac}}} = \left(\frac{T_{\text{eff, inac}}}{T_{\text{eff, ac}}} \right)^2 - 1 \quad (3.7)$$

These values are also listed in Table 3.3.

Since differences in radius are computed through temperature ratios, the results are almost independent of the T_{eff} scale adopted, which is still controversial for M-type stars. A cross-check with the T_{eff} calibrations of Schmidt-Kaler (1982) and de Jager & Nieuwenhuijzen (1987) expectedly yielded the same results. The trend of lower temperatures and larger radii for active stars has high statistical significance since similar differentials are obtained in all luminosity bins.

To rule out a possible effect of the M_{bol} binning procedure itself on the differences reported, an alternative approach were performed. First, a third order polynomial of the form $T_{\text{eff}} = f(M_{\text{bol}})$ was fitted to the inactive star sample. Then, for each individual active star, the temperature difference (and radius difference) between the observed value and the one predicted by the polynomial fit was computed. The results are given in Table 3.4, and are very similar to those in Table 3.3, which were calculated from M_{bol} bins.

A further useful check of the results comes from restricting the analysis to only stars that have been explicitly classified as single through high-resolution spectroscopy (Gizis et al. 2002). Although the statistics are less significant (with 127 inactive and 19 active stars), the mean temperature and radius differences for each M_{bol} bin are within one sigma of those in Table 3.3.

Table 3.3 also lists the mean differences in the $(V - K)$ color index, which are a direct consequence of the different average T_{eff} values between active and inactive stars. The relatively large scatter of these means (especially that of the first M_{bol} bin) may be caused by the variability in the V band of the stars in the active sample. This stems from the existence of surface spots with various cycles that could affect single-epoch V -band measurements but not K -band measurements that are more

immune to spot-induced variability. Note that no obvious or only marginal color differences for active stars have been reported before (see, e.g., Hawley et al. 1996; Bochanski et al. 2007). This would seem to stand in contradiction with the results found here, but it does not. It is important to emphasize that such color comparisons are always carried out using spectral types as fiducial. Thus, the lack of color differences between active and inactive stars of the same spectral types is just revealing that they have the same temperatures and spectral energy distributions, which is not surprising. The color differences found correspond to active and inactive stars of the same luminosity, which is equivalent to mass, and therefore a fundamental stellar property. Further, these are in good agreement with the differences in the spectral energy distribution caused by activity found by Stauffer et al. (2003) in Pleiades K-type stars.

A possible effect that could alter the outcome of this study is the influence of metallicity. Obviously, a metal-poor star will have intrinsically weaker TiO bands and therefore appear as hotter when the TiO5 index is used. For example, a metallicity decrease of 0.5 dex corresponds to a ~ 200 K higher effective temperature. If there was a mean metallicity difference between the two samples used (active and inactive) this could affect their mean temperature difference (and inferred radius difference) based on the TiO5 index. There is certainly a metallicity spread within the two samples used, characteristic of a disk population, but the key issue here is whether the two samples have similar mean metallicities. A possible approach to test this is by directly using the metallicity calibration of Bonfils et al. (2005). However, this calibration is based in the $(V - K)$ index and, according to the hypothesis of an activity effect, the systematic differences in this index will cause a spurious systematic metallicity difference.

It is reasonable to assume that, on average, the inactive sample will be older than the active sample, just because there is a well-established age-activity relationship (Skumanich 1972). However, this age difference does not imply a difference in the mean metallicities of both samples because numerous studies have concluded that there is no age-metallicity correlation in disk stars, as shown by Nordström et al. (2004) and references therein. The average metallicity of the Nordström et al. catalog, when applying the kinematic constraints of the sample used here (i.e., $-165 < U < 130$ km s $^{-1}$, $-130 < V < 40$ km s $^{-1}$ and $-90 < W < 80$ km s $^{-1}$), is $[M/H] = -0.17$. Using Bonfils et al. (2005) calibration in the inactive sample, whose stars should have unbiased $(V - K)$ indices, a mean value of $[Fe/H] = -0.14$ is obtained. Both averages are in good agreement and indicate that the inactive sample is representative of the overall population of the solar neighborhood. If the Bonfils et al. calibration is applied to the active sample, also under the assumption that their $(V - K)$ indices are unbiased, a mean metallicity that is about 0.3 dex higher, $[Fe/H] \sim +0.15$, is found. Such high mean metallicity value is very unlikely

Table 3.5: Active/inactive star radius differences using restrictive kinematic criteria.

M_{bol} bin	$N_{\text{inactive}}/N_{\text{active}}$	$\langle \Delta R/R \rangle$ (%)
7.0 – 8.0	68/8	11.6 ± 4.2
8.0 – 9.0	39/3	9.1 ± 2.9
9.0 – 10.0	19/5	4.9 ± 2.3
10.0 – 11.0	1/3 ^a	

^a Mean not computed because of insufficient statistics.

in the context of the Nordström et al. results, thus suggesting that the $(V - K)$ indices of the active star sample are indeed biased because of the effect of activity.

Additional tests to eliminate the possibility of metallicity effects in the results arising from contamination by metal-poor stars belonging to the thin disk were carried out. When selecting only stars with UV values in the interval $(-90, 50)$ km s⁻¹, which would be characteristic of the overall thin disk, the results are nearly identical to those in Table 3.3. A further test was considered adopting very restrictive kinematic criteria in both the active and the inactive star samples to ensure that both belong to the young disk population, although sacrificing statistical significance. If metallicity was responsible for the observed differences in the radii and temperature, they are expected to disappear when both samples come from the same population. Thus, only stars belonging to the young disk were selected using the UV criteria of Montes et al. (2001) plus $-25 < W < 25$ km s⁻¹. The resulting radius differences are listed in Table 3.5. As can be seen, the differences are fully compatible within the error bars with those of the full sample, therefore indicating that metallicity effects do not play a significant role in the conclusions of this analysis.

3.5 Activity hypothesis

The comparison between models and observations from CM Dra and IM Vir, and the analysis on the active and inactive sample of single stars, performed in this chapter add further evidence to the hypothesis that activity is a feasible explanation for the observed discrepancies. Figure 3.9 displays the fundamental properties determined for CM Dra and IM Vir along with the observations of other DDLEBs. Only mass and radius determinations with accuracies below the 3% level for stars in eclipsing binaries are used. The plots in this figure clearly show that the discrepancies found for CM Dra and IM Vir are in agreement with the findings of other low-mass binary systems. These differences between models and observations are particularly remarkable below $0.8 M_{\odot}$, showing a clear offset towards larger radii and cooler effective temperatures. Above this mass limit the radius and temperature differences due to the evolution of the stars can be an important contribution to the offset.

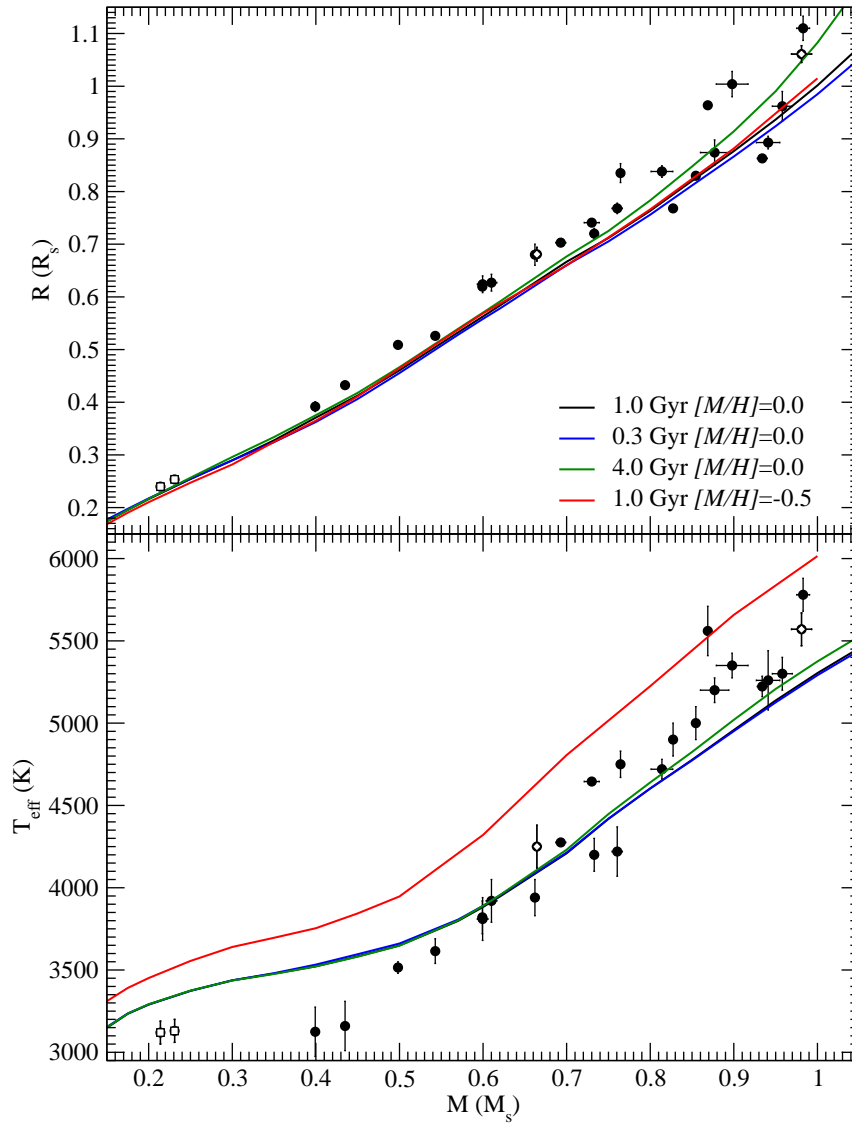


Figure 3.9: $M - R$ and $M - T_{\text{eff}}$ relationships of the theoretical Lyon stellar models (Baraffe et al. 1998) compared with the observations from DDLEBs with masses and radii determinations accurate below the 3% level. CM Dra and IM Vir components are plotted as open squares and open diamonds, respectively.

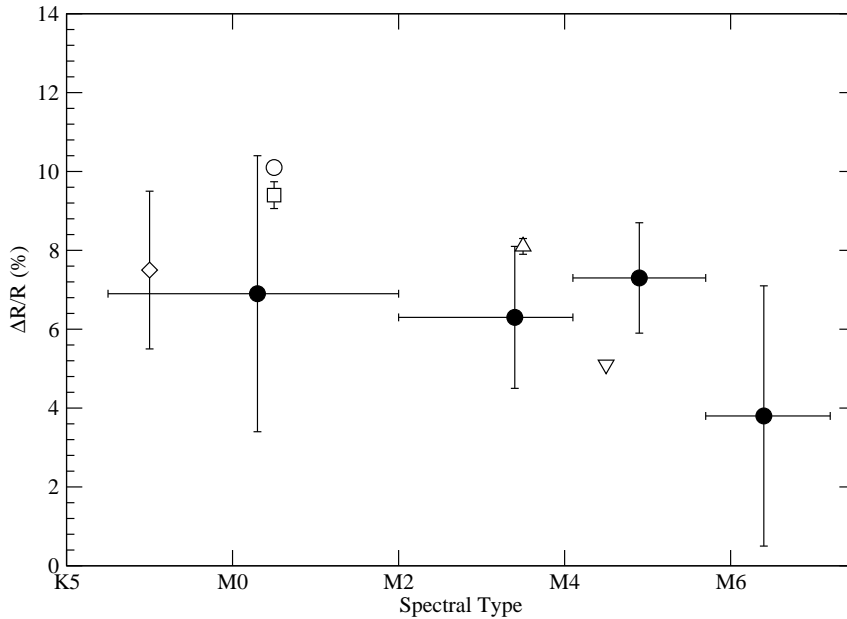


Figure 3.10: Comparison of the differentials of radii over spectral type for single active and inactive stars (filled circles) with results from the eclipsing binaries with highest accuracy (open symbols): IM Vir B (diamond), YY Gem (circle), GU Boo (square), CU Cnc (up triangle) and CM Dra (down triangle).

On the other hand, Figure 3.10 shows the radius differences between active and inactive single main sequence stars given in Table 3.3 translated into spectral type bins. The radius differences obtained from CM Dra, IM Vir B, as well as, well-known binaries such as YY Gem (Torres & Ribas 2002), GU Boo (López-Morales & Ribas 2005) and CU Cnc (Ribas 2003) are also plotted for comparison. Note that the two radius differentials have slightly different meanings. While eclipsing binary values come from the direct comparison of radius measurements with the predictions of the theoretical models of Baraffe et al. (1998), which do not include the effects of stellar activity, the values for single stars are computed from the difference between active and inactive samples. As can be seen, the differentials from these two completely independent approaches are in very good agreement, thus reinforcing that the magnetic activity is the responsible, at least in part, of the discrepancies between theoretical models and observations.

In a theoretical approach, Chabrier et al. (2007) examined the effect of rotation and activity on the Lyon stellar models both as a reduction of the convective transport efficiency and the obstruction of the radiation due to the presence of surface

spots. The first of these effects is equivalent to a reduction of the mixing length parameter (α) whereas the second can be parameterized in terms of a fractional spot coverage. They conclude that the observations can be reproduced with small values of α , although its effect is minimal for fully convective stars, or with spot coverages of about 30-50% of the star.

The results of this chapter and the conclusions of the theoretical work of Chabrier et al. (2007) reinforce the hypothesis that stellar activity is a plausible explanation of the discrepancies between models and observations of low-mass stars. A crucial test of the Lyon stellar models that include activity effects to check their consistency with the observations from DDLEBs will be described in next chapter.

Chapter 4

Stellar models of active stars

The main results of the former chapters confirm the reports indicating that active stars in DDLEBs are larger and cooler than predicted by models. The comparison between active and inactive single stars with equal luminosity (i.e. mass) also draws similar conclusions. These findings clearly point out that magnetic activity is a relevant parameter that must be accounted for in the stellar structure of low-mass stars, which are the main component of the Galaxy. Over the past decades, substantial progress towards the understanding of the structure and evolution of low-mass stars has been made, also including activity effects. Chabrier et al. (2007) showed that the inclusion of rotation and magnetic field effects on the models of Baraffe et al. (1998) could explain the discrepancies between the observed and theoretically predicted mass-radius relationship of DDLEBs if small values of α (mixing-length) are considered, or with spot coverages of 30-50% of the stellar surfaces.

The accurate fundamental properties of low-mass DDLEBs, and especially the case of CM Dra (Morales et al. 2009a), that provides precise characterization of two fully convective stars, makes it worthwhile to carry out a thorough analysis of the agreement between observations and theory using the context suggested in Chabrier et al. (2007). In this chapter, the analysis of the effect of activity both on the models of stars and on the observations of DDLEBs done in collaboration with the stellar modelling group of Lyon is described, and an scenario to explain the discrepancies in radii and effective temperatures between models and observations is proposed. The discussion in this chapter is published in Morales et al. (2010).

4.1 Activity parameters on the Lyon stellar models

As all standard stellar models, the Baraffe et al. (1998) models neglect the stellar rotation and the magnetic field effects in the stellar structure equations. However,

Chabrier et al. (2007) suggested that both rotation and magnetic fields can cause significant changes on the energy transport by convection and on the stellar surface, and thus on the entire stellar structure:

- **Convective transport:** The authors suggest that the effect of magnetic field and rotation alter the efficiency of convective energy transport, thus inhibiting convective motions within the stars. Effectively, this can be modelled by setting the mixing length parameter (α) to lower values than those used for solar models.
- **Stellar surface:** The magnetic fields in fast rotating stars, such as those in DDLEBs, produce a high level of magnetic activity on these objects that can be associated with the appearance of dark spots covering the radiative surface. These surface spots can be modelled by assuming a new stellar luminosity, $L' \propto (1 - \beta) R'^2 T_{\text{eff}}'^4$, where R' and T_{eff}' are the modified stellar radius and effective temperature, respectively, and β is the factor of spots blocking the outgoing luminosity due to their lower temperature (further details on this parameter are given later on Section 4.3).

The results of Chabrier et al. (2007) show that both these scenarios predict larger radius than standard stellar models, but while the effect of spots is significant over the entire low-mass domain, the effect of convection is relatively small for fully convective stars ($M \leq 0.35 M_{\odot}$) because convection is nearly adiabatic and changing the mixing length parameter has a modest impact on their stellar structure. Figure 4.1 (corresponding to figure 1 of Chabrier et al. 2007), shows these models with different sets of α and β parameters compared with a sample of observational values. Regarding the effect of α , models show good agreement with the observations for values of $\alpha \sim 0.5$ only for stars more massive than $0.6 M_{\odot}$, but it must be decreased to rather unphysical values to explain the fully convective stars of CM Dra or a system such as CU Cnc. On the other hand, Chabrier et al. (2007) conclude that assuming 30% of the stellar radiative surface covered by completely dark spots, i.e., $\beta \approx 0.3$, yields a smaller heat flux output and thus larger radii and cooler effective temperatures.

Since radius discrepancies have been reported over a wide range of masses, this results may be indicating that either the contribution of spots or a combination of spots and activity effect on the convective transport are needed to reconcile models with observations. In next sections a thorough test of these models with the best known-eclipsing binaries is performed to check the consistency between the spots coverages suggested by Chabrier et al. (2007) and those reported for DDLEBs, and to understand which are the relative contributions of spots and convection inhibition on the radius discrepancies of active stars.

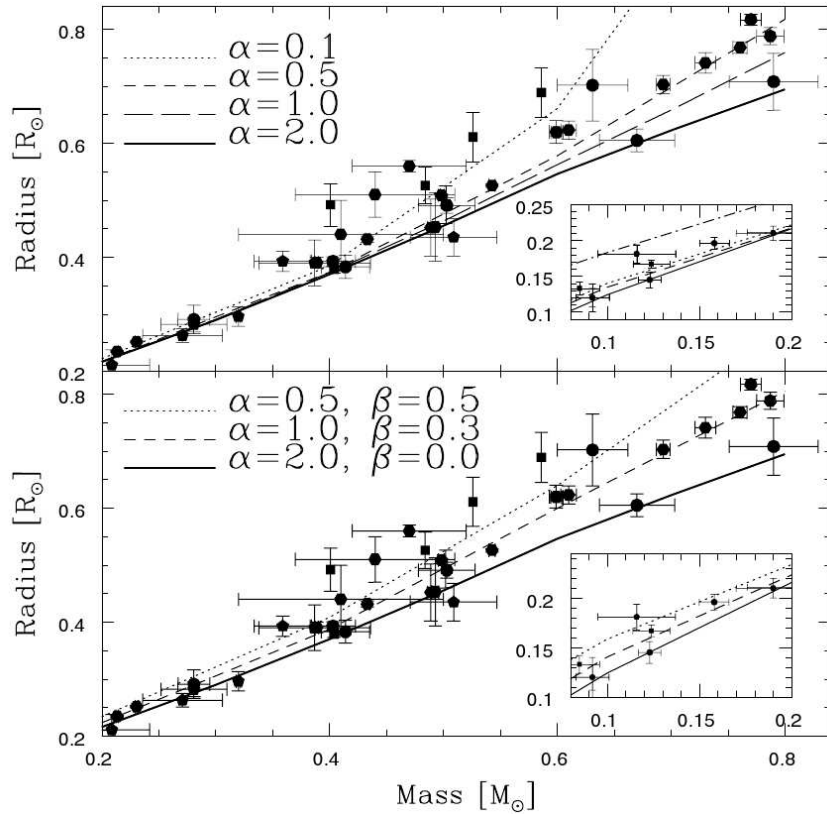


Figure 4.1: $M - R$ relationships of the theoretical Lyon stellar models with different α and β parameters. Figure reproduced from Chabrier et al. (2007).

4.2 Sample of low-mass DDLEBs

To test stellar structure models, masses and radii of stars need to be known with accuracies down to the few percent level (Andersen 1991; Torres et al. 2010). Thus, for this analysis only the known main sequence low-mass stars with accuracies better than 3% on its masses and radii were selected. As reported recently by Torres et al. (2010), special attention should be paid both on the precision and the accuracy of the measures, and so we have excluded from our sample systems with error estimations not clearly described. Furthermore, only main sequence systems with ages below 5 Gyr and masses below $0.8 M_{\odot}$ were selected to restrict radius differences due to evolution below 2% and also to minimize the effect of mixing length differences between low-mass and solar mass models. The mechanical and thermal properties for each component of the selected systems are listed in Table 4.1, as well as the age and metallicity when known.

Table 4.1: Properties of observed EBs included in our sample.

EB	P (days)	M M_{\odot}	R R_{\odot}	T_{eff} (K)
V818 Tau B	5.61	0.7605 ± 0.0062	0.768 ± 0.010	4220 ± 150
IM Vir B	1.31	0.6644 ± 0.0048	0.681 ± 0.013	4250 ± 130
NGC2204-S892 A	0.45	0.733 ± 0.005	0.720 ± 0.010	4200 ± 100
NGC2204-S892 B		0.662 ± 0.005	0.680 ± 0.020	3940 ± 110
GU Boo A	0.49	0.6101 ± 0.0064	0.627 ± 0.016	3920 ± 130
GU Boo B		0.5995 ± 0.0064	0.624 ± 0.020	3810 ± 130
YY Gem A & B	0.81	0.5992 ± 0.0047	0.6194 ± 0.0057	3820 ± 100
CU Cnc A ^b	2.77	0.4349 ± 0.0012	0.4323 ± 0.0055	3160 ± 150
CU Cnc B ^b		0.3992 ± 0.0009	0.3916 ± 0.0094	3125 ± 150
CM Dra A	1.27	0.2310 ± 0.0009	0.2534 ± 0.0019	3130 ± 70
CM Dra B		0.2141 ± 0.0010	0.2396 ± 0.0015	3120 ± 70

EB	$[M/H]$	Age Gyr	$v_{\text{rot, sync}}$ km s^{-1}	Ref. ^a
V818 Tau B	0.13	0.6	6.95 ± 0.09	1
IM Vir B	-0.28	2.4	26.12 ± 0.50	4
NGC2204-S892 A	-	-	80.9 ± 1.1	2
NGC2204-S892 B			76.4 ± 2.2	
GU Boo A	~ 0	1.0	64.7 ± 1.6	3
GU Boo B			64.4 ± 1.6	
YY Gem A & B	~ 0	0.4	38.88 ± 0.36	3
CU Cnc A ^b	~ 0	0.32	8.02 ± 0.10	3
CU Cnc B ^b			7.30 ± 0.17	
CM Dra A	-	4.1	10.02 ± 0.08	4
CM Dra B			9.51 ± 0.07	

^aReferences: 1. Torres & Ribas (2002); 2. Rozyczka et al. (2009); 3. Torres et al. (2010); 4. This work

^b T_{eff} could be underestimated due to the presence of circumbinary dust.

Comparison of this sample with $M - R$ and $M - T_{\text{eff}}$ relationships from stellar models is shown on the panels of Figure 4.2. For the sample of Table 4.1, the comparison with the 1 Gyr solar metallicity model gives discrepancies with observations of 5.8% and -6.1% in radii and effective temperatures, respectively, for fully convective stars (CM Dra), and 7.8% and -3.0%, respectively, for partially radiative stars.

The individual effective temperatures are usually computed using different spectrophotometric calibrations for each system, thus introducing the potential for systematic errors. Furthermore, some DDLEB systems may have peculiarities, such as CU Cnc, which is supposed to have a circumbinary dust disk that may affect the temperature determination. Thus, to investigate the agreement between models and observations, the $M - R$ relationship will be primarily used because these two quantities are both fundamentally determined.

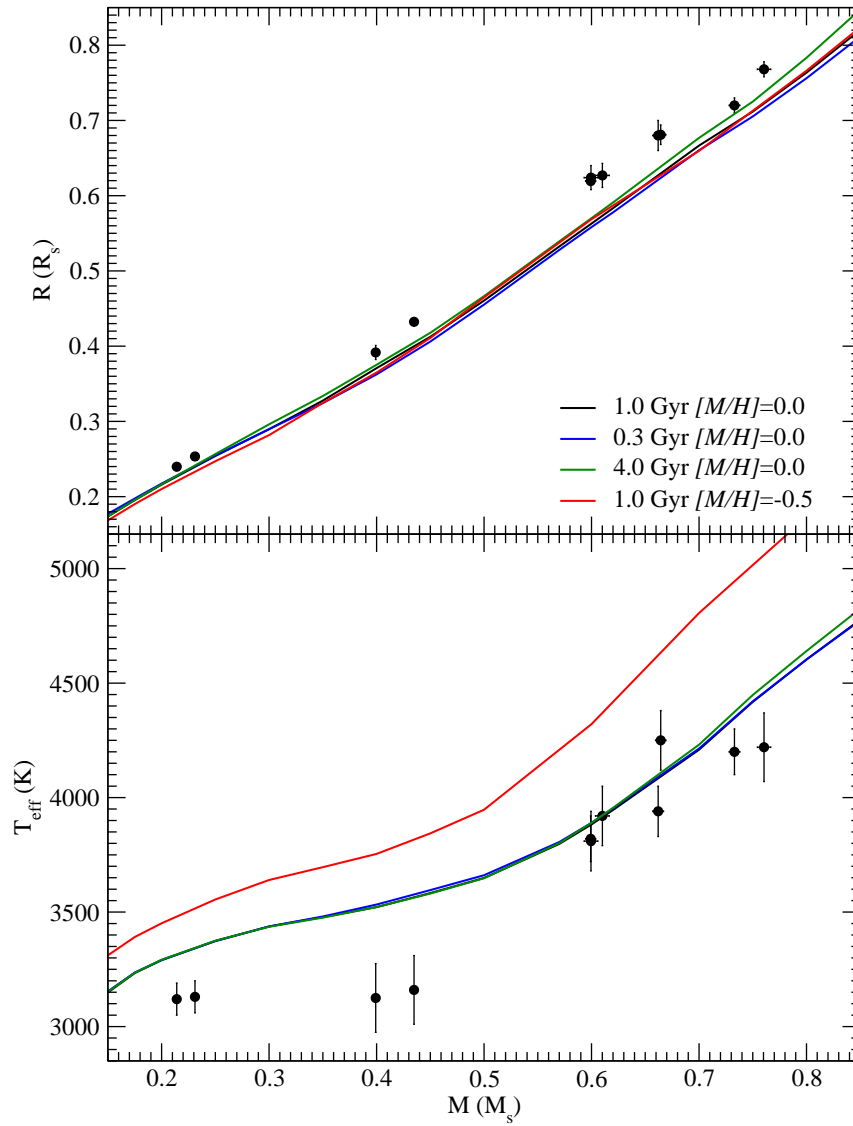


Figure 4.2: $M - R$ and $M - T_{\text{eff}}$ relationships of the theoretical Lyon stellar models compared with the observations from DDLEBs with masses and radii determinations accurate below the 3% level.

4.3 Effect of spots on DDLEB analysis

Before embarking on a careful fine-tuning of model parameters to reach agreement with observations it is worth evaluating whether the observed eclipsing binary parameters could be affected by the strong magnetic activity of the components. Time-variable brightness changes are a common signature of the presence of activity on low-mass stars both on single and eclipsing binaries. In the latter case, the modulation present on the light curves is combined with the eclipsing variability and, therefore, starspots must be taken into account to derive accurate stellar fundamental properties. The possibility that starspots could be responsible for systematic effects inherent to the light curve and radial velocity analyses in the case of the very active low-mass eclipsing binaries is studied in this section. As an example, in Section 2.2.4 it was already shown that spot can cause a ~ 15 s jitter on the CM Dra minima timings. Now, whether the fundamental properties determined from the classical modelling could be biased because of the presence of starspots in different geometries is analyzed.

As explained in Chapter 1, absolute physical properties of DDLEBs are obtained from the combination of the results of light and radial velocity curve analyses with modelling codes such WD. Just as a reminder, light curves yield properties such as the inclination of the orbit (i), the ratio of effective temperatures ($T_{\text{eff}2}/T_{\text{eff}1}$), the luminosity ratio in the light curve bandpass (L_2/L_1) and the surface pseudo-potentials (Ω_1 and Ω_2), which are related to the radii relative to the semimajor axis (r_1 and r_2). Radial velocity curves provide values for the mass ratio (q) and projected semi-major axis ($a \sin i$). The combination of the two modelling procedures yields the absolute properties of the components independently of models or distance calibrations. Radiative parameters, such as limb darkening and gravity darkening, relevant for light curve analyses, are usually taken from theory.

Besides, it was shown that the presence of spots on the surface of the components of a DDLEB system cause perturbations on both the light and radial velocity curves. The most prominent effect is on light curves, in the form of modulations in the out-of-eclipse phases. The WD code also introduces spots on the modelling assuming that they are circular and that they have an uniform temperature ratio with respect to the photosphere. With this simple model, properties of spots such as their location in co-latitude (θ_s , measured from North Pole) and longitude (ϕ_s), the angular size (r_s) and the temperature contrast with the photosphere, i.e., $\frac{T_{\text{eff},s}}{T_{\text{eff}}}$, where T_{eff} and $T_{\text{eff},s}$ are the effective temperatures of the photosphere and the spots, respectively, can be fitted. The values of ϕ_s and r_s are well constrained by the central phase of the modulation and its duration and amplitude, respectively, however the amplitude is also dependent on θ_s and $\frac{T_{\text{eff},s}}{T_{\text{eff}}}$, so these parameters are strongly

correlated with the size of spots.

In the case of active stars, the total luminosity of a spotted star is the addition of the contribution of the spots at an effective temperature $T_{\text{eff},s}$ and the immaculate surface at T_{eff} . If S and S_s are defined as the surface of the star and that covered by spots, respectively, the total luminosity is given by:

$$L = (S - S_s) \sigma T_{\text{eff}}^4 + S_s \sigma T_{\text{eff},s}^4. \quad (4.1)$$

Comparing this equation with the formalism introduced by Chabrier et al. (2007), it can be concluded that the β parameter is given by:

$$\beta = \frac{S_s}{S} \left[1 - \left(\frac{T_{\text{eff},s}}{T_{\text{eff}}} \right)^4 \right]. \quad (4.2)$$

This equation indicates that the β parameter is related with the properties of spots. For completely dark spots ($T_{\text{eff},s} = 0$), the term in brackets in Equation 4.2 is exactly one, therefore, β is a measure of the fraction of stellar surface covered by dark spots as defined by Chabrier et al. (2007). However, in the realistic case that spots are not completely dark the term in brackets is less than one and β is lower than the fraction of spotted surface. For a given T_{eff} and an estimation of the contrast of spots, Equation 4.2 provides the ratio of surface covered by spots when β is known, or vice versa.

Spot modelling results have been published for several of the best-known DDLEBs (Torres & Ribas 2002; Ribas 2003; López-Morales & Ribas 2005; Morales et al. 2009a,b) reporting both cold and hot spots with radii between $\sim 9^\circ$ and $\sim 90^\circ$ and with temperature factors down to 0.86. Hot spots can be interpreted as photosphere regions surrounded by large cool spots. Considering the spot parameters given in the above references for the cases of IM Vir, GU Boo, YY Gem, CU Cnc, and CM Dra, β values of up to 0.1 are found according to Equation 4.2. This value is much smaller than the range between 0.3 and 0.5 suggested by Chabrier et al. (2007). It must be mentioned, though, that since the relevant measures in DDLEB light curve analyses are differential magnitudes, the photometric variations used to derive the spot parameters are not sensitive to the total surface covered by spots but to the contrast between areas with different effective temperatures. For instance, an evenly spotted star would not show significant light curve variations. It is thus possible that DDLEBs could be more heavily spotted than simple photometric variations indicate and permit β values higher than 0.1. Thus, both the photometric variations that could produce such higher values of β , as well as, their effect on derived parameters from fits have to be checked.

4.3.1 Modulation on light curves

For M-type stars, an assumption of $T_{\text{eff}} \sim 3500$ K and spots about ~ 500 K cooler than the photosphere and β values between 0.3–0.5 corresponds to a fractional surface area of 65–100% covered by spots (as shown by Equation 4.2). To test the consistency between the theoretical modulations expected from different β values and the spot modulations observed on DDLEB light curves, a set of DDLEB systems with components randomly spotted were simulated and their light curves were generated with the WD code. Such theoretical light curves were subsequently compared with those observed in DDLEBs.

A code to randomly place spots on the surface of stars was developed for this purpose. Uniform longitude distribution was assumed and different distributions over latitude were tried. Granzer et al. (2000) calculate the probability of spot appearance for different latitudes as a function of spin period and mass. Their results show that for a star like the components of GU Boo (see Table 4.1), spots are formed in a band from 25° to 55° of co-latitude. Both bands (one per hemisphere) represent about one third of the stellar surface, which is not enough to simulate spot coverages with β greater than 0.15 (assuming spots 500 K cooler than the photosphere). Doppler tomography analyses have revealed the prominent existence of polar spots on active stars (Jeffers et al. 2007; Washuettl & Strassmeier 2001; see also Strassmeier 2009, and references therein). Thus, the distribution was extended to all stellar latitudes. Three distributions were considered, two of them similar to those given in Granzer et al. (2000), and the other for comparison:

- **Distribution 1:** A linear probability from the pole to 40° and from 45° to the equator with a plateau between 45° and 40° . This roughly mimics distributions of $0.6 M_\odot$ rapidly-rotating stars in Granzer et al. (2000).
- **Distribution 2:** A bilinear distribution from the pole to 70° with a peak at 25° . This is similar to the $0.4 M_\odot$ distribution in Granzer et al. (2000) for rapidly rotating stars but extended to cover β factors up to 0.3.
- **Uniform distribution:** A completely homogeneous distribution on longitude and latitude.

These distributions are shown in Figure 4.3 and it illustrates that Distribution 2 is more concentrated towards the poles. Additionally, to have reasonable computing time using the WD code, the number of spots on the stars was limited by imposing that the centers of two spots could not be closer than half their radius, i.e., each spot contributes at least $\sim 30\%$ of its surface to the total spot coverage.

The simulation procedure was executed as follows:

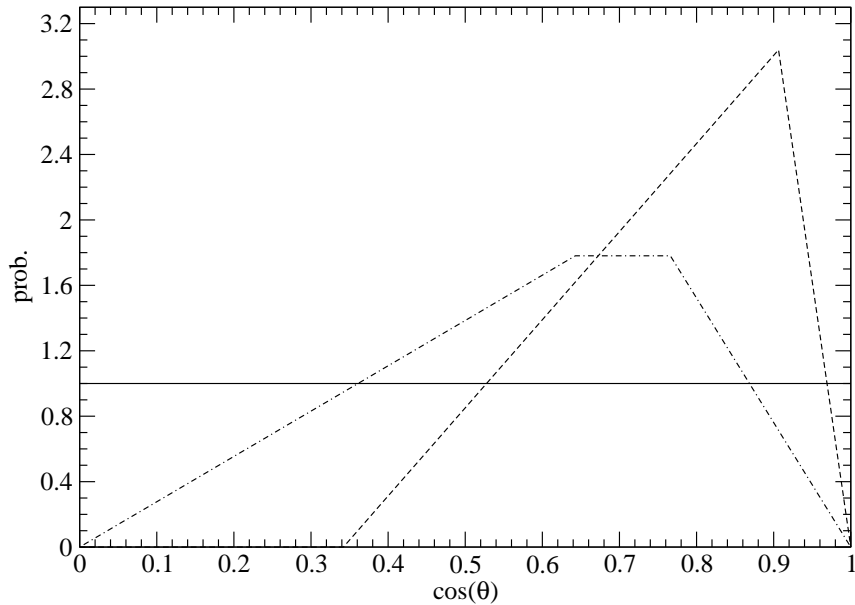


Figure 4.3: Probability density functions over $\cos \theta$ used to simulate spotted stars. The equator corresponds to $\theta = 90^\circ$. The uniform distribution (solid line), Distribution 1 (dot-dashed line) and Distribution 2 (dashed line) are described in the text.

1. Spots with a temperature contrast with the photosphere of 0.85 were considered, even on overlapping areas (i.e., the temperature contrast in the area where two spots overlap is also 0.85). This value constrains β between 0 and ~ 0.5 , the latter meaning a completely spotted stellar surface. In the case of Distribution 2 the upper value of β is ~ 0.35 . The spot radius was fixed to 10° in line with large spot groups measured on the Sun.
2. For each latitude distribution 25 light curves with spots randomly distributed over the surface of the components were simulated for different values of β .
3. The peak-to-peak variations on the out-of-eclipse phases of these simulated light curves were measured and the mean value of the 25 light curves was computed.

This procedure was done using the physical properties of GU Boo as template and using R -band light curves. However, since the effect of absolute masses or mass ratio on the light curves is negligible, this should be representative of the entire low-mass star domain.

The values of the peak-to-peak modulations found with these simulations were later compared with the real values for the best-known DDLEBs. Figure 4.4 shows

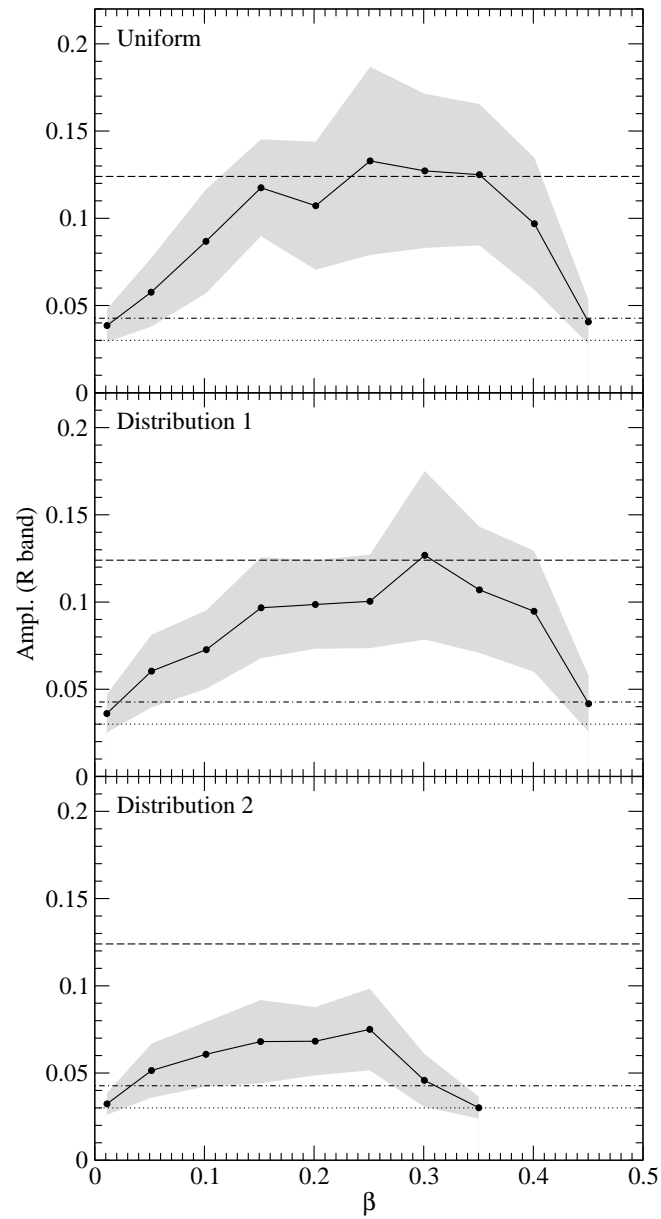


Figure 4.4: Amplitude of the modulations produced by different β spot scenarios using different spot distributions on R -band light curves. Each point is the mean value of 25 realizations and the shaded area shows the standard deviation of these modulations. The values reported in the literature for CM Dra (dotted line), YY Gem (dot-dashed line) and GU Boo (dashed line) are shown for comparison.

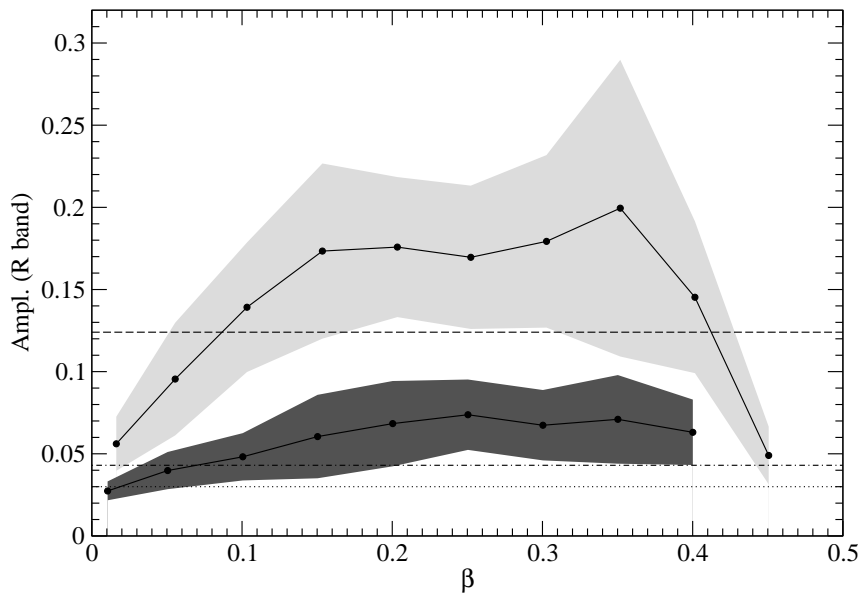


Figure 4.5: Same as Figure 4.4 for the uniform distribution comparing the cases of simulations using spots with radius of 15° (light shade) and 5° (dark shade).

the peak-to-peak modulations resulting from simulations for each distribution compared with a few observational values as reference. Large modulations are better explained by mild spot coverages assuming a uniform distribution or Distribution 1, while low spot signals are better reproduced by Distribution 2. However, the amplitude of these modulations depends on the size and thermal properties of the spots as shown on Figure 4.5. It is clear that the observed modulations could be explained with any of the distributions when considering the different spot sizes and the intrinsic dispersion of the modulation. Therefore, low amplitudes such as those of YY Gem and CM Dra could be recovered with a mild spot coverage with small size or low temperature contrast spots. Besides, the variability of the spot properties should also be taken into account since it could induce different modulations on different epochs as has been reported for the case of V band light curves of YY Gem, showing amplitudes of 0.09 mag and 0.055 mag in different seasons (Torres & Ribas 2002).

Several other distributions, such as linear, quadratic and square root from equator to poles were tested yielding results between the uniform and Distribution 1 cases.

4.3.2 Systematics on light curves due to spots

The simulations described above, were also used to investigate systematic effects of spots on fits to light curves. A thorough statistical analysis of the systematic deviations induced by the presence of spots on these parameters requires fitting all the simulated light curves by treating them as real observations. Typical light curve analyses involve testing fits for different parameters, especially when spots are present, since different spot configurations should be tested. Simultaneous fits of light curve in several bands are also preferable in order to avoid correlations between parameters such as limb darkening and radius. Besides, spot parameters are degenerate and thus the inversion of a light curve to recover the input parameters is an ill-posed problem. This implies carrying out a slow procedure consisting in adding spots and evaluating the relevance of the modulation to reach the best compromise between stability and the quality of the fit to the observations. For these reasons, fitting all the simulated curves is prohibitively time consuming. Thus, three simulated light curves for each distribution and for each of the β values 0.1, 0.2, 0.3 and 0.4 (33 light curves in total) were adjusted with the aim of inferring a general trend. We focused our attention on the R -band to reduce the computing time. This band is commonly used in the photometric follow-up of low-mass eclipsing binaries and it is representative of light curve analyses. A possible bias resulting from the correlation between radius and limb darkening coefficients should be negligible because the coefficients are computed from the same theoretical tables (Claret 2000a) both for simulations and fits. For each of the β values mentioned, three realizations with modulation amplitudes representative of the average were chosen as representative spotted light curves.

A random Gaussian noise of 1% of the flux was added to the simulations so that the typical scatter of light curves is reproduced and fits were subsequently performed using the WD code. Light-curve relevant parameters such as the inclination, temperature ratio, light ratio and surface potentials were fitted along with spot properties. Since some of the spot parameters are highly correlated, the latitude was fixed to 45° and spots 10% cooler or hotter than the photosphere were considered as a starting point of the fits. The free parameters were the longitude (ϕ_s) and size (r_s) of spots and, in a second step, the co-latitude (θ_s) and temperature contrast ($T_{\text{eff},s}/T_{\text{eff}}$). As the usual practice, as many spots as needed to obtain a realistic fit were included in the model and their location on the primary component, secondary or both at the same time was tested. All cases yielded satisfactory fits with 1–3 spots on different components. Best fits with $T_{\text{eff},s}/T_{\text{eff}}$ ratios of ~ 0.9 were found, thus indicating that spot groups could be modeled with a smoother temperature contrast than real. A phase shift was also set as a free parameter to account for phase corrections due to spots.

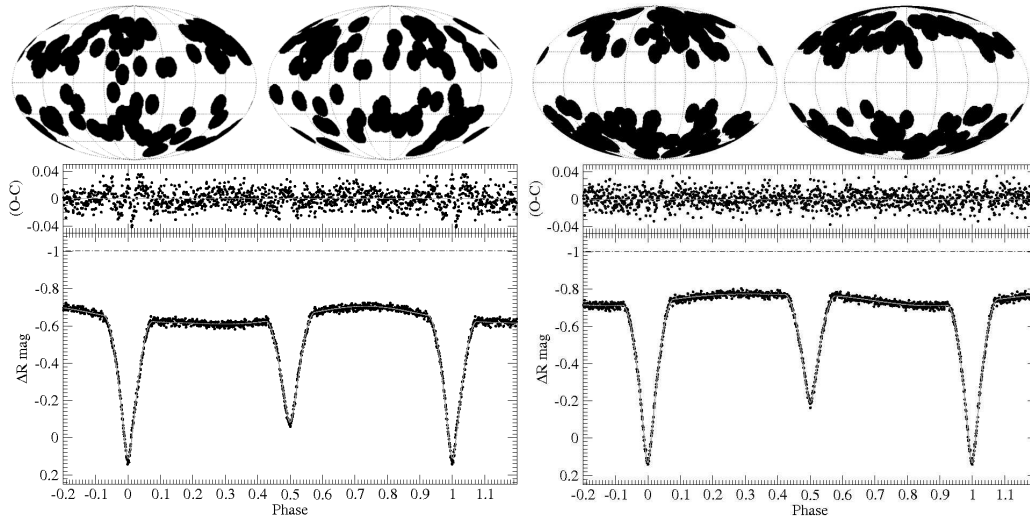


Figure 4.6: Two representations (left panel for Distribution 1 and right panel for Distribution 2) of simulated spotted DDLEB systems (primary component on the left and secondary on the right) with the resulting light curves. Star surfaces are represented in a Mollweide projection and the center of each one corresponds to 0° of longitude and 90° of co-latitude (equator). Best fits to the simulated light curves together with the O-C residuals are shown. Both cases were simulated with $\beta = 0.2$. The reference level of the unspotted light curve is shown for comparison (dot-dashed line).

Figure 4.6 depicts two examples of the fits together with the configuration of the simulated spots on the stars, and Figure 4.7 shows all the 33 fits performed. In Figure 4.8 the effect of spots on the radius is illustrated, both by plotting the mean values and standard deviations (error bars) of the systematic differences with respect to the input values of the simulations. The sum and the ratio of radii relative to the semimajor axis were used to check for systematic effects since these are the parameters that directly depend on the shape of the eclipses. A clear trend is seen in the case of Distribution 2, where the sum of the radii of the components (i.e., total size of the stars) is systematically overestimated by the fits by 2–6%. For distributions less concentrated to the pole the deviations induced by spots seem to be random. In the case of the ratio of radii, the differences found do not seem to be significant in any of the cases, and especially when considering the dispersion. The same lack of systematic trends is found for other fit parameters such as the inclination, effective temperature ratio, or light ratio.

The parameters related to radial velocity curves, such as semimajor axis, mass ratio and systemic radial velocity, were also inspected for deviations by simulating the corresponding velocity curves. Fits using the WD code were performed by ignor-

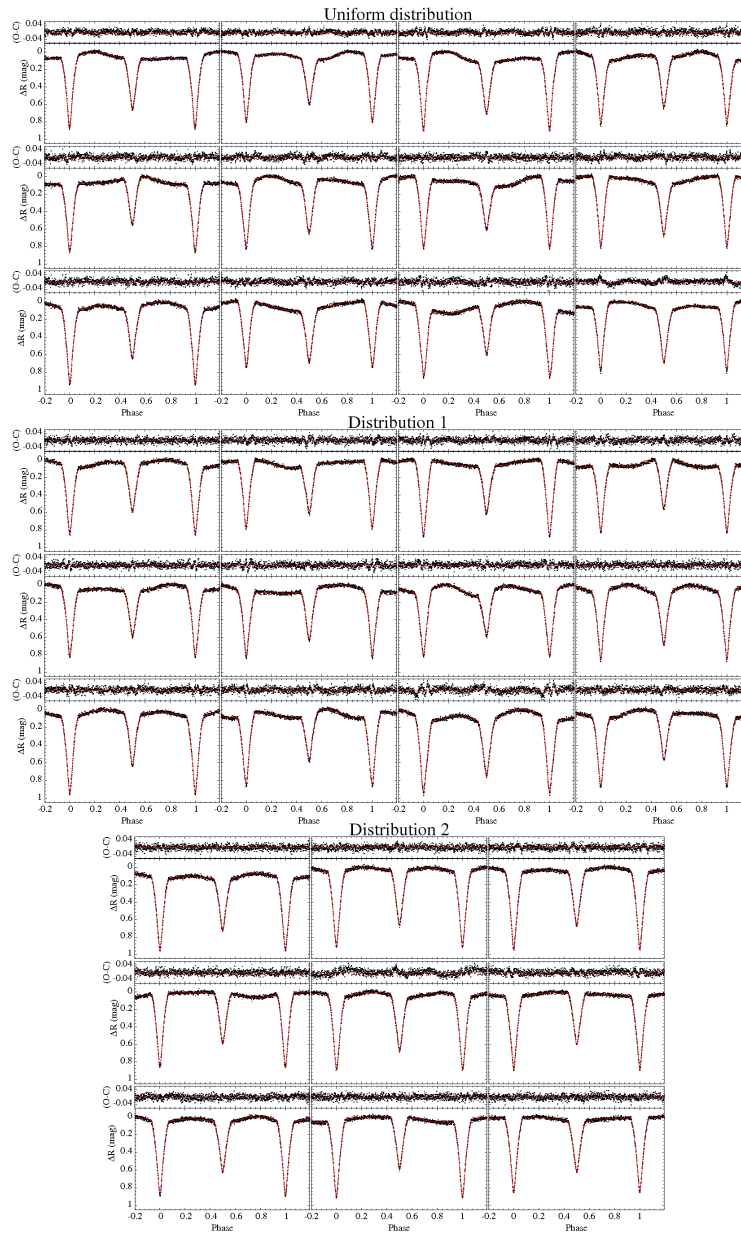


Figure 4.7: Fits to simulated light curves following the procedure explained in the text. Light curves are vertically shifted to be plotted with the same scale. Each block corresponds to a different spot distribution as indicated. Simulations with equal β value are arranged in columns, starting from $\beta = 0.1$ to 0.4 in steps of 0.1 , except for Distribution 2, for which the last column corresponds to $\beta = 0.3$.

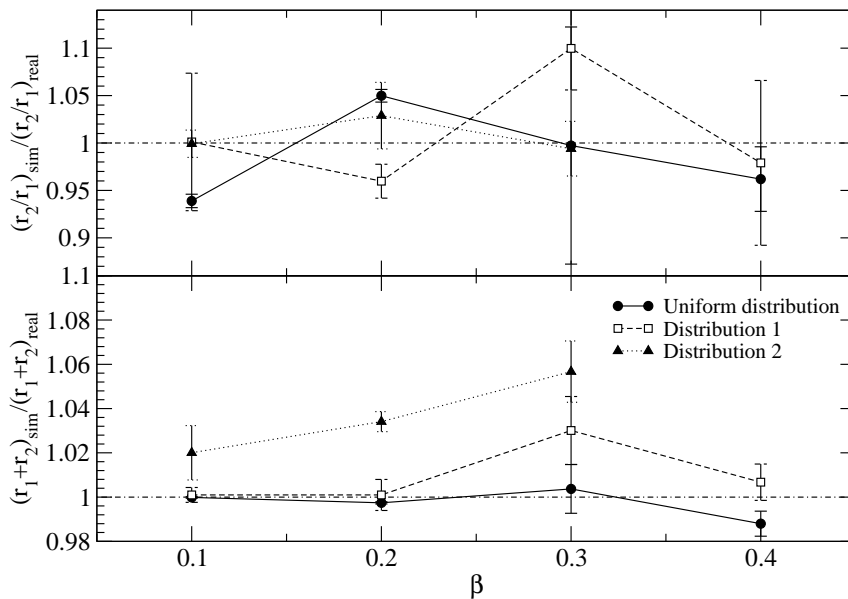


Figure 4.8: Differentials between input parameters to the simulations and those recovered from fits. The ratio and the sum of the radii are shown on the top and bottom panels, respectively, for different distributions: uniform (filled circles), Distribution 1 (open squares) and Distribution 2 (filled triangles). These values are computed as the average of the results of fits on three simulated light curves for each distribution. Standard deviations are shown as error bars.

ing the presence of spots and yielded insignificant differences in the mass ratio and semi-major axis, in all cases below 1% and 0.5%, respectively. As a consequence, the absolute radius derived for each component of the eclipsing binary system is not biased because of the effect of spots on the semi-major axis, which ultimately defines the scale of the system.

The systematically larger radii found from the distributions with polar spots have a relatively straightforward geometric interpretation. A projected star that has a polar cap loses its circular symmetry and its isophotes become elongated. This causes the eclipses to widen and the WD code, which assumes a Roche geometry (i.e., nearly spherical stars for these well-separated systems) finds a best fit with a larger stellar radius. In the case of spots more uniformly distributed in latitude, eclipses are not significantly affected, thus, systematic deviations appear more random. This was tested by assuming systems with pure polar caps (i.e., circular and symmetric dark spots covering both poles) and carrying out fits without considering the presence of spots (since no modulations are seen). The results confirm the existence of the systematic effect on the stellar radii found in the simulations with Distribution 2.

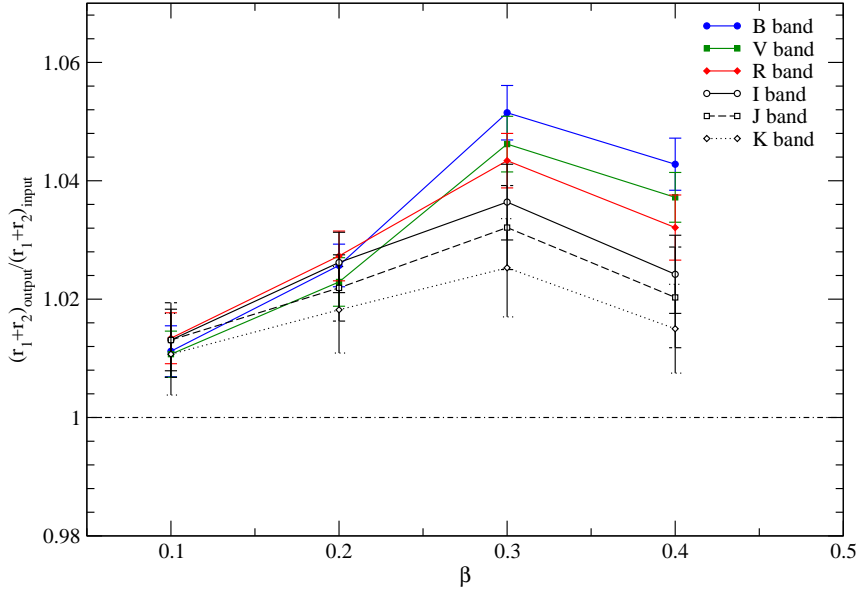


Figure 4.9: Differentials between input parameters to the simulations and those recovered from fits for a case such as GU Boo with polar caps. The ratio and the sum of the radii are shown on the top and bottom panels, respectively, for different filter bands.

Also, because of the much faster fits, several input parameters (corresponding to the systems IM Vir, GU Boo, YY Gem, CU Cnc and CM Dra) were also tested, yielding comparable results, thus confirming the systematic effect on radius also for different values of relevant binary parameters such as inclination, relative radius and temperature ratio. These simulations were also used to test the influence of the photometric band by producing light curves in the *BVRIJK* filters. Figure 4.9 shows that the systematic effect on the radius is expectedly smaller in the near-IR bands because the spot contrast is lower. The radius differences range from $\sim 3.5\%$ in *B* to $\sim 1.2\%$ in *K*. The simultaneous fit of several bands still yields systematic radius differences, corresponding to some average of those resulting from fits to the individual filter light curves.

The outcome of this battery of tests is that the presence of starspots on the stellar surface could bias the determination of stellar radii. This is the case when spots are concentrated towards the poles. Doppler tomography imaging has revealed a preeminence of polar spots on rapidly rotating low-mass stars, such as AG Dor, AB Dor, LO Peg (see Strassmeier 2009, for a review). YY Gem is the only DDLEB system from the sample with published Doppler images (Hatzes 1995), although no indication of a polar cap was found. However, polar spots are difficult to detect with Doppler tomography for near edge-on inclinations, such as the case of YY Gem.

Spectropolarimetric analyses of low-mass stars showing intense poloidal magnetic fields (see Donati & Landstreet 2009, for a review) may provide further evidence of polar spots. If polar caps are present on low-mass DDLEBs, these could be responsible for up to $\sim 6\%$ (if $\beta = 0.3$) of the radius discrepancy between models and observations. Thus, stellar models should be compared with observed values corrected from the systematic effect due to polar spots.

4.4 Modelling active stars

As mentioned in Section 4.1, Chabrier et al. (2007) introduced activity effects in low-mass stellar models by considering two parameters: the spot blocking factor (β) and the modification of the mixing length parameter (α). The study of Chabrier et al. (2007) shows that the effects of the β and α parameters are degenerate, i.e., the properties of any given system can be reproduced by modifying any of the two or both, although for completely convective stars, the effect of reducing the mixing length parameter is very small.

CM Dra offers the possibility of discerning between the effects of activity on the convective efficiency (parameterized by α) and on surface spots (parameterized by β). This is because the components of this system should be fully convective and their structure almost independent of the mixing length parameter α . Thus, this system was used to find the β value that yields the best fit to the properties of the components of CM Dra. We compared the theoretical $M - R$ relationships, interpolating between models with different β . To do so, the presence of polar spots on the components was assumed and theoretical $M - R$ relationships were compared by interpolating between models with different β values (kindly provided by J. Gallardo). Different negative corrections to the radii of the components were used depending on the value of β and in consistency with the simulations in Figure 4.8. An iterative process was employed until reaching agreement between the resulting β value and the radius correction from light curve systematics. After iterating, the best model reproducing both components of CM Dra was found to be $\beta = 0.17 \pm 0.03$ when the radii of the stars were downwards corrected by $\sim 3\%$. If spots are $\sim 15\%$ cooler than the photosphere, the resulting β translates into $(36 \pm 6)\%$ of the star surface covered by spots, a value that is in agreement with findings from Doppler imaging for other systems such as HK Aqr (Barnes & Collier Cameron 2001). Note, however, that spot coverages from Doppler tomography represent a lower limit because of the limited sensitivity of the technique to small-sized spots or low contrast temperatures.

Abundant X-ray observations have revealed a clear relation between magnetic activity and rotation, indicating that rapidly rotating stars are more active than

slower rotators up to a certain limit where saturation is reached. Pizzolato et al. (2003) showed that M-dwarfs with rotation periods below ~ 10 days show saturation of their X-ray emission, therefore we could assume that binaries in the sample are all in this regime of saturated coronal activity. The physical mechanism of saturation is not well understood yet, but one of the feasible explanations could be that saturation is reached when the entire stellar corona is full of active regions. This may imply that the β parameter is similar for stars that are in the saturated regime.

At this point, two assumptions are made in order to proceed with the analysis:

1. That spots on active DDLEBs are mostly polar.
2. That saturated systems have similar spot coverages (i.e., that β is roughly independent of mass for very active systems).

The top panel of Figure 4.10 shows a comparison of mass and radius observations with models assuming different β values. The radii of the DDLEB systems shown in the figure were corrected considering two effects. First, a 3% systematic difference resulting from the light curve analysis. Second, an age effect on the stellar radii to put all systems at a normalized age of 1 Gyr (ages in Table 4.1, except for NGC2204-S892 where no age is available and no correction was made) using the models of Baraffe et al. (1998). The effect of metallicity on radius was not considered for the case of V818 Tau B and IM Vir B because its effect is negligible or because of the poorly constrained value of metallicity in the case of CM Dra (see Section 2.2.5). The evolutionary radius offsets are always well below the 1% level. This allowed us to plot Figure 4.10 and compare all DDLEBs with a theoretical model with the same age.

To serve as a reference, if the polar spot assumption is relaxed, i.e., the systematic effect of polar spots on light curves is not corrected, the best model reproducing CM Dra gives $\beta = 0.37 \pm 0.04$, which means more than 75% of the surface of each component covered by spots. This seems to be a rather high value of spot coverage when compared with the results of Doppler imaging. Following the same procedure applied above for CM Dra, the overall sample of DDLEB systems is reproduced within 1σ of their error bars with $\beta = 0.20 \pm 0.04$, i.e., $(42 \pm 8)\%$ of spot coverage. On the other hand, if the saturation hypothesis is not considered and it is assumed that each system could be reproduced by different β factors, in systems such as YY Gem or GU Boo over half of the surface must be spotted. Note that the spot coverage estimates depend on the spot contrast, which is set to ~ 500 K in this work.

Some remaining radius differences are still apparent in Figure 4.10 when considering a β value of 0.17. Systems such as YY Gem or GU Boo have observed radii well over 1σ of the model predictions. It is interesting to note that these are the

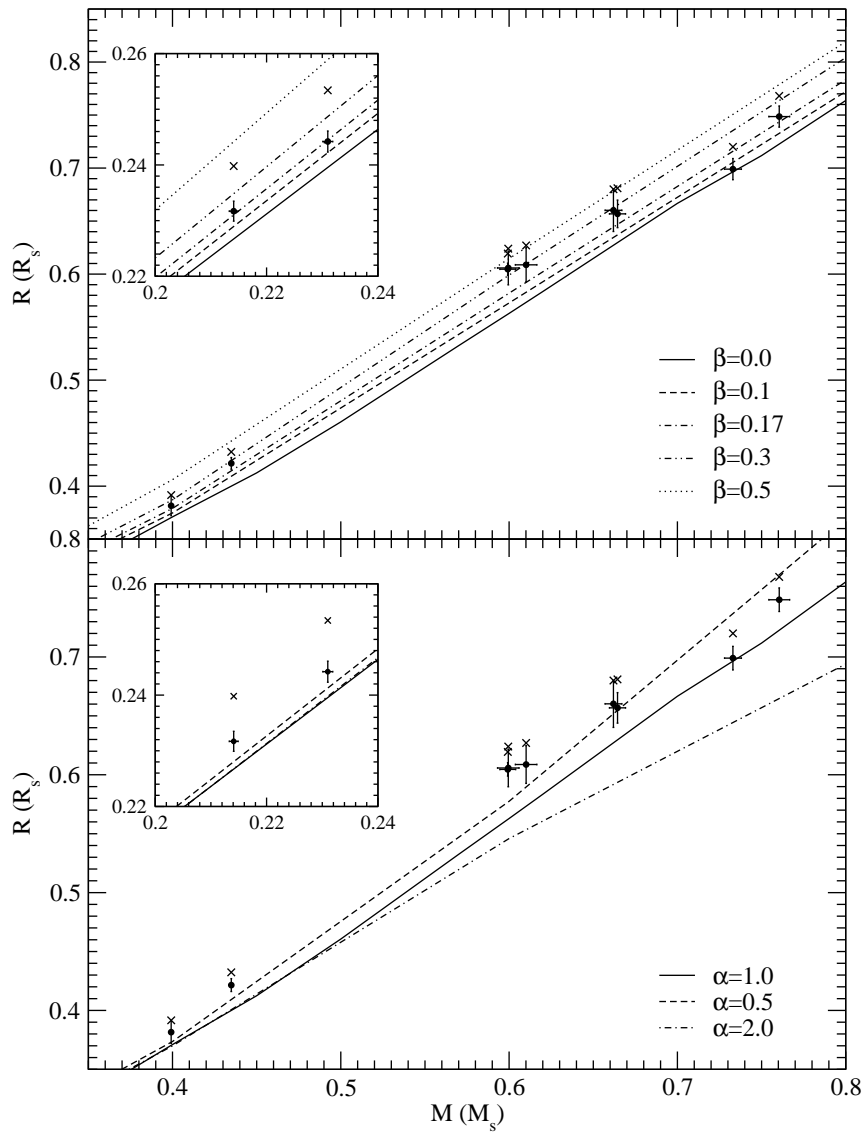


Figure 4.10: Comparison between $M - R$ relationships from models and observations for different β values and $\alpha = 1$ (top), and for different α values and $\beta = 0$ (bottom). Crosses indicate the measured radius of the DDLEB components reported in Table 4.1 and circles represent the values corrected for the 3% systematic factor described in text and further normalized to an age of 1 Gyr. The insets display the case of CM Dra.

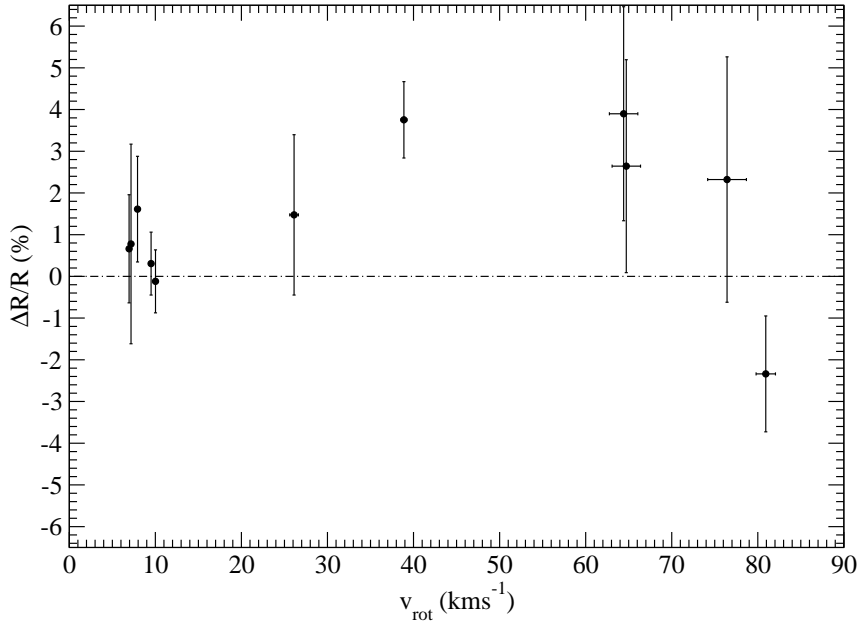


Figure 4.11: Residual discrepancy between observations and the model with $\beta=0.17$ that best fits the case of CM Dra, which is not affected by variations of the mixing length parameter α .

systems with the fastest rotational velocity and perhaps this could be an indication of additional effects of rotation and/or magnetic activity not accounted for in the β analysis. The bottom panel of Figure 4.10 shows that for the more massive M-type DDLEBs ($> 0.6 M_{\odot}$) the additional differences could be explained by reducing the mixing length parameter α . Figure 4.11 depicts the differences between the $\beta = 0.17$ model and observations (after correction for polar spots and normalized to 1 Gyr) as a function of the rotational velocity of each star (computed assuming synchronization). Although not significant, a general trend of increasing differences for increasing rotational velocities seems to be present. The exception is NGC2204-S892 (two rightmost points on the plot), which is the shortest period binary. But note that no determination of the age and metallicity of this DDLEB system is available and this could be falsifying the analysis. The tentative trend may indicate that, while the spot effect (via the β parameter) is a clear contributor to explaining the differences between observation and theory, the loss of efficiency of convective energy transport (related with magnetic fields and thus possibly with rotation rate) may also be at play, explaining up to 4% of the radius difference.

As stated in Section 4.2, absolute effective temperatures of DDLEB components were not used to constrain model parameters because they are not determined in-

independently of calibrations as masses and radii. Nevertheless the consistency of the spot scenario also with temperatures was checked. The panels of Figure 4.12 show the comparison between models and observations in the $M - T_{\text{eff}}$ plane for different α and β values. The temperatures represented on these plots have been also normalized to an age of 1 Gyr using the models of Baraffe et al. (1998) although differences amount for less than 10 K in all cases. The model with $\beta = 0.17$ also reproduces the $M - T_{\text{eff}}$ relationship of DDLEBs within the errors, with the exceptions of IM Vir, which metallicity may have an effect on the temperatures (the Lyon stellar models predict a temperature difference of about -300 K between the model with solar metallicity and with $[M/H] = -0.28$), and CU Cnc, whose temperatures may be affected by a circumstellar dust disk (Ribas 2003). These figures also show that both models with lower α and the model with $\beta = 0.17$ reproduce all systems but CM Dra, due to the negligible effect of mixing length on completely convective stars. Thus, the conclusions from the $M - R$ analysis are also consistent with the effective temperature comparison.

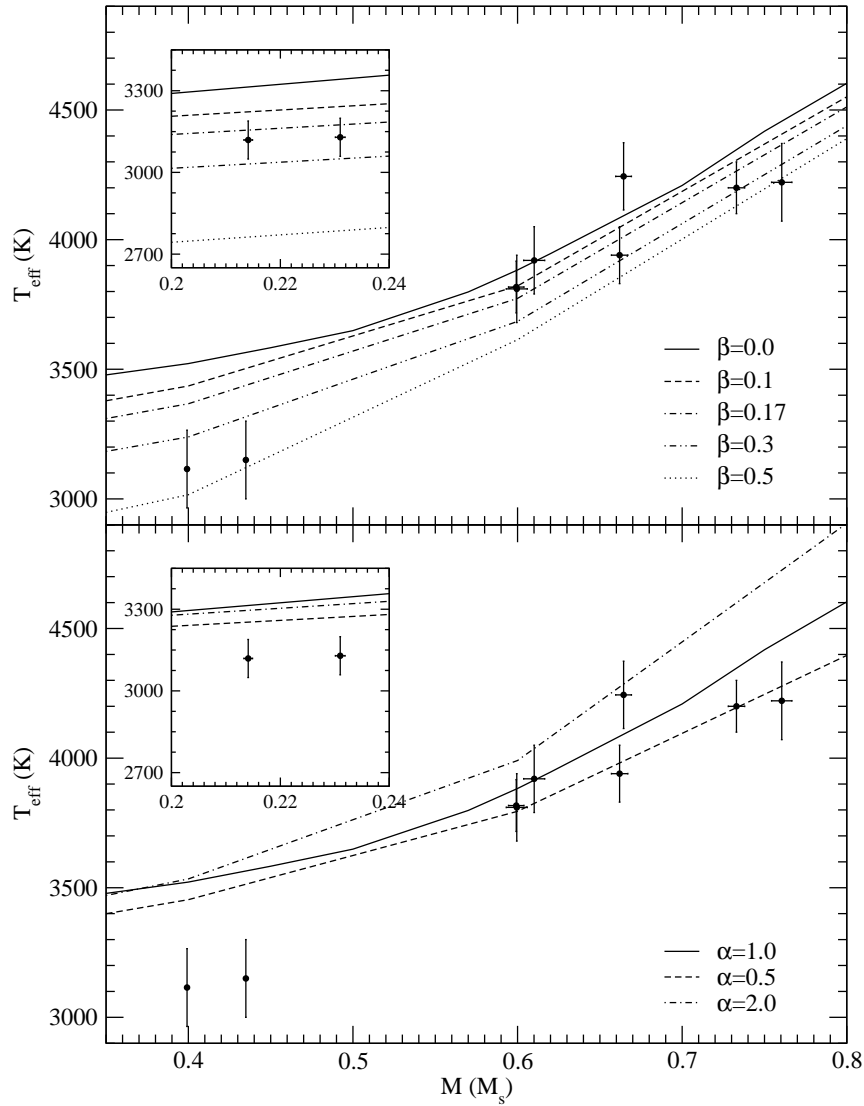


Figure 4.12: Comparison between $M - T_{\text{eff}}$ relationships from models and observations for different β values and $\alpha = 1$ (top), and for different α values and $\beta = 0$ (bottom). Circles are the values of effective temperatures of the DDLEBs in Table 4.1 normalized to an age of 1 Gyr. Bottom: $M - T_{\text{eff}}$ relationship. The insets display the case of CM Dra.

Chapter 5

Conclusions

5.1 Summary and results

The main goal of this work was to understand and to propose an scenario to explain the radius and effective temperature differences found between stellar structure models and observations of low-mass stars ($M < 1 M_{\odot}$) in eclipsing binaries. These differences have been ascribed to the effects of metallicities, opacities or the magnetic activity on these stars but the results of this work reveal that the magnetic activity is the most reasonable explanation, and the inclusion of its effect on the stellar models can explain the fundamental properties of the best-known DDLEB systems. Following, the observational and theoretical work done here and the main conclusions from the results are summarized.

From the observational point of view, the fundamental properties of the stars in two relevant binary systems were determined, thus adding two new systems to the sample of 15 well known DDLEBs with at least one component below $1 M_{\odot}$ (only 6 with components below $0.8 M_{\odot}$, see Torres et al. 2010, for a review). Masses and radii of the components of CM Dra and IM Vir, were obtained with accuracies below the 2% level.

- **CM Dra:** The analysis of the vast amount of photometric and spectroscopic data of this system with improved methods with respect to those used by Lacy (1977) yielded the masses and radii of its components with uncertainties of only $\sim 0.5\%$, $M_1 = 0.2310 \pm 0.0009 M_{\odot}$, $M_2 = 0.2141 \pm 0.0010 M_{\odot}$, $R_1 = 0.2534 \pm 0.0019 R_{\odot}$ and $R_2 = 0.2396 \pm 0.0015 R_{\odot}$. A special effort was made in this study to account for the effect of the photospheric spots present on the components of this system. A number of tests were performed to investigate possible sources of systematic errors in the orbital and physical parameters and to asses their importance. The absolute effective temperatures were also checked for consistency. The resulting uncertainties of these funda-

mental properties of the components offered the best opportunity to date for carrying out meaningful tests of stellar evolution models for fully convective stars.

Furthermore, the age of CM Dra was also estimated from the cooling time of the white dwarf common proper motion companion and the evolution of its assumed progenitor, thus constraining another relevant property when comparing with stellar models. Unfortunately, the metallicity is not as constrained given the confusing results of Viti et al. (1997, 2002).

Finally, for this system, the large number of minima timings (although with an unfortunate gap of 18 years) clearly showed the presence of apsidal motion. Its value ($\dot{\omega} = (2.3 \pm 1.4) \times 10^{-4} \text{ }^\circ\text{cycle}^{-1}$) is still poorly determined because of observational errors, other errors due to the distortions caused by spots on the system, and the limited time coverage of the data. Moreover, no clear signature of third bodies have been found within the minima timings data. The observational value of the apsidal motion is significantly in disagreement with the theoretically predicted one. This can be indicating the effect of an unseen third body in the system, which could explain as well the small but observable eccentricity of the system. Further measurements over the coming years will greatly help to constrain the precession of the line of apsides and to separate the effect of a third body, if present, more clearly.

- **IM Vir:** The light and radial velocity curves of this binary system were analyzed here for the first time in order to determine the fundamental properties of the components. The masses and radii were determined with accuracies better than 2%, the values being $M_1 = 0.981 \pm 0.012 M_\odot$, $M_2 = 0.6644 \pm 0.0048 M_\odot$, $R_1 = 1.061 \pm 0.016 R_\odot$ and $R_2 = 0.681 \pm 0.013 R_\odot$. The effective temperatures were also constrained and checked for consistency with the results from the curve analysis. The special interest in this system lies in the very different masses of its components, that provide increased discriminating power for testing models of stellar structure and evolution.

Unfortunately, in this case, no clear constraints on the age or the chemical composition of the system was found, although a mildly subsolar metallicity value was indicated both by the analysis of the spectroscopic data used to get the radial velocities and by photometric color calibrations.

When comparing the components of these binary systems with the Lyon stellar structure models (Baraffe et al. 1998) discrepancies in the mass-radius and mass-effective

temperatures in agreement with those reported previously for other DDLEBs (see Ribas 2006a, for a review) were found.

In the case of CM Dra, the radii of the primary and secondary components are 5.0% and 5.2%, respectively, larger than expected from theoretical models while temperatures are 6.4% and 5.9% cooler, thus extending the discrepancies to the mass range of fully convective stars. On the other hand, the luminosities are relatively better determined as found for other systems. Lower metallicity models, as those used by Viti et al. (1997, 2002) for CM Dra, do not reduce these discrepancies but increase them. This suggests to adopt a compromise solar metallicity for CM Dra.

In the case of IM Vir, for which neither metallicity nor the age was reliably known, a different approach was used taking advantage of the large mass difference of its components. No stellar isochrone with the same age and metallicity provided a good fit to both the primary and the secondary components at the same time, showing discrepancies in radius and effective temperatures similar to other DDLEBs. Assuming that luminosities are well predicted by models, observations were matched by a model with 2.4 ± 0.5 Gyr and $[M/H] = -0.28 \pm 0.10$, while reproducing radii 3.7% and 7.5% smaller and effective temperatures 2% and 3.5% hotter than the observations. Interestingly, this metallicity value is close to that estimated from spectroscopy or photometric calibrations.

Both of these binary systems are known to host magnetically active stars, as the photometric variability due to spots and the saturated X-ray emission indicate, thus reinforcing the hypothesis that the activity is the responsible of the discrepancies between models and observations. Besides, the analysis of the PMSU sample of nearby isolated stars, showed similar discrepancies between single active stars and their inactive counterparts with the same luminosities (i.e. mass), adding further evidence to the magnetic activity hypothesis.

Finally, the sample of best known DDLEBs systems with main-sequence components were used to test the theoretical scenario suggested by Chabrier et al. (2007). These authors introduce the effects of rotation and magnetic activity on models both by inhibiting the convective motions, that is mimicked by reducing the mixing length parameter (α), and by assuming that photospheric spots block part of the outgoing flux from the stellar interior, that is parameterized with the ratio of surface covered by completely dark spots (β).

CM Dra was used as a cornerstone to separate the effects of α and β since the fully convective stars are almost insensitive to changes of the convective efficiency. After evaluating the effect of photospheric spots both on the models and on the light and radial velocity curve analysis of DDLEBs, a rather complex picture is now

emerging since no single effect can account for the full size of the differences. The analysis shown here suggests that the $\sim 5 - 10\%$ radius discrepancy in M-type stars is explained by combining three factors:

1. A systematic of the stellar radius derived from DDLEB light curve analyses caused by the presence of polar spots with the subsequent loss of circular symmetry. This amounts to about 3% of the radius difference.
2. An increase of the stellar radii to compensate for the loss of radiative efficiency because of starspots that is modelled with $\beta \sim 0.17$ and explains 2% of the radius difference.
3. An increase of the radius caused by the lower convective efficiency in fast rotators with supposedly strong magnetic fields, reproduced by models by changing α and amounting to 0–4% of the radius difference.

The results of this analysis are based on two main hypothesis:

1. That all of these active DDLEB components have spots that preferentially occupy locations close to the pole.
2. That all DDLEB components have similar surface spottedness.

The former hypothesis is in line with the results of Doppler imaging and with theoretical analyses of the emergency of the magnetic flux tubes on fast rotating stars, while the later is indicated by the saturated activity regime of these DDLEB systems. The first hypothesis relaxes the classical discrepancy with models to a lower 2 – 7% while the second ensures that β will roughly be the same for the strongly active stars, and gives CM Dra its relevant role in this analysis.

This scenario also reproduces the $M - T_{\text{eff}}$ distribution of DDLEBs although effective temperatures are not as fundamentally determined as radii. The predicted spot coverages of about $\sim 35\%$ ($\beta \sim 0.17$ if the temperature contrast between the photosphere and the spots is 0.85) and the simulated light curves are found to reproduce the modulation amplitudes in the real light curves of DDLEB systems. Also the surface coverage is found to be compatible with results from Doppler tomography of active stars.

Therefore, the results of the present work consolidate the scenario that magnetic activity is a relevant parameter to take into account when studying low-mass stars since their stellar structure can be severely affected either due to the starspots, the inhibition of convection, or both.

5.2 Future prospects

Further evidence to confirm the main results of this work can come from different sources and are under study.

Although the number of eclipsing binaries with low-mass components is increasing there is still a scarcity of them, especially with well-known fundamental properties. The determination of accurate masses and radii from DDLEBs would help to confirm the correlations (if existing) between the radius differences and parameters such as the rotation of the stars, and to better constrain the activity parameters of the models. Particularly interesting are systems in:

- **Open clusters or kinematic groups.** The membership of a binary system to an open cluster or a kinematic group allows to assume that its age and metallicity are the same as that of the ensemble. Consequently, two of the fundamental properties that are more difficult to obtain turn out to be constrained.
- **Long period orbits.** These systems would provide strong evidence for the activity hypothesis. The components of DDLEBs with periods over 10 days are not expected to be synchronized, so they may not be as affected by magnetic activity as very close binaries. Their light and radial velocity curves would provide very accurate fundamental properties of inactive stars to be compared both with models and with the sample of active DDLEBs. The increasing accuracy of radius interferometric measurements can also help in this point, although the masses are not as fundamentally determined as for DDLEBs and the radius accuracy depends also on the determination of the distance to the star.

An effort to increase the sample of low-mass DDLEBs was done through the ROTES project (see Appendix C and Ribas et al. 2006, 2007), especially devoted to the discovery of DDLEBs in open clusters. Unfortunately, no system with low-mass components has been clearly identified yet. However, with the increasing interest in exoplanets it is expected that a significant number of DDLEBs (notably some with long periods) will come from missions such as *COROT* and *Kepler*. In this sense, data coming from *COROT* are already being analyzed to find low-mass DDLEB candidates (see also Appendix C).

New precise photometric techniques can also help to understand the effect of activity on stars. They can be used to map the surface of the spots during transits, and thus, to better estimate the configuration of the spots on the components.

Finally, the apsidal motion analysis of CM Dra opened a new possibility of stellar models testing by comparing the theoretical predictions and the observational values of the internal structure constants. Although the value found here for CM Dra is still poorly determined, new minima timings in the coming years would unveil the presence of a third body in the system or clarify the best scenario to both explain the remaining eccentricity in the system and the apsidal motion.

Bibliography

- Akerlof C. W., Kehoe R. L., McKay T. A., Rykoff E. S., Smith D. A., Casperson D. E., McGowan K. E., Vestrand W. T., Wozniak P. R., Wren J. A., Ashley M. C. B., Phillips M. A., Marshall S. L., Epps H. W., Schier J. A., 2003, *PASP*, 115, 132
- Allard F., Hauschildt P. H., 1995, *ApJ*, 445, 433
- Allard F., Hauschildt P. H., Alexander D. R., Starrfield S., 1997, *ARA&A*, 35, 137
- Alonso A., Arribas S., Martinez-Roger C., 1994, *A&ASS*, 107, 365
- Amado P. J., Byrne P. B., 1997, *A&A*, 319, 967
- Andersen J., 1991, *A&ARv*, 3, 91
- Bahcall J. N., Basu S., Pinsonneault M., Serenelli A. M., 2005, *ApJ*, 618, 1049
- Bahcall J. N., Serenelli A. M., Pinsonneault M., 2004, *ApJ*, 614, 464
- Baraffe I., Chabrier G., Allard F., Hauschildt P. H., 1997, *A&A*, 327, 1054
- , 1998, *A&A*, 337, 403
- Barnes J. R., Collier Cameron A., 2001, *MNRAS*, 326, 950
- Bayless A. J., Orosz J. A., 2006, *ApJ*, 651, 1155
- Beatty T. G., Fernández J. M., Latham D. W., Bakos G. Á., Kovács G., Noyes R. W., Stefanik R. P., Torres G., Everett M. E., Hergenrother C. W., 2007, *ApJ*, 663, 573
- Bentley S. J., Smalley B., Maxted P. F. L., Hellier C., Wilson D. M., Anderson D. R., Collier Cameron A., Gillon M., Hebb L., Pollacco D. L., Queloz D., Triaud A. H. M. J., West R. G., 2009, *A&A*, 508, 391
- Berger D. H., Gies D. R., McAlister H. A., Brummelaar T. A. t., Henry T. J., Sturmann J., Sturmann L., Turner N. H., Ridgway S. T., Aufdenberg J. P., Mérand A., 2006, *ApJ*, 644, 475

- Bergeron P., Leggett S. K., Ruiz M. T., 2001, *ApJS*, 133, 413
- Bessell M. S., 1991, *AJ*, 101, 662
- Bessell M. S., Brett J. M., 1988, *PASP*, 100, 1134
- Bessell M. S., Castelli F., Plez B., 1998, *A&A*, 333, 231
- Blake C. H., Torres G., Bloom J. S., Gaudi B. S., 2008, *ApJ*, 684, 635
- Bochanski J. J., Hawley S. L., Reid I. N., Covey K. R., West A. A., Tinney C. G., Gizis J. E., 2005, *AJ*, 130, 1871
- Bochanski J. J., West A. A., Hawley S. L., Covey K. R., 2007, *AJ*, 133, 531
- Bonfils X., Delfosse X., Udry S., Santos N. C., Forveille T., Ségransan D., 2005, *A&A*, 442, 635
- Çakırlı Ö., Ibanoglu C., 2010, *MNRAS*, 401, 1141
- Çakırlı Ö., Ibanoglu C., Güngör C., 2009, *New Astronomy*, 14, 496
- Carpenter J. M., 2001, *AJ*, 121, 2851
- Carroll B. W., Ostlie D. A., 1996, *An introduction to modern astrophysics*. Reading, MA: Addison-Wesley
- Casagrande L., Flynn C., Bessell M., 2008, *MNRAS*, 389, 585
- Casagrande L., Portinari L., Flynn C., 2006, *MNRAS*, 373, 13
- Castelli F., Kurucz R. L., 2004, *ArXiv Astrophysics e-prints*
- Catalán S., Isern J., García-Berro E., Ribas I., 2008, *MNRAS*, 387, 1693
- Chabrier G., Baraffe I., 1995, *ApJ*, 451, L29
- , 1997, *A&A*, 327, 1039
- Chabrier G., Gallardo J., Baraffe I., 2007, *A&A*, 472, L17
- Claret A., 2000a, *A&A*, 363, 1081
- , 2000b, *A&A*, 359, 289
- , 2004, *A&A*, 428, 1001
- Claret A., Giménez A., 1993, *A&A*, 277, 487

- Cox A. N., 2000, *Allen's astrophysical quantities*. *Allen's astrophysical quantities*, 4th ed. Publisher: New York: AIP Press; Springer, 2000. Edited by Arthur N. Cox. ISBN: 0387987460
- Cram L. E., Mullan D. J., 1979, *ApJ*, 234, 579
- Creevey O. L., Benedict G. F., Brown T. M., Alonso R., Cargile P., Mandushev G., Charbonneau D., McArthur B. E., Cochran W., O'Donovan F. T., Jiménez-Reyes S. J., Belmonte J. A., Kolinski D., 2005, *ApJ*, 625, L127
- Cutri R. M., Skrutskie M. F., van Dyk S., Beichman C. A., Carpenter J. M., Chester T., Cambresy L., Evans T., Fowler J., Gizis J., Howard E., Huchra J., Jarrett T., Kopan E. L., Kirkpatrick J. D., Light R. M., Marsh K. A., McCallon H., Schneider S., Stiening R., Sykes M., Weinberg M., Wheaton W. A., Wheelock S., Zacarias N., 2003, *2MASS All Sky Catalog of point sources*, Cutri, R. M., Skrutskie, M. F., van Dyk, S., Beichman, C. A., Carpenter, J. M., Chester, T., Cambresy, L., Evans, T., Fowler, J., Gizis, J., Howard, E., Huchra, J., Jarrett, T., Kopan, E. L., Kirkpatrick, J. D., Light, R. M., Marsh, K. A., McCallon, H., Schneider, S., Stiening, R., Sykes, M., Weinberg, M., Wheaton, W. A., Wheelock, S., & Zacarias, N., ed.
- Dall T. H., Foellmi C., Pritchard J., Lo Curto G., Allende Prieto C., Bruntt H., Amado P. J., Arentoft T., Baes M., Depagne E., Fernandez M., Ivanov V., Koesterke L., Monaco L., O'Brien K., Sarro L. M., Saviane I., Scharwächter J., Schmidtbreick L., Schütz O., Seifahrt A., Selman F., Stefanon M., Sterzik M., 2007, *A&A*, 470, 1201
- de Jager C., Nieuwenhuijzen H., 1987, *A&A*, 177, 217
- Deeg H. J., Doyle L. R., Kozhevnikov V. P., Blue J. E., Martín E. L., Schneider J., 2000, *A&A*, 358, L5
- Deeg H. J., Ocaña B., Kozhevnikov V. P., Charbonneau D., O'Donovan F. T., Doyle L. R., 2008, *A&A*, 480, 563
- Demarque P., Woo J., Kim Y., Yi S. K., 2004, *ApJS*, 155, 667
- Demory B., Ségransan D., Forveille T., Queloz D., Beuzit J., Delfosse X., di Folco E., Kervella P., Le Bouquin J., Perrier C., Benisty M., Duvert G., Hofmann K., Lopez B., Petrov R., 2009, *A&A*, 505, 205
- Devor J., Charbonneau D., Torres G., Blake C. H., White R. J., Rabus M., O'Donovan F. T., Mandushev G., Bakos G. Á., Fűrész G., Szentgyorgyi A., 2008, *ApJ*, 687, 1253
- Donati J., Landstreet J. D., 2009, *ARA&A*, 47, 333

- Dunham E. W., Mandushev G. I., Taylor B. W., Oetiker B., 2004, *PASP*, 116, 1072
- Dvorak S. W., 2005, *Information Bulletin on Variable Stars*, 5603, 1
- Eggen O. J., Sandage A., 1967, *ApJ*, 148, 911
- Etzel P. B., 1981, in *Photometric and Spectroscopic Binary Systems*, E. B. Carling & Z. Kopal, ed., p. 111
- Flower P. J., 1996, *ApJ*, 469, 355
- Giménez A., 1985, *ApJ*, 297, 405
- Giménez A., Bastero M., 1995, *Ap&SS*, 226, 99
- Girardi L., Bressan A., Bertelli G., Chiosi C., 2000, *A&ASS*, 141, 371
- Gizis J. E., Reid I. N., Hawley S. L., 2002, *AJ*, 123, 3356
- González Hernández J. I., Bonifacio P., 2009, *A&A*, 497, 497
- Granzer T., Schüssler M., Caligari P., Strassmeier K. G., 2000, *A&A*, 355, 1087
- Griffin R. E. M., David M., Verschueren W., 2000, *A&ASS*, 147, 299
- Guinan E. F., Ribas I., 2001, *ApJ*, 546, L43
- Hargis J. R., Bradstreet D. H., Lake J. S., Jewett F. D., Wilkinson G. R., Blair J. M., Guinan E. F., Ribas I., McCook G. P., 2000, in *Bulletin of the American Astronomical Society*, Vol. 32, *Bulletin of the American Astronomical Society*, p. 1480
- Hartman J. D., Bakos G. Á., Noyes R. W., Sipöcz B., Kovács G., Mazeh T., Shporer A., Pál A., 2009, *ArXiv e-prints*
- Hatzes A. P., 1995, in *IAU Symposium*, Vol. 176, *IAU Symposium*, p. 90
- Hauschildt P. H., Allard F., Baron E., 1999, *ApJ*, 512, 377
- Hawley S. L., Gizis J. E., Reid I. N., 1996, *AJ*, 112, 2799
- Hebb L., Wyse R. F. G., Gilmore G., 2004, *AJ*, 128, 2881
- Hebb L., Wyse R. F. G., Gilmore G., Holtzman J., 2006, *AJ*, 131, 555
- Helfand D. J., Caillault J., 1982, *ApJ*, 253, 760
- Høg E., Fabricius C., Makarov V. V., Urban S., Corbin T., Wycoff G., Bastian U., Schwekendiek P., Wicenec A., 2000, *A&A*, 355, L27

- Holmberg J., Nordström B., Andersen J., 2007, *A&A*, 475, 519
- Irwin J., Charbonneau D., Berta Z. K., Quinn S. N., Latham D. W., Torres G., Blake C. H., Burke C. J., Esquerdo G. A., Fürész G., Mink D. J., Nutzman P., Szentgyorgyi A. H., Calkins M. L., Falco E. E., Bloom J. S., Starr D. L., 2009, *ApJ*, 701, 1436
- Irwin J. B., 1959, *AJ*, 64, 149
- Jeffers S. V., Donati J., Collier Cameron A., 2007, *MNRAS*, 375, 567
- Johnson H. L., 1966, *ARA&A*, 4, 193
- Johnson J. A., Apps K., 2009, *ApJ*, 699, 933
- Joy A. H., Abt H. A., 1974, *ApJS*, 28, 1
- Kippenhahn R., Weigert A., 1990, *Stellar Structure and Evolution. Stellar Structure and Evolution*, XVI, 468 pp. 192 figs.. Springer-Verlag Berlin Heidelberg New York. Also *Astronomy and Astrophysics Library*
- Kopal Z., 1978, *Dynamics of Close Binary Stars*. Reidel Publishing Company
- Kozhevnikova A. V., Kozhevnikov V. P., Zakharova P. E., Polushina T. S., Svechnikov M. A., 2004, *Astronomy Reports*, 48, 751
- Kuiper G. P., 1942, *ApJ*, 95, 201
- Lacy C. H., 1977, *ApJ*, 218, 444
- Lacy C. H., Moffett T. J., Evans D. S., 1976, *ApJS*, 30, 85
- Latham D. W., 1985, in *Stellar Radial Velocities*, p. 21
- , 1992, in *Astronomical Society of the Pacific Conference Series*, Vol. 32, IAU Colloq. 135: Complementary Approaches to Double and Multiple Star Research, H. A. McAlister & W. I. Hartkopf, ed., p. 110
- Leggett S. K., Allard F., Berriman G., Dahn C. C., Hauschildt P. H., 1996, *ApJS*, 104, 117
- Liu X., Huang H., Zhu W., 1996, *Ap&SS*, 246, 39
- López-Morales M., 2007, *ApJ*, 660, 732
- López-Morales M., Orosz J. A., Shaw J. S., Havelka L., Arevalo M. J., McIntyre T., Lazaro C., 2006, *ApJ*, submitted, (astro-ph: 0707.1792)
- López-Morales M., Ribas I., 2005, *ApJ*, 631, 1120

- López-Morales M., Shaw J. S., 2007, in *Astronomical Society of the Pacific Conference Series*, Vol. 362, *The Seventh Pacific Rim Conference on Stellar Astrophysics*, Y. W. Kang, H.-W. Lee, K.-C. Leung, & K.-S. Cheng, ed., p. 26
- López-Santiago J., Montes D., Crespo-Chacón I., Fernández-Figueroa M. J., 2006, *ApJ*, 643, 1160
- Maceroni C., Montalbán J., 2004, *A&A*, 426, 577
- Mandushev G., O'Donovan F. T., Charbonneau D., Torres G., Latham D. W., Bakos G. Á., Dunham E. W., Sozzetti A., Fernández J. M., Esquerdo G. A., Everett M. E., Brown T. M., Rabus M., Belmonte J. A., Hillenbrand L. A., 2007, *ApJ*, 667, L195
- Mandushev G., Torres G., Latham D. W., Charbonneau D., Alonso R., White R. J., Stefanik R. P., Dunham E. W., Brown T. M., O'Donovan F. T., 2005, *ApJ*, 621, 1061
- Manfroid J., Sterken C., Bruch A., Burger M., de Groot M., Duerbeck H. W., Duemmler R., Figer A., Hageman T., Hensberge H., Jorissen A., Madejsky R., Mandel H., Ott H., Reitermann A., Schulte-Ladbeck R. E., Stahl O., Steenman H., Vander Linden D., Zickgraf F., 1991, *A&ASS*, 87, 481
- Marschall L. A., Nations H., Witman K., 1988, in *Bulletin of the American Astronomical Society*, Vol. 20, *Bulletin of the American Astronomical Society*, p. 994
- Marschall L. A., Stefanik R., Nations H., Karshner G., 1989, in *Bulletin of the American Astronomical Society*, Vol. 21, *Bulletin of the American Astronomical Society*, p. 1083
- Masana E., Jordi C., Ribas I., 2006, *A&A*, 450, 735
- Maxted P. F. L., Marsh T. R., Morales-Rueda L., Barstow M. A., Dobbie P. D., Schreiber M. R., Dhillon V. S., Brinkworth C. S., 2004, *MNRAS*, 355, 1143
- Maxted P. F. L., O'Donoghue D., Morales-Rueda L., Napiwotzki R., Smalley B., 2007, *MNRAS*, 376, 919
- Mazeh T., 2008, in *EAS Publications Series*, Vol. 29, *EAS Publications Series*, M.-J. Goupil & J.-P. Zahn, ed., p. 1
- Metcalf T. S., Mathieu R. D., Latham D. W., Torres G., 1996, *ApJ*, 456, 356
- Monet D., Bird A., Canzian B., Dahn C., Guetter H., Harris H., Henden A., Levine S., Luginbuhl C., Monet A., Rhodes A., Riepe B., Sell S., Stone R., Vrba F., Walker R., 1998, *VizieR Online Data Catalog*, 1252

- Montes D., López-Santiago J., Gálvez M. C., Fernández-Figueroa M. J., De Castro E., Cornide M., 2001, *MNRAS*, 328, 45
- Morale F., Micela G., Favata F., Sciortino S., 1996, *A&ASS*, 119, 403
- Morales J. C., Gallardo J., Ribas I., Jordi C., Baraffe I., Chabrier G., 2010, *ApJ*
- Morales J. C., Ribas I., Jordi C., 2008a, *A&A*, 478, 507
- , 2008b, *Memorie della Societa Astronomica Italiana*, 79, 735
- Morales J. C., Ribas I., Jordi C., Torres G., Gallardo J., Guinan E. F., Charbonneau D., Wolf M., Latham D. W., Anglada-Escudé G., Bradstreet D. H., Everett M. E., O'Donovan F. T., Mandushev G., Mathieu R. D., 2009a, *ApJ*, 691, 1400
- Morales J. C., Ribas I., Jordi C., Torres G., Guinan E. F., 2007a, in *IAU Symposium*, Vol. 240, *IAU Symposium*, p. 326
- Morales J. C., Ribas I., Jordi C., Torres G., Guinan E. F., Charbonneau D., 2007b, in *Highlights of Spanish Astrophysics IV*, Figueras F., Girart J. M., Hernanz M., Jordi C., eds., *SEA Conference*, 2006
- Morales J. C., Torres G., Marschall L. A., Brehm W., 2009b, *ApJ*, 707, 671
- Nelson T. E., Caton D. B., 2007, *Information Bulletin on Variable Stars*, 5789, 1
- Nordström B., Mayor M., Andersen J., Holmberg J., Pont F., Jørgensen B. R., Olsen E. H., Udry S., Mowlavi N., 2004, *A&A*, 418, 989
- O'Brien M. S., Bond H. E., Sion E. M., 2001, *ApJ*, 563, 971
- O'Donoghue D., Koen C., Kilkeny D., Stobie R. S., Koester D., Bessell M. S., Hambly N., MacGillivray H., 2003, *MNRAS*, 345, 506
- O'Donovan F. T., Charbonneau D., Bakos G. Á., Mandushev G., Dunham E. W., Brown T. M., Latham D. W., Torres G., Sozzetti A., Kovács G., Everett M. E., Baliber N., Hidas M. G., Esquerdo G. A., Rabus M., Deeg H. J., Belmonte J. A., Hillenbrand L. A., Stefanik R. P., 2007, *ApJ*, 663, L37
- O'Donovan F. T., Charbonneau D., Mandushev G., Dunham E. W., Latham D. W., Torres G., Sozzetti A., Brown T. M., Trauger J. T., Belmonte J. A., Rabus M., Almenara J. M., Alonso R., Deeg H. J., Esquerdo G. A., Falco E. E., Hillenbrand L. A., Roussanova A., Stefanik R. P., Winn J. N., 2006a, *ApJ*, 651, L61
- O'Donovan F. T., Charbonneau D., Torres G., Mandushev G., Dunham E. W., Latham D. W., Alonso R., Brown T. M., Esquerdo G. A., Everett M. E., Creevey O. L., 2006b, *ApJ*, 644, 1237

- Ogloza W., Niewiadomski W., Barnacka A., Biskup M., Malek K., Sokolowski M., 2008, *Information Bulletin on Variable Stars*, 5843, 1
- Paczyński B., Sienkiewicz R., 1984, *ApJ*, 286, 332
- Pandey J. C., Singh K. P., 2008, *MNRAS*, 387, 1627
- Parsons S. G., Marsh T. R., Copperwheat C. M., Dhillon V. S., Littlefair S. P., Gänsicke B. T., Hickman R., 2010, *MNRAS*, 402, 2591
- Pizzolato N., Maggio A., Micela G., Sciortino S., Ventura P., 2003, *A&A*, 397, 147
- Popper D. M., 1996, *ApJS*, 106, 133
- , 2000, *AJ*, 119, 2391
- Popper D. M., Etzel P. B., 1981, *AJ*, 86, 102
- Popper D. M., Lacy C. H., Frueh M. L., Turner A. E., 1986, *AJ*, 91, 383
- Ramírez I., Meléndez J., 2005, *ApJ*, 626, 446
- Reid I. N., Hawley S. L., Gizis J. E., 1995, *AJ*, 110, 1838
- Ribas I., 2003, *A&A*, 398, 239
- , 2006a, in *Astronomical Society of the Pacific Conference Series*, Vol. 349, *Astrophysics of Variable Stars*, Sterken C., Aerts C., eds., p. 55
- , 2006b, *Ap&SS*, 304, 89
- Ribas I., Morales J. C., Allende Prieto C., Jordi C., 2007, in *Highlights of Spanish Astrophysics IV*, Figueras F., Girart J. M., Hernanz M., Jordi C., eds., SEA Conference, 2006
- Ribas I., Morales J. C., Allende Prieto C., Jordi C., Bradstreet D. H., Sanders S. J., 2006, *Ap&SS*, 304, 231
- Rozyczka M., Kaluzny J., Pietrukowicz P., Pych W., Mazur B., Catelan M., Thompson I. B., 2009, *Acta Astronomica*, 59, 385
- Russell H. N., Merrill J. E., 1952, *The determination of the elements of eclipsing binaries*, Russell, H. N. & Merrill, J. E., ed.
- Saumon D., Chabrier G., 1991, *Physical Review A*, 44, 5122
- , 1992, *Physical Review A*, 46, 2084

- Schmidt-Kaler T., 1982, in Schaifers, K., & Voigt, H. H. ed. Landolt-Börnstein, Vol. 2b. Springer, Heidelberg
- Schmitt J. H. M. M., Fleming T. A., Giampapa M. S., 1995, *ApJ*, 450, 392
- Schwarzenberg-Czerny A., 1996, *ApJ*, 460, L107
- Ségransan D., Kervella P., Forveille T., Queloz D., 2003, *A&A*, 397, L5
- Shaw J. S., López-Morales M., 2007, in *Astronomical Society of the Pacific Conference Series*, Vol. 362, *The Seventh Pacific Rim Conference on Stellar Astrophysics*, Y. W. Kang, H.-W. Lee, K.-C. Leung, & K.-S. Cheng, ed., p. 15
- Siess L., Dufour E., Forestini M., 2000, *A&A*, 358, 593
- Silva D. R., Gioia I. M., Maccacaro T., Mereghetti S., Stocke J. T., 1987, *AJ*, 93, 869
- Skumanich A., 1972, *ApJ*, 171, 565
- Smith A. B., Caton D. B., 2007, *Information Bulletin on Variable Stars*, 5745, 1
- Stauffer J. R., Hartmann L. W., 1986, *ApJS*, 61, 531
- Stauffer J. R., Jones B. F., Backman D., Hartmann L. W., Barrado y Navascués D., Pinsonneault M. H., Terndrup D. M., Muench A. A., 2003, *AJ*, 126, 833
- Strassmeier K. G., 2009, *A&A Rev.*, 17, 251
- Strassmeier K. G., Hall D. S., Fekel F. C., Scheck M., 1993, *A&ASS*, 100, 173
- Thompson I. B., Kaluzny J., Rucinski S. M., Krzeminski W., Pych W., Dotter A., Burley G. S., 2010, *AJ*, 139, 329
- Torres G., 2007, *ApJ*, 671, L65
- Torres G., Andersen J., Giménez A., 2010, *Astronomy & Astrophysics Review*, 18, 67
- Torres G., Lacy C. H., Marschall L. A., Sheets H. A., Mader J. A., 2006, *ApJ*, 640, 1018
- Torres G., Lacy C. H. S., 2009, *AJ*, 137, 507
- Torres G., Ribas I., 2002, *ApJ*, 567, 1140
- Torres G., Vaz L. P. R., Sandberg Lacy C. H., 2008, *AJ*, 136, 2158

- Vaccaro T. R., Rudkin M., Kawka A., Vennes S., Oswalt T. D., Silver I., Wood M., Smith J. A., 2007, *ApJ*, 661, 1112
- van Altena W. F., Lee J. T., Hoffleit E. D., 1995, The general catalogue of trigonometric [stellar] parallaxes, van Altena, W. F., Lee, J. T., & Hoffleit, E. D., ed.
- van den Besselaar E. J. M., Greimel R., Morales-Rueda L., Nelemans G., Thorstensen J. R., Marsh T. R., Dhillon V. S., Robb R. M., Balam D. D., Guenther E. W., Kemp J., Augusteijn T., Groot P. J., 2007, in *IAU Symposium*, Vol. 240, *IAU Symposium*, W. I. Hartkopf, E. F. Guinan, & P. Harmanec, ed., p. 105
- Viti S., Jones H. R. A., Maxted P., Tennyson J., 2002, *MNRAS*, 329, 290
- Viti S., Jones H. R. A., Schweitzer A., Allard F., Hauschildt P. H., Tennyson J., Miller S., Longmore A. J., 1997, *MNRAS*, 291, 780
- Washuettl A., Strassmeier K. G., 2001, *A&A*, 370, 218
- West A. A., Hawley S. L., Walkowicz L. M., Covey K. R., Silvestri N. M., Raymond S. N., Harris H. C., Munn J. A., McGehee P. M., Ivezić Ž., Brinkmann J., 2004, *AJ*, 128, 426
- Wilson R. E., 1979, *ApJ*, 234, 1054
- Wilson R. E., Devinney E. J., 1971, *ApJ*, 166, 605
- Yi S., Demarque P., Kim Y., Lee Y., Ree C. H., Lejeune T., Barnes S., 2001, *ApJS*, 136, 417
- Young T. B., Hidas M. G., Webb J. K., Ashley M. C. B., Christiansen J. L., Derekas A., Nutto C., 2006, *MNRAS*, 370, 1529
- Zacharias N., Urban S. E., Zacharias M. I., Wycoff G. L., Hall D. M., Monet D. G., Rafferty T. J., 2004, *AJ*, 127, 3043
- Zucker S., Mazeh T., 1994, *ApJ*, 420, 806

Appendix A

CM Draconis data

A.1 Light curves

The CM Dra eclipsing binary system has been photometrically followed-up by different observers due to its very low-mass and the eccentricity of its orbit. The very low-mass of its components makes this system very interesting to test the stellar models of fully convective stars and also to detect extrasolar planets around the binary system. For these reasons, abundant photometric data of the system are available. A total of eight seasons of observations were analyzed in this work:

- **Lacy (1977) light curve:** An *I*-band light curve taken with a 91 cm telescope equipped with a photomultiplier at McDonald Observatory (Texas, USA) was published in Lacy (1977). Figure A.1 shows the WD fit of this light curve done here in order to subtract the effect of spots and third light before combining all the light curves as described in Section 2.2.2.
- **Fairborn light curves:** Six light curves measured in the *I* and *R* bands were obtained with the 0.8 m Four College Automatic Photoelectric Telescope (FCAPT) located at Fairborn Observatory in Southern Arizona in the Patagonia Mountains. Differential photoelectric photometry was conducted from 1995 to 2005 on 335 nights. The photometry was typically conducted using the Cousins *R* and *I* filters. The primary comparison and check stars were HD 238580 and HD 238573, respectively. Integration times of 20 s were used and the typical precision of the delta-*R* and *-I* band measurements was 0.014 mag and 0.011 mag, respectively. The relatively large uncertainties arise mainly from the faintness of CM Dra and uncertainties in centering the variable star using blind-offsets (rather than direct acquisition). For the visualization of these data, the individual fits to the different seasons used in this work are plotted in Figure A.2. These fits include the spots and third light parameters

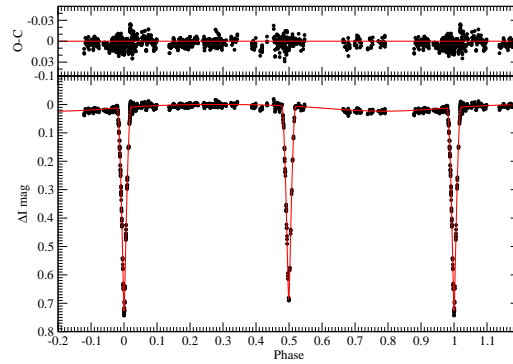


Figure A.1: Best fit (including spots and third light) to the Lacy (1977) CM Dra I -band light curve. The upper panel shows the residuals of the fit.

reported in Table 2.2 of Section 2.2.2. The complete data set is electronically available from Morales et al. (2009a).

- Sleuth light curves:** an additional light curve in the Sloan r' -band was gathered with the Sleuth telescope located at the Palomar Observatory in southern California. Sleuth was one of the three telescopes that together made up the *Trans-atlantic Exoplanet Survey* (TrES), and its primary use was to discover transiting planets orbiting stars brighter than $V = 13$ (e.g., O'Donovan et al. 2006b, 2007; Mandushev et al. 2007). Sleuth consists of a lens with a physical aperture of 10 cm that images a field of view of size 5.7 degrees-square onto a thinned, back-illuminated CCD with 2048×2048 pixels, corresponding to a plate scale of $10''$ per pixel. From UT 2004 March 29 to UT 2004 June 6, Sleuth observed (as part of its survey for transiting planets) a field centered on the guide star HD 151613, and this field fortuitously contained CM Dra. Whenever weather permitted operation, the telescope gathered exposures in r' -band with an exposure time of 90 s and a CCD readout time of 27 s, for a cadence of 117 s. A photometric aperture of radius $30''$ (3 pixels) was used to produce the differential photometric time series. The calibration of TrES images, the extraction of the differential photometric time series (based on image subtraction methods), and the decorrelation of the resulting light curves is described elsewhere (Dunham et al. 2004; Mandushev et al. 2005; O'Donovan et al. 2006a). Figure A.3 shows this light curve with the best fit with spots and third light parameters set as free. The data of this curve are also electronically available from Morales et al. (2009a).

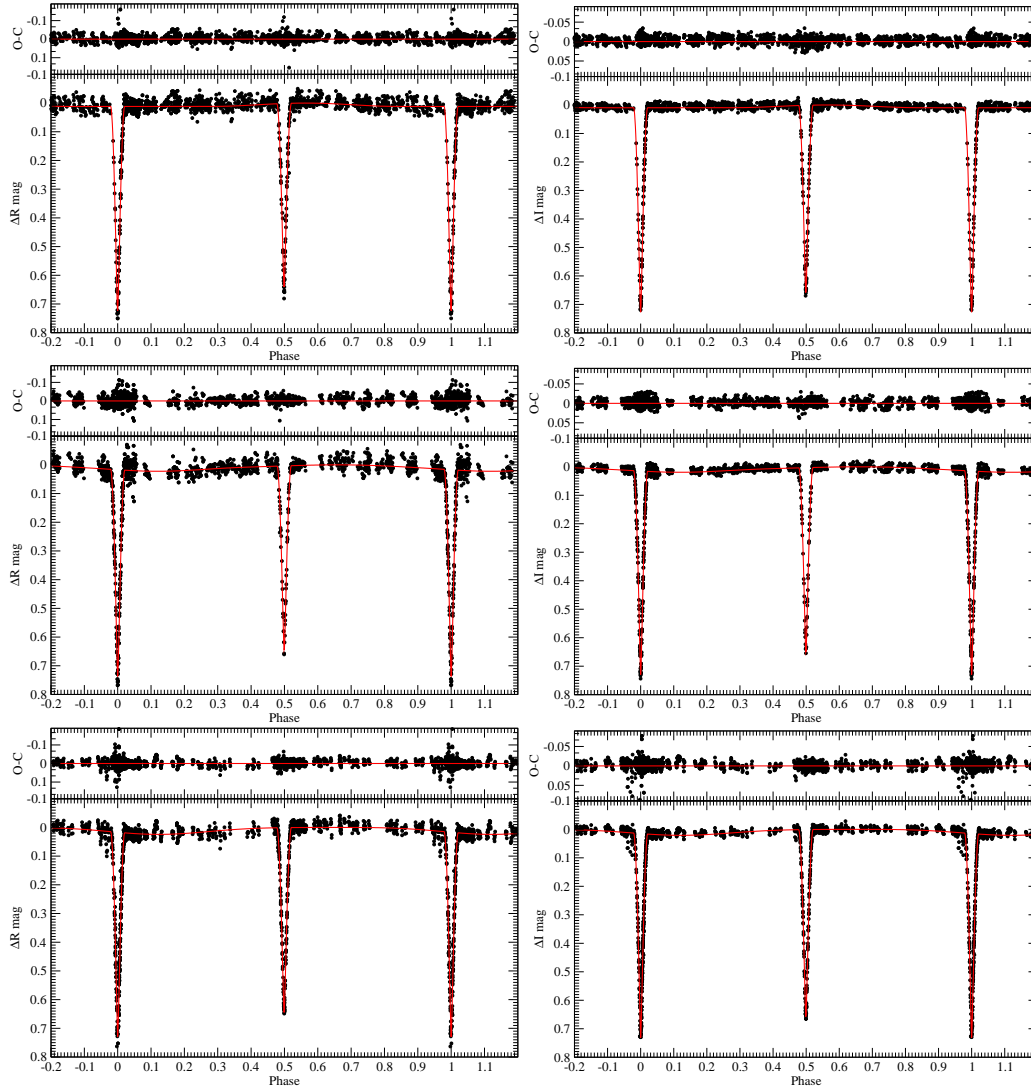


Figure A.2: Best fits (including spots and third light) to the FCAPT CM Dra light curves. The upper panels show the residuals of the fits. Seasons from 1996 to 2001 are displayed from top to bottom, with the *R*-band at left and the *I*-band at right. Notice the different residual scales between *R*- and *I*-bands.

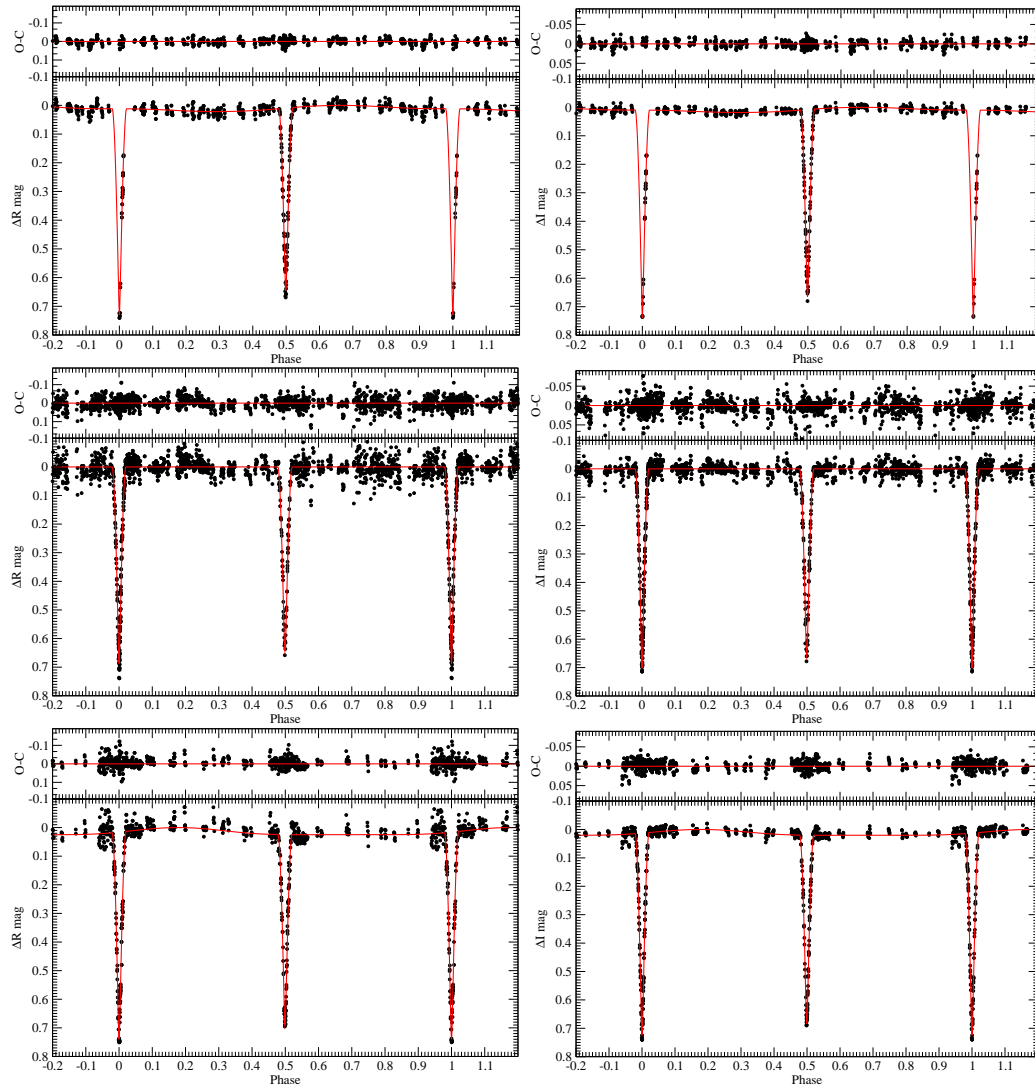


Figure A.2: Continued.

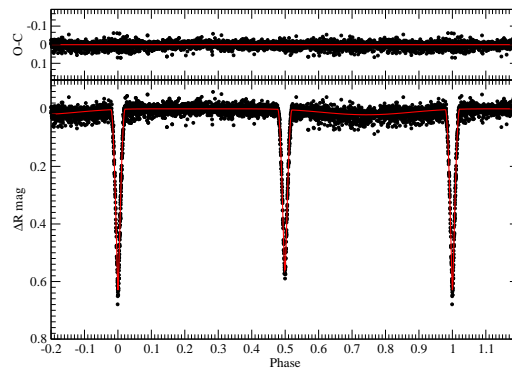


Figure A.3: Best fit (including spots and third light) to the Sleuth CM Dra light curve. The upper panel shows the residuals of the fit.

A.2 Radial velocity curves

For the present study, the spectroscopic material discussed by Metcalfe et al. (1996) was used. These data were obtained over a period of nearly 5 years with an echelle spectrograph on the 1.5 m Tillinghast reflector at the F. L. Whipple Observatory (Mount Hopkins, Arizona). The observations were taken at a resolving power $\lambda/\Delta\lambda \approx 35,000$, and cover approximately 45 \AA in a single order centered near the Mg I *b* triplet at $\sim 5187 \text{ \AA}$. See Metcalfe et al. (1996) for further details on the observations. In the present work, these spectra were reanalyzed with improved techniques compared to the original study. Radial velocities were obtained with TODCOR (Zucker & Mazeh 1994), a two-dimensional cross-correlation algorithm. The template for both components was chosen to be an observation of Barnard’s star (GJ 699, M4Ve) taken with a similar instrumental setup, which provides a close match to the spectral type of CM Dra. Unlike the original study, a special effort to match the rotational broadening of each component by convolving the spectrum of Barnard’s star (assumed to have negligible rotation) with a standard rotational profile was made. The values of the projected rotational velocity of the components ($v \sin i$) that provide the best match to the stars are $9.5 \pm 1.0 \text{ km s}^{-1}$ for the primary and $10.0 \pm 1.0 \text{ km s}^{-1}$ for the secondary. For completeness, Figure A.4 also shows here the radial velocity curves of CM Dra. The data of these curves are electronically available from Morales et al. (2009a).

As a test, other templates obtained with the same instrumentation were used to investigate the possibility of systematic errors in the velocities due to “template mismatch” (see, e.g., Griffin et al. 2000), which might bias the mass determinations. The use of a template made from an observation of the star GJ 725 A (M3.5V) produced rather similar velocities, and an orbital solution with nearly identical el-

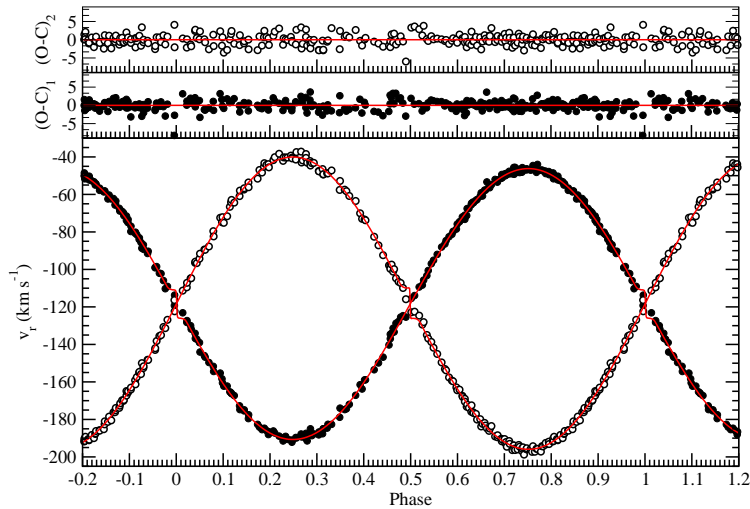


Figure A.4: Best fits to the CM Dra radial velocity curves. Filled and open symbols indicate the primary and secondary components radial velocities, respectively. Upper panels show the residuals of the fits.

ements and formal uncertainties only slightly higher than that of the reference fit (obtained with Barnard’s star as template). The minimum masses from this solution were smaller than the previous results by only 0.23% and 0.14% for the primary and secondary, respectively, which are below the formal errors in those quantities. A template from an observation of GJ 51 (M5.0V) gave an orbital solution that was significantly worse, and minimum masses 0.67% and 0.72% higher than those from the reference fit. As a measure of the closeness of the match to the real components of CM Dra, for each template the cross-correlation value from TODCOR averaged over all exposures was computed. Both of the alternate templates, which bracket the spectral type of CM Dra, gave average correlation values that were lower than the obtained with the GJ 699 template (particularly for GJ 51), indicating the match is not as good. The results using Barnard’s star are thus preferable, and the above tests indicate template mismatch is unlikely to be significant.

A.3 Minima timings

Numerous eclipse timings for CM Dra have been reported in the literature using a variety of techniques, beginning with those of Lacy (1977). Photoelectric or CCD measurements have greater precision and are the most useful for the purposes of this work. Several timings were obtained in the FCAPT and Sleuth observation

campaigns and additionally, new timing measurements were made here from different observatories:

- **Ondřejov Observatory:** A total number of 20 minima were obtained with the 65 cm reflecting telescope with the Apogee AP-7 CCD camera in primary focus from 1997 to 2007. The measurements were done using the Cousins R filter with 30 s exposure time. The nearby star GSC 3881.1146 on the same frame was selected as a primary comparison. No correction for differential extinction was applied because of the proximity of the comparison stars to the variable and the resulting negligible differences in airmass.
- **Roque de los Muchachos Observatory:** 8 CCD minima were obtained during 2007 and 2008 in the Sloan r' band using the 2.0 m Liverpool Telescope in La Palma. High quality photometry (3–4 mmag per measurement) was obtained, with typically 100 photometric points per event.
- **Bradstreet Observatory:** 63 CCD minima were obtained between 1997 and 2002 with a 41 cm f/10 Schmidt-Cassegrain reflector coupled to a Santa Barbara Instruments Group ST-8 CCD camera binned so as to give a scale of $0.93''\text{pixel}^{-1}$. All observations were taken through a Cousins I filter. The comparison star used was GSC 3881.421 which was always contained within the same $13' \times 13'$ field. The exposure times were 25 s in duration, typically resulting in uncertainties of 3 mmag for each data point.
- **F. L. Whipple Observatory:** A secondary eclipse of CM Dra was measured in July 2006 with the 1.2 m telescope using a $4k \times 4k$ CCD camera (KeplerCam), binned to provide a scale of $0.67''\text{pixel}^{-1}$. Observations were made through a Harris I filter relative to a set of 30 comparison stars, and exposure times were 30 s each. Photometric measurements were performed with IRAF using an aperture of $6''$, and have typical uncertainties of 2 mmag.

Table A.1 lists the 200 times of eclipse, 101 primary timings and 99 secondary timings, used in this work. They are electronically available from Morales et al. (2009a). Additional minima timings are currently being obtained with a 80 cm telescope equipped with a CCD at the Montsec Observatory facility.

As explained in Section 2.2.4 the analysis of these times of minimum was used to determine the apsidal motion of the system. Besides, they can also reveal the presence of third bodies in the system through the time-delay effect caused by the orbit of the binary around the barycenter of the system (Irwin 1959; Guinan & Ribas 2001). This produces a sinusoidal modulation of the $(O-C)$ values from the timings. Deeg et al. (2008) reported the possible presence of a third body around CM Dra based on a parabolic fit to their sample of $(O-C)$ values. However, during the analysis done to derive the apsidal motion, it was found that using the timings reported here

a parabolic fit is essentially indistinguishable from a linear fit to the measurements. Thus, any third body must have a period longer than roughly twice the span of the measurements, or ~ 60 years, or must induce a light-time effect below ~ 15 s which would be undistinguishable from the dispersion of the data due to the spot effects, as seen in Section 2.2.4.

Other indications of the possible presence of a third body are the disagreement between the observed apsidal motion and the theoretical prediction (already explained in Section 3.2.2) and the small eccentricity of the close binary orbit of CM Dra. Systems with periods as short as that of CM Dra are usually assumed to be tidally circularized early on (Mazeh 2008), possibly even during the pre-main sequence phase. To explain the present non-zero eccentricity one may invoke the presence of a perturbing component in a more distant orbit. Such configuration can produce secular variations of the orbital parameters of the inner orbit, like eccentricity modulation with a typical period U_{mod} given by:

$$U_{\text{mod}} \simeq P_{1,2} \left(\frac{a_3}{a_{1,2}} \right)^3 \frac{M_1 + M_2}{M_3}, \quad (\text{A.1})$$

where $P_{1,2}$ and $a_{1,2}$ are the period and semimajor axis of the inner orbit of CM Dra, and a_3 and M_3 are the semimajor axis of the third body around the center of mass of the triple system and the mass of the third body, respectively. A third body is actually known in the CM Dra system (the common proper motion white dwarf companion). Adopting a mass for the white dwarf of $0.63 M_{\odot}$ from Bergeron et al. (2001), along with an angular separation from CM Dra of about $26''$ (corresponding to ~ 380 AU at the distance of CM Dra), the modulation period on CM Dra would be roughly 2 Gyr. However, the effect of such a long-period eccentricity pumping would be averaged out over many apsidal motion cycles, and therefore the orbit would remain circular. One may assume that eccentricity pumping by some other body in the system will only be effective if $U_{\text{mod}} \lesssim 5400$ years, which is the period of the apsidal motion found for CM Dra. This provides a constraint on the properties of this putative body, if it is to explain the measured eccentricity. Figure. A.5 represents the allowed region (mass vs. period) of the companion by accounting for the non-detection of light-time effect above 15 s and the eccentricity pumping. Also, a stability criteria of hierarchical triple systems given by $P_3/P_{1,2} \gtrsim 30$ was considered. As can be seen, a massive planet or light brown dwarf with an orbital period of 50–200 days would fulfill all constraints.

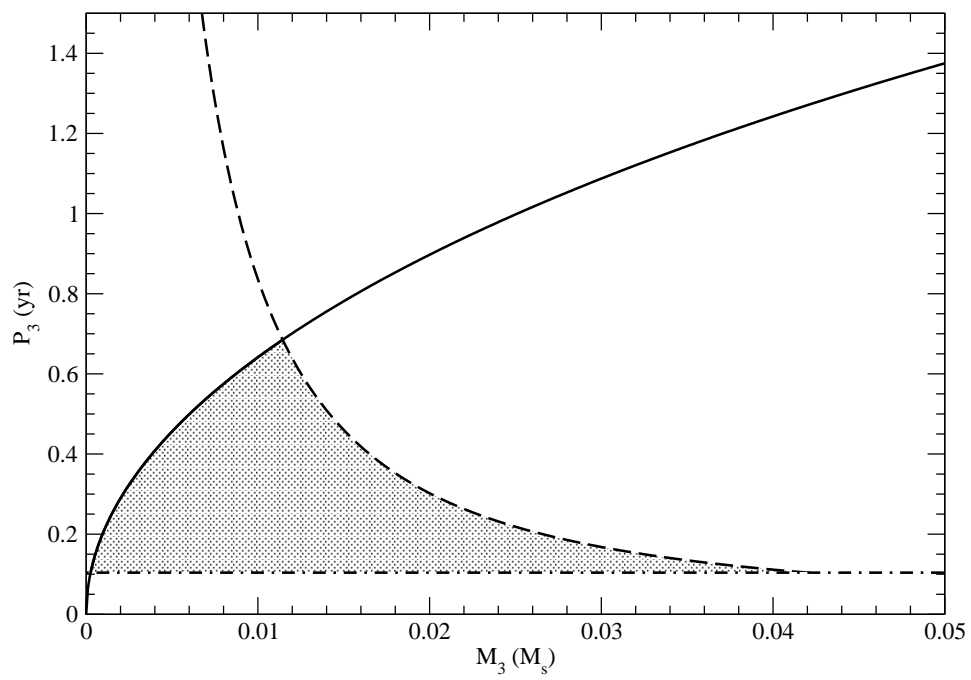


Figure A.5: Allowed region (shaded area) in a mass vs. orbital period diagram for the third body in the CM Dra system according to observational constraints: eccentricity modulation (solid line), light-time effect (dashed line), and stability criteria (dot-dashed line).

Table A.1: Photoelectric and CCD eclipse timings for CM Dra.

HJED	(O - C) (s)	Error (s)	Prim./Sec.	Ref.	HJED	(O - C) (s)	Error (s)	Prim./Sec.	Ref.
2441855.75476	-25.4	30.2	II	2	2450241.71585	35.3	8.6	I	1 Fairborn
2442555.90592	-35.6	30.2	II	2	2450243.61740	-54.1	8.6	II	4
2442557.80955	54.7	30.2	I	2	2450244.88582	-51.5	4.6	II	4
2442607.91053	18.9	30.2	II	2	2450252.49611	-55.8	2.8	II	4
2442888.85928	49.9	30.2	I	2	2450255.66799	22.4	13.0	I	1 Fairborn
2442893.93299	62.9	30.2	I	2	2450257.56974	-49.7	3.1	II	4
2442912.95925	98.4	30.2	I	2	2450259.47343	45.7	4.4	I	4
2442966.86433	-30.8	30.2	II	2	2450262.64335	-45.4	2.9	II	4
2442994.76890	-31.6	30.2	II	2	2450272.79038	-53.2	2.7	II	4
2449494.63438	55.1	2.8	I	4	2450549.93502	70.2	13.0	I	1 Fairborn
2449497.80410	-53.4	4.8	II	4	2450566.42370	36.9	7.4	I	1 Fairborn
2449499.70791	52.5	2.4	I	4	2450567.05703	-37.9	15.6	II	1 Fairborn
2449500.97622	45.6	6.3	I	4	2450568.96077	61.6	5.2	I	1 Fairborn
2449501.60943	-39.5	8.6	II	4	2450624.76998	66.0	5.2	I	1 Fairborn
2449511.75651	-43.0	5.0	II	4	2450631.74490	-39.8	11.2	II	1 Fairborn
2449562.49219	-35.9	2.3	II	4	2450636.81846	-39.8	3.5	II	4
2449815.53701	52.0	7.5	I	4	2450643.79567	52.3	3.0	I	4
2449828.85396	-46.9	2.1	II	4	2450650.77058	-54.4	4.8	II	4
2449830.75778	59.7	1.4	I	4	2450677.40668	-62.1	7.9	II	1 Ondrejov
2449831.39071	-49.5	8.6	II	4	2450710.38499	-47.5	3.5	II	4
2449833.92746	-52.1	1.5	II	4	2450717.36222	45.9	8.6	I	1 Ondrejov
2449840.90481	52.0	3.0	I	4	2450797.90386	-51.2	9.5	II	1 Bradstreet
2449853.58878	58.1	4.1	I	4	2450824.54017	-41.0	4.2	II	1 Fairborn
2449855.49024	-39.1	2.8	II	4	2450831.51755	65.7	3.5	I	1 Fairborn
2449858.66228	52.9	3.3	I	4	2450870.83745	49.9	5.3	I	1 Bradstreet
2449872.61449	46.0	3.8	I	4	2450896.83833	-46.5	9.5	II	1 Bradstreet
2449881.49321	45.2	4.1	I	4	2450903.81571	60.6	4.9	I	1 Bradstreet
2449947.44955	50.4	1.6	I	4	2450905.71696	-55.0	1.8	II	4
2449949.35094	-52.8	1.3	II	4	2450910.79053	-54.1	3.3	II	1 Bradstreet
2449954.42463	-41.6	2.8	II	4	2450931.72037	67.1	4.0	I	1 Bradstreet
2450221.42156	30.8	1.6	I	1 Fairborn, 4	2450942.50042	-41.9	5.4	II	1 Ondrejov
2450222.05487	-45.8	14.7	II	1 Fairborn	2450947.57390	-48.9	6.1	II	1 Bradstreet
2450222.68999	34.5	2.3	I	4	2450948.84223	-54.0	4.1	II	1 Bradstreet
2450225.85983	-63.3	6.9	II	1 Fairborn	2450952.64743	-51.4	6.5	II	1 Bradstreet
2450232.83727	48.3	27.6	I	1 Fairborn	2450955.81953	45.7	5.2	I	1 Bradstreet
2450239.81202	-72.4	12.1	II	1 Fairborn	2450957.72086	-63.1	4.1	II	1 Bradstreet

Table A.1: Continued.

HJED	(O - C) (s)	Error (s)	Prim./Sec.	Ref.	HJED	(O - C) (s)	Error (s)	Prim./Sec.	Ref.
2450962.79443	-62.2	6.0	II	1 Bradstreet	2451309.70014	28.2	5.1	I	1 Bradstreet
2450966.59961	-61.4	2.9	II	1 Bradstreet	2451319.84760	58.0	4.8	I	1 Bradstreet
2450969.77187	50.0	6.0	I	1 Fairborn	2451326.82238	-59.6	4.1	II	1 Bradstreet
2450983.72422	54.8	5.2	I	1 Bradstreet	2451340.77469	-57.9	2.4	II	4
2450990.69909	-55.0	5.8	II	1 Bradstreet	2451359.80061	-51.8	2.2	II	4
2450993.87120	43.1	5.3	I	4	2451373.75289	-52.7	1.6	II	4
2450995.77273	-48.5	4.5	II	1 Bradstreet, 4	2451375.65661	45.1	4.2	I	1 Bradstreet
2450997.67644	49.2	1.8	I	1 Bradstreet	2451394.68279	74.0	6.8	I	1 Bradstreet
2451000.84624	-52.4	3.6	II	4	2451396.58410	-36.3	5.0	II	1 Bradstreet
2451007.82371	61.8	4.4	I	1 Bradstreet	2451434.63567	-47.9	8.5	II	1 Bradstreet
2451009.72497	-52.4	4.2	II	4	2451616.65079	52.3	3.2	I	6
2451021.77588	51.9	4.9	I	1 Bradstreet	2451647.72489	-73.5	7.4	II	1 Bradstreet
2451023.67726	-52.7	4.3	II	1 Bradstreet	2451666.11779	34.1	26.8	I	1 Fairborn
2451026.84940	48.7	6.0	I	1 Bradstreet	2451678.80181	44.8	8.6	I	1 Fairborn
2451028.75095	-41.1	6.7	II	1 Bradstreet	2451685.77675	-59.9	8.1	II	1 Fairborn
2451030.65465	55.2	4.1	I	1 Bradstreet	2451688.94899	50.1	5.9	I	1 Fairborn
2451037.62947	-59.5	6.7	II	1 Bradstreet	2451694.65552	-56.0	9.5	II	1 Bradstreet
2451058.55928	59.8	5.0	I	1 Bradstreet	2451699.72882	-78.9	12.1	II	1 Bradstreet
2451061.72903	-46.2	12.1	II	1 Bradstreet	2451737.78068	-64.7	9.5	II	1 Bradstreet
2451098.51226	-53.2	3.2	II	1 Bradstreet	2451738.41618	48.4	3.5	I	1 Ondrejov
2451219.00919	-63.2	5.4	II	1 Fairborn	2451766.32079	51.0	3.6	I	6
2451220.91291	35.0	4.8	I	1 Bradstreet	2451780.27310	52.6	2.6	I	6
2451224.71832	55.8	7.6	I	1 Bradstreet	2451959.74918	-42.6	5.8	II	1 Bradstreet
2451234.86528	41.6	8.4	I	1 Bradstreet	2451995.89936	49.5	7.1	I	1 Bradstreet
2451236.76683	-48.1	4.3	II	1 Bradstreet	2452004.77828	65.9	13.0	I	1 Bradstreet
2451253.89130	56.1	2.9	I	1 Bradstreet	2452018.73054	62.6	7.9	I	1 Bradstreet
2451256.42819	65.8	3.4	I	1 Ondrejov	2452025.70559	-31.3	7.8	II	1 Bradstreet
2451260.86644	-30.9	4.7	II	1 Bradstreet	2452032.68276	56.9	10.4	I	1 Bradstreet
2451267.84358	55.1	3.4	I	1 Bradstreet	2452037.75635	60.0	11.2	I	1 Bradstreet
2451274.81836	-62.2	5.7	II	1 Bradstreet	2452039.65769	-48.3	9.5	II	1 Bradstreet
2451276.72225	50.6	3.5	I	1 Bradstreet	2452049.80478	-50.3	7.8	II	1 Fairborn
2451281.79579	48.5	4.0	I	1 Bradstreet	2452059.31873	37.8	7.6	I	1 Fairborn
2451293.84457	-31.8	4.2	II	1 Bradstreet	2452059.95186	-54.1	13.0	II	1 Fairborn
2451295.74806	46.6	2.1	I	1 Bradstreet	2452060.58729	53.0	8.6	I	1 Bradstreet
2451299.55336	57.8	6.5	I	1 Bradstreet	2452068.83061	-52.0	8.6	II	1 Fairborn
2451300.82182	63.8	6.3	I	1 Bradstreet	2452084.68665	48.7	7.8	I	1 Fairborn

Table A.1: Continued.

HJED	($O - C'$) (s)	Error (s)	Prim./Sec.	Ref.	HJED	($O - C'$) (s)	Error (s)	Prim./Sec.	Ref.
2452089.76026	53.0	6.9	I	1 Fairborn	2453766.57174	46.2	3.5	I	1 Ondrejov
2452103.71251	49.6	3.3	I	1 Bradstreet	2453832.52817	59.2	3.5	I	1 Ondrejov
2452334.55940	42.1	3.5	I	1 Ondrejov	2453860.43265	50.6	3.5	I	1 Ondrejov
2452416.36948	-50.7	3.6	II	6	2453867.40761	-51.8	3.5	II	1 Ondrejov
2452417.63767	-67.9	13.0	II	1 Bradstreet	2453898.48435	50.7	3.5	I	1 Ondrejov
2452799.42326	-50.2	1.3	II	6	2453925.75358	-49.5	6.0	II	1 Whipple
2452853.33104	53.3	2.5	I	6	2454027.22469	-56.8	4.3	II	1 Ondrejov
2453082.90964	54.9	8.6	I	3	2454149.62564	56.7	4.3	I	1 La Palma
2453103.83677	-58.4	8.5	II	1 Palomar	2454166.74766	-51.2	3.2	II	6
2453107.00881	34.0	7.9	I	1 Palomar	2454189.57866	-52.6	2.2	II	1 La Palma
2453108.91039	-52.5	10.4	II	1 Palomar	2454210.50834	55.3	4.3	I	1 Ondrejov
2453110.81407	41.5	5.7	I	1 Palomar	2454215.58190	54.9	1.6	I	1 La Palma
2453115.88766	44.6	14.7	I	1 Fairborn	2454217.48326	-50.6	1.6	II	1 Ondrejov
2453117.78884	-77.2	13.8	II	1 Palomar	2454227.63024	-63.1	3.5	II	1 La Palma
2453120.96137	57.5	51.0	I	1 Palomar	2454252.36529	62.2	4.3	I	1 Ondrejov
2453122.86268	-52.8	6.8	II	1 Palomar	2454286.61171	52.4	1.8	I	1 La Palma
2453124.76632	37.9	12.1	I	1 Palomar	2454307.53894	-52.0	3.0	II	1 La Palma
2453127.93599	-74.6	7.6	II	1 Palomar	2454335.44357	-47.0	4.3	II	1 Ondrejov
2453131.74132	-61.1	8.1	II	1 Palomar	2454485.74902	59.4	3.1	I	1 La Palma
2453136.81495	-54.6	4.1	II	1 Palomar	2454541.55814	56.0	1.7	I	1 La Palma
2453138.71894	66.6	5.5	I	1 Palomar					
2453143.79266	80.3	6.9	I	1 Palomar					
2453145.69395	-31.2	13.0	II	1 Palomar					
2453153.93938	46.1	15.6	I	1 Palomar					
2453155.84078	-55.9	11.2	II	1 Palomar					
2453157.74473	62.0	21.6	I	1 Palomar					
2453160.91459	-34.7	8.4	II	6					
2453162.81855	83.9	19.9	I	1 Palomar					
2453176.77079	80.1	10.4	I	1 Fairborn					
2453456.44924	-53.1	4.8	II	6					
2453472.30538	55.8	2.9	I	6					
2453478.64744	65.7	8.6	I	5					
2453482.45260	64.8	3.5	I	1 Ondrejov					
2453498.30616	-48.9	5.4	II	6					
2453503.37972	-49.0	3.6	II	6					
2453579.48304	-55.6	3.5	II	1 Ondrejov					

Appendix B

IM Virginis data

B.1 Light curves

Differential photometric observations of IM Vir were conducted in April and May 2006 using the 0.4-m Ealing Cassegrain reflector of the Gettysburg College Observatory (GCO, Gettysburg, Pennsylvania). The camera was a Photometrics (Roper Scientific) CH-350 thermoelectrically-cooled unit equipped with a SITe 003B back-illuminated scientific grade CCD chip and Bessell *BVRI* filters. Exposure times were 120, 60, 25, and 20 seconds, respectively. A number of 597, 672, 630, and 631 observations in *B*, *V*, *R*, and *I*, were obtained with a cadence of about 6 minutes. The field of view of the GCO camera is approximately $18'$, and since IM Vir is a relatively bright target, this severely limited the choice of reference stars of comparable magnitude and color to two: BD-05 3573 ('comp', $\alpha = 12^{\text{h}}48^{\text{m}}36^{\text{s}}.40$, $\delta = -5^{\circ}53'33''.6$, J2000.0; $V = 10.39$, $B - V = 0.67$) and HD 111427 ('check', $\alpha = 12^{\text{h}}49^{\text{m}}14^{\text{s}}.94$, $\delta = -5^{\circ}49'20''.7$, J2000.0; $V = 9.40$, $B - V = 0.67$). The colors of these two stars are in fact nearly identical to that of the variable, which is $B - V = 0.66$.

Differential photometry was performed on IM Vir and the two reference stars in all the images by means of MIRA-AP software (<http://www.mirametrics.com/>). Standard aperture photometry techniques were employed to derive instrumental magnitudes, setting the radius of the measuring apertures for each night using a standard value of 2.5 times the FWHM of the seeing disk, based on previous curve-of-growth calibrations using the same equipment. Typical errors as represented by the scatter of the comp-check differences are 0.0132 mag in *B*, 0.0124 mag in *V*, 0.0135 mag in *R*, and 0.0150 mag in *I*. The data of these light curves are electronically published in Morales et al. (2009b).

As explained in the description of the analysis of the IM Vir light curves, the second half of the photometry showed a systematic 0.01 mag offset with respect the

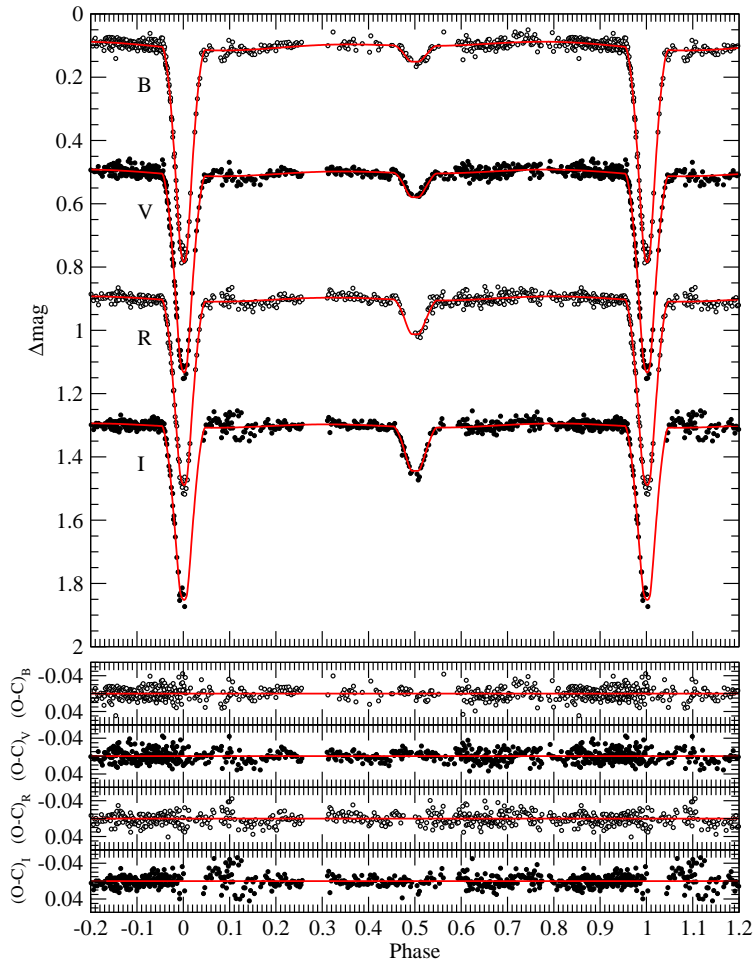


Figure B.1: *BVRI* observations of IM Vir along with the best-fit model. The curves are shifted vertically for clarity. Photometric residuals are shown in the bottom panels, in the same order as the top curves.

first half, probably due to the changes in the spot geometry, and was rejected given its poor phase coverage. In order to visualize all these data, Figure B.1 shows the fits to the first half of these light curves, from which the fundamental properties of the components of IM Vir were obtained, and Figure B.2 shows the second half of the photometry compared with the same fit but excluding the spot terms. The larger scatter is obvious, but the fit is still quite reasonable.

Additional photometry of IM Vir was reported by Manfroid et al. (1991) in the Strömgren *uvby* system. These data were obtained some twenty years earlier than

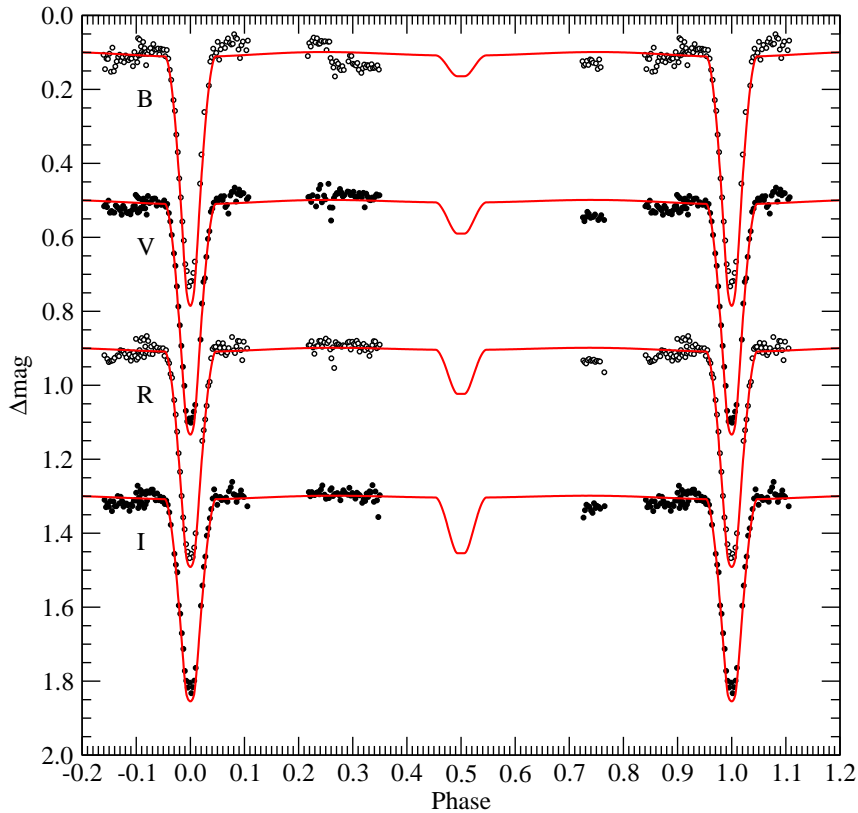


Figure B.2: Differential *BVRI* photometry of IM Vir corresponding to the second half of the data set, The solid curves are the same best-fit model shown in Figure B.1 (without the spots), adjusted for a slight overall brightness change and a phase shift.

the Gettysburg measurements, between 1983 May and 1986 July. Unfortunately, the coverage of the eclipses is very incomplete, so these data was not useful for determining the geometric parameters of the system. Nevertheless, it was possible to extract an average time of eclipse, as well as the brightness ratios in the different bands (0.0167, 0.0353, 0.0599, and 0.0775 in *wby*, respectively), which were used to deconvolve the light of the two stars in order to obtain estimates of the temperatures and the metallicity from color calibrations as explained in Section 2.3.3. Figure B.3 displays the fits to this sparser photometry. Only a phase shift and the light ratios were adjusted in this fit, fixing all the other parameters to those found with the *BVRI* data set.

A total of 5 minima timings were computed from all these photometric data. Three times of eclipse from the *BVRI* photometry were measured by fitting the

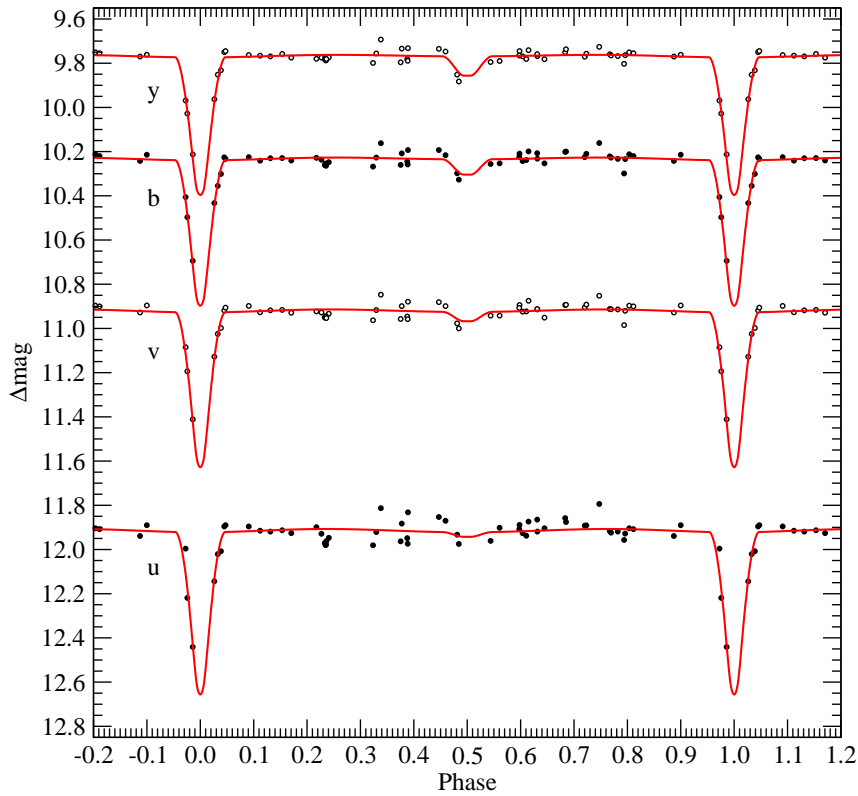


Figure B.3: Strömgren *uvby* photometry on the standard system published by Manfroid et al. (1991), but not used in the light curve analysis, compared with the best-fit model to the *BVRI* data.

adopted final light-curve model (including spot parameters) to each night with sufficient coverage of a primary or secondary minimum, simultaneously in all four pass-bands. The only adjustable parameter allowed in these fits was a time shift. A similar procedure was followed with the Manfroid et al. (1991) photometry, with the primary luminosity in each band added as a free parameter and no spots considered. The resulting eclipse timings for IM Vir are collected in Table B.1, along with an average time of eclipse from the spectroscopy, and the few additional times found in the literature.

Table B.1: Eclipse timings of IM Vir

HJD (2,400,000+)	σ (days)	Type ^a	Instr.	O–C (days)	Source ^c
46042.99984	0.00097	I	ccd	−0.00561	1
51274.8750		I	ccd	+0.02690	2
51885.9610		I	vis	−0.01029	2
52402.87420 ^b	0.00052	I	spec	0.0	4
53474.62948	0.00055	I	ccd	−0.00038	3
53843.65995	0.00010	I	ccd	+0.00067	4
53845.62427	0.00052	II	ccd	+0.00207	4
53877.68325	0.00038	I	ccd	−0.00002	4

^aEclipses labeled as ‘I’ for primary, and ‘II’ for secondary.

^bMean epoch from the radial velocities.

^cSource: 1. Mean epoch from the Manfroid et al. (1991) photometry; 2. B.R.N.O. database (<http://var.astro.cz>); 3. Ogloza et al. (2008); 4. This work.

B.2 Radial velocity curves

IM Vir was spectroscopically observed at the Harvard-Smithsonian Center for Astrophysics (CfA) with three nearly identical echelle spectrographs on the 1.5 m Tillinghamast reflector at the F. L. Whipple Observatory (Mount Hopkins, Arizona), the 1.5 m Wyeth reflector at the Oak Ridge Observatory (Harvard, Massachusetts), and the 4.5 m equivalent Multiple Mirror Telescope (also on Mount Hopkins, Arizona) prior to its conversion to a 6.5 m monolithic telescope. Photon-counting intensified Reticon detectors (‘Digital Speedometers’; Latham 1985, 1992) were used in each case to record a single 45 Å echelle order centered at a wavelength of 5188.5 Å, featuring the gravity-sensitive lines of the Mg I b triplet. The resolving power provided by this setup was $\lambda/\Delta\lambda \approx 35,000$. Nominal signal-to-noise (S/N) ratios for the 138 spectra obtained range from 13 to 58 per resolution element of 8.5 km s^{−1}. The first observation was taken in 1984 January 1, and monitoring continued until 2009 May 10. A handful of the early spectra used were the same ones included in the work of Silva et al. (1987), who discovered the radial-velocity variability, but were re-reduced and analyzed here with much improved methods using TODCOR (Zucker & Mazeh 1994) and synthetic templates based on the ATLAS stellar atmosphere models (Castelli & Kurucz 2004). The radial velocity curves with the best fits are shown in Figure B.4 here for completeness. The complete data set is electronically published in Morales et al. (2009b).

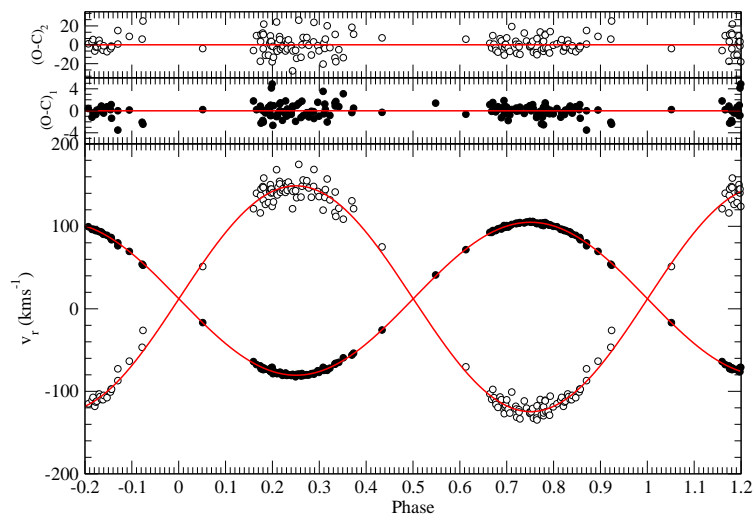


Figure B.4: Phase-folded radial velocity observations for IM Vir (filled circles for the primary, open circles for the secondary), along with the best-fit model. The residuals from the fit are shown in the top panels.

Appendix C

Searching for low-mass eclipsing binaries

Throughout this work it has been mentioned that the number of well-known DDLEBs is scarce. Up to now, only 8 systems (including CM Dra and IM Vir) with at least one component with mass below $0.8 M_{\odot}$ and accurate determinations of its masses and radii are known (Torres et al. 2010). Thus increasing the sample of these systems is still a relevant task to do. With this purpose, several photometric surveys have been conducted (see Hebb et al. 2004; Shaw & López-Morales 2007, as some examples). The ROTES project described in this appendix is one of such projects (see Ribas et al. 2006, 2007, for further references).

Additionally, the photometric data obtained with missions such as *COROT* and *Kepler* is also very useful to detect eclipsing binary systems. A selection of low-mass eclipsing binary candidates within the *COROT* data, which is under progress, is also described here.

C.1 The ROTES project

To solve the paucity of known DDLEB systems, the ROTES project (ROTse Telescope Eclipsing-binary survey) conducted a systematic search for late-type binaries in nearby extended clusters using the wide-field robotic capabilities of the ROTSEIIIb telescope. As mentioned in this work, DDLEBs in open clusters are very valuable because their age and chemical composition can be estimated from the cluster membership. Thus, these two fundamental properties can be fixed when comparing with stellar models.

ROTSEIIIb is a fully-robotic 0.450 m f/1.9 telescope with a 2k×2k Marconi

CCD sited at McDonald Observatory (Akerlof et al. 2003). The telescope provides white-light wide-field imaging ($1.85^\circ \times 1.85^\circ$) with its main scientific goal being the detection and follow-up of GRB optical transients. Since such observations only take up a fraction of the available time, the telescope is also used for other projects, mostly time-series photometry of variables sources, supernovae searches, and sky surveys. The ROTES survey is one of such projects (Ribas et al. 2006, 2007). The observations were focused on the Hyades, Collinder 359, Praesepe, Platais 3 and M67. The exposure time was set to 5 s, providing white-light photometry accurate to better than 0.01-0.02 mag down to $V \sim 14$ mag.

Observations of open clusters were routinely taken every clear night. Several fields of each cluster were used to cover a large fraction of the area of the clusters. Depending on various constraints, each field was visited a few times per night to attain optimal phase coverage in the resulting light curves. The images were flat-fielded and calibrated astrometrically by the reduction ROTSE pipeline and aperture photometry of all stars was obtained with IRAF. With the full image sequence for each cluster, a set of UNIX shell scripts and FORTRAN programs were used to carry out a refinement of the astrometry, cross-matching of the stars, determination of a photometric zero-point and finally construct time-series photometry files for each star.

To design an eclipsing binary selection method, observations of the well-studied CU Cnc and YY Gem systems were simulated. The result was that 2 to 7 observations out of 50 randomly distributed in time and 5 to 18 observations out of 100 would occur during the eclipses. Thus, the strategy used with the ROTES data was to evaluate the number of observations with a magnitude $2\text{-}\sigma$ below the average and to select as eclipsing binary candidates those with a certain number of such occurrences. Periods were computed for the selected variable stars using the analysis of variance algorithm (Schwarzenberg-Czerny 1996). Finally, the light curves were used to identify the best eclipsing binary candidates for further study.

The selected eclipsing binary candidates were cross-matched with the 2MASS (Cutri et al. 2003), USNO2 (Monet et al. 1998), UCAC2 (Zacharias et al. 2004) and *Tycho2* (Høg et al. 2000) catalogues. B_T and V_T magnitudes from *Tycho2* (Høg et al. 2000) of the brightest stars in the survey were used to calibrate the ROTSE white light photometry as a function of $(J - K)$ transformed to the Johnson system. Figure C.1 shows this calibration for the Hyades cluster, as an example. An estimation of T_{eff} was made from the $(V - K_S)_0$ index assuming single main-sequence stars with the reddening of the cluster and the color-temperature calibrations in Cox (2000). The distance to each system was derived using a calibration of M_K as a function of $(V - K)_0$ (Johnson 1966). Combining this with UCAC2 proper motions an evaluation of cluster membership probability was performed. A cross-matching

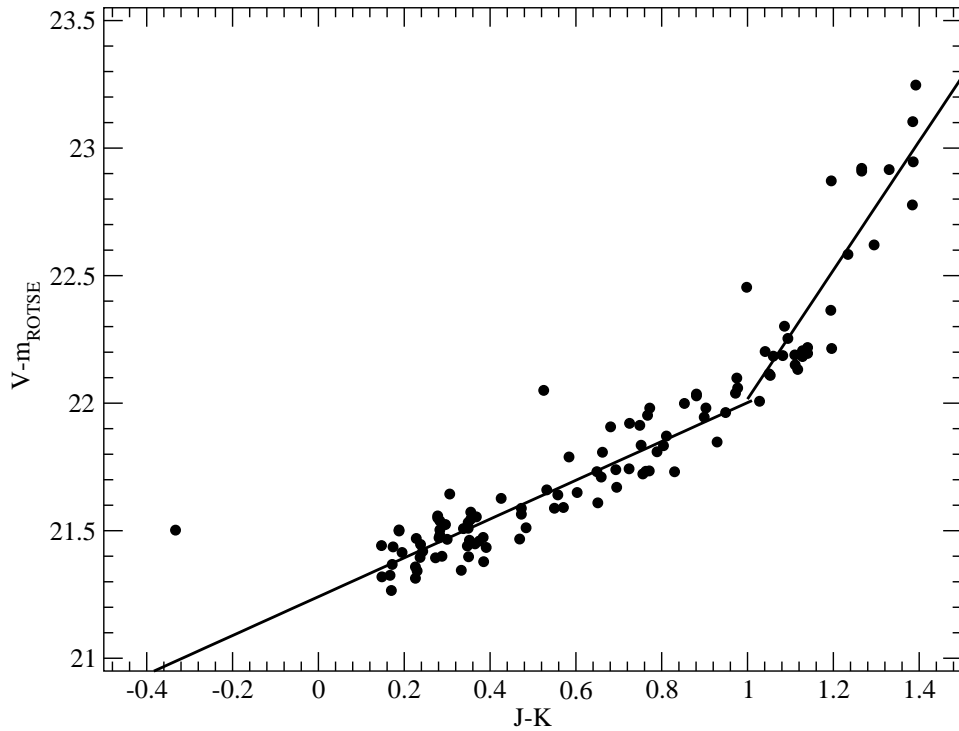


Figure C.1: Calibration of the ROTSE white light photometry using the data of the Hyades cluster.

with SIMBAD catalogue was also done in order to discern the identified variable stars present in the fields.

Table C.1 lists the best eclipsing binary candidates found in the areas of Hyades, Collinder 359, Praeseppe, M67 and Platais 3 clusters and their magnitudes and colors. The number of fields observed for each cluster are 17, 5, 5, 3, and 1, respectively and the approximate number of observations is 130, 50, 100, 90 and 60 for each cluster, respectively. Stars with 6 or 3 (for the less covered clusters) points at least $2\text{-}\sigma$ below the mean magnitude were selected as eclipsing binary candidates. Due to the spatial extension of the Hyades cluster and its large number of observations, more than half of the eclipsing binary candidates are in the field of this cluster. Figure C.2 shows some examples of the binary candidates found and the photometric follow-up of one of these systems providing the efficiency of the selection method.

Unfortunately, none of the systems was found to be member of the observed clusters, although still useful for eclipsing binary analysis. Spectroscopic and precise

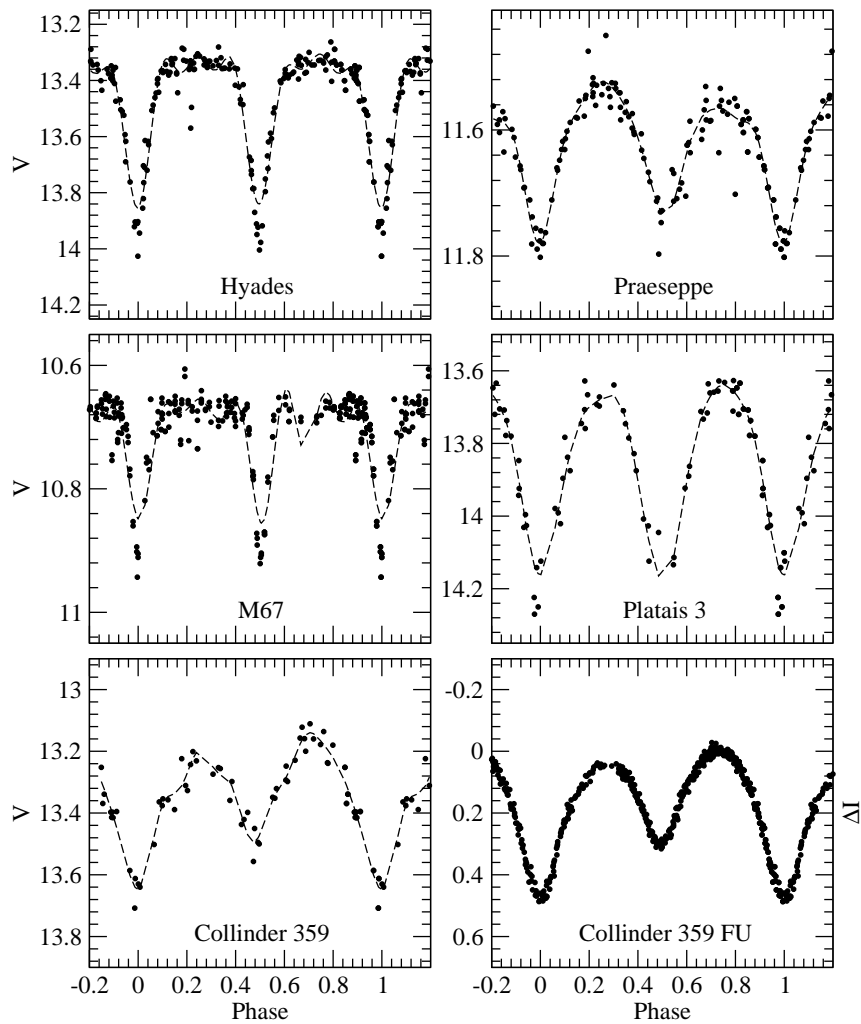


Figure C.2: Light curves of some of the variable stars discovered in the ROTES project for the open clusters surveyed. The bottom right panel shows a photometric follow-up with a 40 cm telescope equipped with a CCD of the Collinder 359 candidate plotted at its left.

photometric follow-up of some targets is still pending. Additional clusters such as Melotte 111, NGC 6939, NGC 6866, NGC 7062, NGC 7789, NGC 188 were observed and they are currently in the image reduction process.

Table C.1: Eclipsing binaries found in the region of the clusters surveyed with ROTSEIIIb.

Star	P (days)	V_{max}	$(V - K)_0$	Star	P (days)	V_{max}	$(V - K)_0$
Hyades							
star61.44196	0.29	13.93	2.50	star61.90892	1.76	13.31	3.09
star62.27151	1.56	13.42	2.35	star62.31986	0.59	12.53	1.13
star62.81043	2.21	13.23	2.47	star63.68436	1.37	12.81	2.24
star64.40810	0.38	14.39	1.81	star64.52607	4.09	14.90	3.41
star65.02993	0.44	14.20	1.60	star65.39291	0.63	14.35	1.79
star66.23733	0.61	14.92	2.55	star66.40923	0.62	13.33	1.63
star66.93768	0.53	14.65	2.04	star67.31705	0.41	10.95	1.66
star67.62950	0.85	11.61	2.52	star68.35001	0.37	14.65	2.03
star68.38767	0.27	14.81	3.00	star68.55581	0.67	15.14	3.25
star69.05671	2.07	13.79	2.46	star69.12546	1.33	13.64	1.82
star69.46529	1.14	13.22	1.86	star69.72262	3.80	12.16	3.13
star69.79089	1.09	13.81	1.88	star69.83558	0.36	14.20	2.65
Collinder 359				Praesepe			
star268.26082	0.31	13.13	1.77	star128.74077	0.32	11.5	1.84
star268.47580	3.47	12.05	3.40	star128.97387	3.49	13.7	1.38
star271.42918	0.50	13.78	1.07	star130.90600	8.96	12.8	2.51
M67				Platais 3			
star131.58491	0.28	13.2	2.42	star72.52244	0.52	13.7	1.44
star133.39671	1.33	12.8	0.43				
star133.57822	1.30	11.1	0.74				

C.2 Eclipsing binaries from *COROT*

In order to increase the number of DDLEBs with low-mass components, the data from space missions such as *COROT* are also potentially very useful. The *COROT* (COnvection ROtation and planetary Transits) mission is devoted to the study of the interior of stars through asteroseismology and also to the detection of extrasolar planets by the detection of transits on stars. It was launched in December 2006 and it is still providing high-quality light curves of thousands of stars. Its main instrument is a 27 cm aperture telescope equipped with four CCDs (two for the asteroseismology channel and two for the exoplanet channel) that continuously takes photometric measurements of the stars in the field of observation with a cadence of 32 s or 512 s. The short cadence of the observations and the long time span of the photometric follow-up, which range between 150 days (for long runs) and 20 days (for short runs) are suitable to detect long period systems, that if magnetically inactive, could prove the conclusions given in this work. The telescope is alternatively pointing towards two opposite regions of the sky, to the galactic center (18^h50^m) and to the anticenter (6^h50^m), with each pointing duration being up to 150 days, with a duty cycle $\geq 90\%$.

Among other variable systems and transiting exoplanets, eclipsing binaries are being observed by *COROT*, so a selection of low-mass system candidates is being performed according to the colors of the surveyed stars. For each of the observed fields, a cross-correlation with the 2MASS catalog (Cutri et al. 2003) is per-

formed in order to get the IR magnitudes. Stars with $V - K > 2.50$ and with $J - K < 1.83 + 1.13(V - K)$ are selected as good low-mass candidates given the results in Bessell & Brett (1988) and their temperatures are estimated from the $(V - K)$ color according to the calibrations in Cox (2000). The light curves of those systems with better chances of being of low-mass, are plotted and inspected by eye to select good DDLEB candidates.

A total number of 8 *COROT* fields with more than 75000 stars have been cross-correlated with the catalogs, finding more than 36000 low-mass candidates. A first pre-selection of candidates with high proper motions ($\geq 80 \text{ mas yr}^{-1}$), expected to be nearby, reduced the sample to 403 stars, some of which have been selected for spectroscopic observations to better characterize them. Eclipsing binaries coming from false positive transiting exoplanets and from the results of the *COROT* Variable Classifier (CVC) are also inspected.

The main disadvantage of the data coming from this mission is that light curves are commonly affected by instrumental jitter, although it can be subtracted using appropriate filtering. On the other hand, the precision of the light curves is very high, so even eclipses with small depth can be observed. Figure C.3 show the light curve of one of the selected systems after detrending and binning to reduce the large number of data points (more than 128000). The dispersion of this curve is of 0.6 mmag. The effect of photospheric spots was also preliminarily subtracted using a moving average filter in order to clearly see the shallow secondary eclipse. This system is expected to host two stars of approximately $0.9 M_{\odot}$ and $0.2 M_{\odot}$, a mass difference that would be very useful to test stellar structure models on the low-mass range.

The selection of DDLEB candidates from *COROT* and its subsequent spectroscopic characterization and follow-up is foreseen in the framework of the *COROT* Binary Thematic Team. The radial velocity curves of these systems will complete the observational information needed to determine their accurate masses and radii.

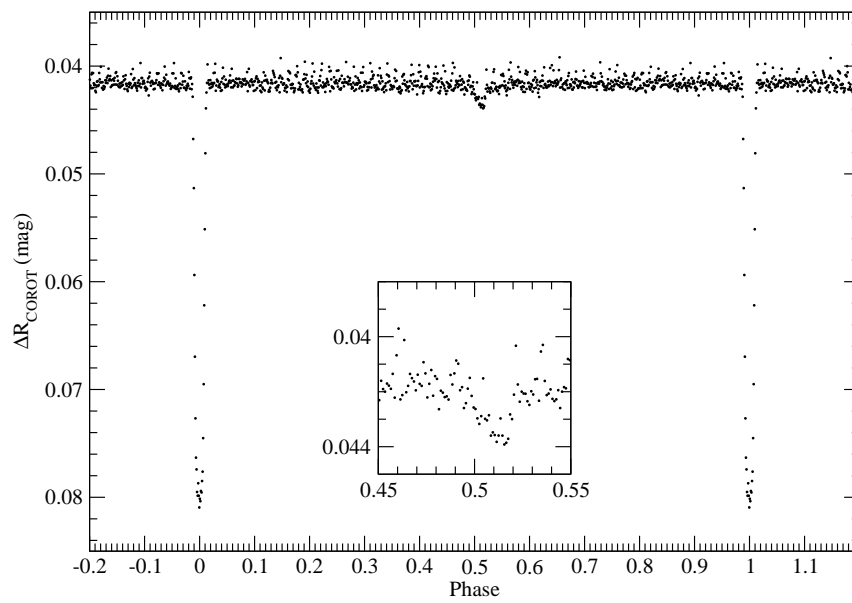


Figure C.3: Example of a R_{COROT} -band light curve of an eclipsing binary observed with *COROT*. The original curve, with more than 128000 data points, was detrended and binned in 0.002 phase bins. The effect of spots on this system was removed in order to better detect the secondary eclipse (shown in the inset). Notice that the depth of the eclipses are of ~ 0.04 mag and ~ 0.002 mag.